Wavenumber Selection in the Stabilized Kuramoto-Sivashinsky Equation: Stationary Probabilities and Dynamics

by

Saloni Saxena

A Thesis Submitted in Partial Fulfillment of the Requirements
for the Degree of
Doctor of Philosophy in Physics

This dissertation by Saloni Saxena is accepted in its present form

by the Department of Physics as satisfying the

dissertation requirement for the degree of Doctor of Philosophy.

Date _____   _____

                                              Prof. J. Michael Kosterlitz, Advisor

Recommended to the Graduate Council

Date _____   _____

                                              Prof. Robert A. Pelcovits, Reader

Date _____   _____

                                              Prof. Thomas R. Powers, Reader

Approved by the Graduate Council

Date _____   _____

                                              Andrew. G. Campbell,

                                              Dean of the Graduate School

Curriculum Vitae

Education

B. S. Physics, St. Xavier's College, Mumbai, India (2012).

M. S. University of Mumbai, India (2014).

M. S. Brown University, USA (2017).

Ph. D. Brown University, USA (expected 2021).

Publications

1. S. Saxena, J. M. Kosterlitz, *Wave-number Selection in Pattern-forming Systems*. Phys. Rev. E. **100** 022223 (2019).

2. S. Saxena, J. M. Kosterlitz, *Dynamics of Noise-induced Wave-number Selection in the Stabilized Kuramoto-Sivashinsky Equation*. Phys. Rev. E. **103** 012205 (2021).

Acknowledgments

First, I would like to thank my advisor Prof. Kosterlitz. I have learnt a lot from our countless discussions over the years. I credit him for introducing me to non-equilibrium statistical mechanics, a field which I want to pursue for the rest of my career. I would also like to thank Prof. Bob Pelcovits and Prof. Tom Powers for agreeing to be on my thesis committee. I am grateful to Profs. Pelcovits and Powers for introducing me to the study of active matter and liquid crystals and for giving me the opportunity to interact with them weekly. This experience has been instrumental in preparing me for postdoctoral interviews.

I am immensely grateful to my family: my mother and sister who have been by my side constantly. This work is dedicated to my father who always had the utmost confidence in me. Finally, none of what I have achieved during my PhD would have been possible with the love and support of my boyfriend Alex, my roommate Lianne and my cats Nannu, Momo, Luna and Night.

Contents

List of Figures

List of Tables

Chapter 1

Introduction

Fluctuations are present in almost every aspect of our day-to-day lives. They occur on a variety of length scales and time scales. Brownian motion, which refers to the random movements of microscopic particles in water occurs on tiny spatiotemporal scales. At the other end of the spectrum, weather fluctuations like hurricanes may arise over tens or hundreds of square miles and last for several days. In many cases, there is a clear separation of scales between systematic or deterministic motion and fluctuations. As long as such a distinction can be made, one can derive deterministic equations of motion such as Newton's laws of mechanics, Coulomb's law of electrostatics and Maxwell's equations of electrodynamics. However, even at the level of classical physics, we know that certain events cannot occur without the presence of fluctuations. Chemical reactions are an important example of this. They involve transitions between different metastable states, for which it is necessary to overcome the energy barrier between those states. In the absence of fluctuations, the system remains in the same state indefinitely. However, if fluctuations are present, there is a finite non-zero probability of a random "kick" that is strong enough to allow the system to escape from its original state. In general, realistic physical systems are highly complex, with a vast number of locally stable states. Noise allows these systems to explore all possible states, even if they are unstable, leading to the plethora of complex patterns seen in nature.

Having argued that fluctuations play a significant role in every physical system, we need to develop a systematic framework to study them. In this work, we use the Langevin equation formalism i.e. we study dynamical equations for the variables of interest with randomly fluctuating terms added by hand [8]. The exact form of the fluctuating terms depends on the nature of the physical fluctuations. Broadly speaking, one can incorporate two types of noise in a differential equation - additive noise and multiplicative noise. Additive noise does not depend on the field variables at any time, while multiplicative noise depends on the state of the system. Once the type of noise to be used is decided, the next step is to define the statistical properties of the noise, namely the mean and the variance. In this work, we will restrict ourselves to the simplest possible case - additive, delta-correlated noise with zero mean. Our aim is to study the effects of such noise on the phenomenon of pattern formation, particularly wavenumber selection (defined below).

Spatiotemporal patterns are ubiquitous in nature. Mathematically, they are represented by nonlinear partial differential equations which undergo a bifurcation from a spatially uniform steady state to periodic steady states with a continuous set of allowed wavenumbers [9, 10]. The band of allowed wavenumbers is determined from a linear stability analysis of the equation of motion and the wavenumber of the perturbation that grows fastest in the linear regime is called the critical wavenumber. The periodic steady states may themselves undergo secondary instabilities such as the Eckhaus instability [10, 11], which occurs when the periodic states are subjected to long wavelength perturbations. Some well-known examples of pattern formation are Rayleigh-Bénard convection, Taylor-Couette flow and cellular interfaces in directional solidification [10, 12, 13, 14, 15]. Examples can also be found in chemistry (reaction-diffusion systems) and biology (chemotaxis-induced patterns in bacterial colonies) [10].

The existence of many apparently equivalent periodic states naturally leads to the question of wavenumber selection. The two main aspects of the problem are: (i) what is the wavenumber of an observed pattern for a specific set of experimental conditions? (ii) is there

a unique preferred wavenumber which is an intrinsic property of the system and does not depend on the initial state of the system? Most previous work on the subject has focused on deterministic mechanisms such as spatially ramped control parameters [3, 4, 16] (see Chapter 4 for details). In all cases, the wavenumber of the final pattern was found to depend on the initial state and experimental constraints. These results have been used to argue that there is no universal selection mechanism.

On the other hand, *stochastic* wave-number selection i.e. selection in the presence of noise has historically been a topic of debate. Most literature on pattern formation ignores fluctuations arguing that thermal fluctuations are too small to have significant effects on macroscopic scales. In contrast, several works have shown other sources of noise can in fact have non-trivial consequences for phase transitions and pattern formation. Examples include noise-mediated shift of the transition point, pure noise-induced phase transitions and fluctuation-induced first-order transitions [17] (and references therein). In spite of these interesting results, there have been surprisingly few investigations of noise-induced selection. One of the first studies of stochastic selection was performed by Kerszberg [18, 19] for the special case of directional solidification. The author studied the evolution of a periodic cellular interface in a model of directional solidification with additive noise and found that the noise drives the interface towards a unique periodicity. Some qualitative arguments to explain this effect were given. More detailed studies have been performed recently in a model known as the stabilized Kuramoto-Sivashinsky (SKS) equation [6, 5, 7]. All these works have provided substantial evidence that noise can select a particular state out of many available ones (see Chapter 4 for details).

Selection of a unique wavenumber by noise is expected for dynamics where the deterministic part is the gradient of a free energy functional,

$$\partial_t u(x,t) = -\delta\mathcal{F}[u]/\delta u(x,t) + \zeta(x,t) \tag{1.1}$$

3

where $\zeta(x, t)$ represents the noise. In this case, it is known that the most probable configuration is the one which minimizes the free energy [20, 8]. An example of a pattern-forming model falling into this category is the Swift-Hohenberg model [21], for which the free energy is minimized by a periodic configuration with wave number q_{min}. In the presence of noise, the wave number of the most probable configuration is found to be very close to q_{min} [22].

It is then natural to ask what happens if the system under consideration cannot be written as the gradient of a free energy functional. This is the question that we will address in this thesis. We choose the SKS equation, previously studied by Obeid et al. [5] and Qiao et al. [6], as our model of interest. This model does *not* possess a free energy functional, and a clear understanding of noise-induced selection is lacking. The thesis is organized as follows: In Chapter 2, we introduce the underlying physics of pattern formation, along with standard mathematical techniques used for studying it. In Chapter 3, we introduce the SKS equation and explore the properties of the deterministic version of the equation. In Chapter 4, we review existing work on wavenumber selection, with and without noise. Finally, in Chapters 5 and 6, we present new results on wavenumber selection in the noisy SKS equation which have been obtained through extensive numerical simulations.

Chapter 2

Pattern Formation: An Overview

In this chapter, we give an overview of the physics and mathematics of deterministic pattern formation. We start by introducing a simple experiment which has been studied extensively in this context. We give a qualitative description of the processes by which patterns arise in this system. Then we proceed to review the basic mathematical tools that are employed to obtain quantitative information about pattern-forming systems. These include linear stability analysis and amplitude equation expansions. We also illustrate some valuable applications of the amplitude equation formalism. Much of this chapter is based on the treatment given in Ref. [10].

2.1 Physical mechanism of pattern formation

The main qualitative features of pattern-forming systems are best visualized through a simple experiment. Consider a gas or liquid confined between two parallel horizontal plates maintained at different temperatures. Let T_1 be the temperature of the bottom plate and T_2 be the temperature of the top plate. We take the orientation of the plates to be parallel to the XY plane. Let the length of the plates be L and the distance between them be d. We take $L >> d$, so that the X and Y directions are "extended directions" while the Z axis is the "confined direction". The setup is shown in Fig. 2.1.
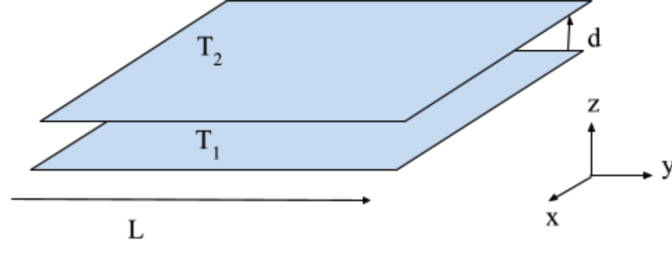
Figure 2.1: Schematic diagram of a typical convection apparatus. The bottom and top plates are at temperatures T_1 and T_2 respectively, where $T_1 > T_2$. The plates have lateral dimension L and are separated by distance d, $L >> d$.

Let us consider what happens when the temperature difference $\Delta T = T_1 - T_2$ is varied. This can be achieved by performing the same experiment several times with a different value of ΔT in each instance. Note that for a particular realization of the experiment, the temperature difference is constant in time. For each instance, we can monitor the motion of the fluid by introducing a tracer to visualize the flow in different parts of the apparatus. Consider first the case where $T_1 = T_2$ so that $\Delta T = 0$. The fluid is thus in thermal equilibrium and is seen to be stationary at long times. Furthermore, this stationary configuration is stable to small perturbations. All perturbations are short-lived and decay with time.

Now let us suppose that the temperature of the bottom plate is larger than that of the top plate, $T_1 > T_2$. Since the temperature is no longer uniform in space, the system is out of equilibrium. Energy is continuously transmitted from the bottom plate to the adjoining fluid, causing warm fluid at the bottom to rise. It is replaced by cold fluid descending from the top. The system is now in a non-equilibrium state which is driven by the temperature gradient.

In any realistic system, the viscosity is non-zero and opposes relative motion between different parts of the fluid. Hence, even if $\Delta T > 0$, macroscopic motion may not occur if the strength of viscous force exceeds the driving of the temperature difference. The competition between dissipative mechanisms such as viscosity and driving mechanisms (the temperature gradient, in this example) determines whether or not the fluid is in motion. The bifurcation from a motionless fluid to a convecting one can be quantitatively characterized by a
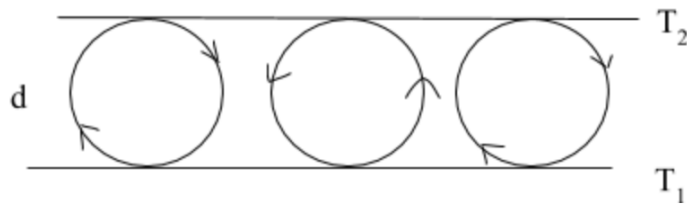
Figure 2.2: Sketch of convection rolls in Rayleigh-Bénard convection.

dimensionless parameter called the Rayleigh number. The Rayleigh number is defined as

$$R = \frac{\alpha g d^3 \Delta T}{\nu \kappa} \tag{2.1}$$

where g is the gravitational acceleration, d is the distance between the plates, ν is the kinematic viscosity, α is the coefficient of thermal expansion and κ is the thermal diffusivity. It turns out that when R is greater than a critical value R_c, the uniform state is destabilized and convection sets in. The Rayleigh number is therefore called the "control parameter".

What does the moving fluid look like? The warm fluid near the bottom rises in some parts of the apparatus, while the cold fluid at the top descends in other parts of the apparatus. The net result is the formation of convection rolls lying parallel to the floor (Fig. 2.2). If we imagine slicing through the rolls along a plane parallel to the plates and make a contour plot of the z component of the fluid velocity in the plane, we would observe a set of parallel stripes, as shown in Fig. 2.3. Here the black regions represent regions of downward flow, while the white regions represent upward flowing fluid. This is an example of "pattern formation", with the pattern in this case being stripes.

The experiment described above is known as Rayleigh-Bénard convection [23, 24]. This is just one of many pattern-forming systems observed in nature and in the laboratory. Prominent naturally-occurring pattern-forming systems include spiral galaxies, ripples in sand dunes and snowflakes [10]. In the laboratory, patterns are observed in fluid dynamics experiments such as the one described above and Taylor-Couette flow [25, 26], biological systems [27, 28, 29], solidification experiments [14, 15, 12, 30] and liquid crystals [31]. In the next
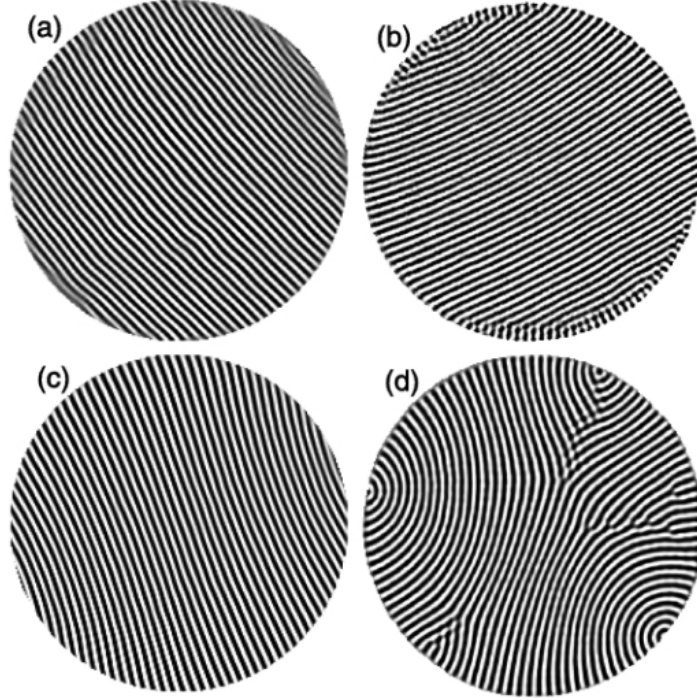
Figure 2.3: Stripe states obtained in an experiment on Rayleigh-Bénard convection. Taken from Ref. [1].

section, we begin a quantitative study of such systems.

2.2   Linear stability analysis

In case of the Rayleigh-Bénard experiment, adjusting the temperature gradient to overcome the dissipative forces leads to the appearance of convection rolls. However, we are interested in developing a general framework for understanding the emergence of patterns out of uniform states, which can be applied to diverse systems of interest. The simplest way to do so is to perform what is known as a "linear stability analysis". Before beginning the linear stability analysis, it is necessary to represent the system by a nonlinear partial differential equation (PDE) [1] for a spatially and temporally varying quantity known as the "order parameter". Such an equation can be obtained by a systematic coarse-graining of the actual physical

---

[1]Models which are discrete in space and time, such as cellular automata have also been widely studied. We will not discuss them here.

equations of motion. The resulting PDE should have a spatially homogeneous steady solution as well as periodic steady solutions, which can be stripes or more complex structures. Once such an equation is available, we add a small perturbation to the uniform steady state and derive the conditions under which the perturbation grows or decays with time. The time evolution of the perturbation determines the stability of the underlying base state.

2.2.1 Example: Linear stability analysis of the one dimensional Swift-Hohenberg equation

It is most convenient to illustrate the process of linear stability analysis with the help of the most widely studied model of pattern formation. This is the Swift-Hohenberg model, and it was developed in the 1970s to describe the convection of a fluid in a situation similar to that described in the previous section [21]. For the purpose of presenting the main steps in the linear stability analysis, it is sufficient to consider the Swift-Hohenberg equation in one spatial dimension. The equation is defined over a spatial domain $0 \leq x \leq L$ and is given by

$$\partial_t u(x,t) = (r-1)u - 2\partial_x^2 u - \partial_x^4 u - u^3 \tag{2.2}$$

In the pattern formation literature, it is customary to write the above equation in the following form.

$$\partial_t u(x,t) = ru - (\partial_x^2 + 1)^2 u - u^3 \tag{2.3}$$

We will see that this form makes it easier to interpret the results of the linear stability analysis. The constant r is known as the *control parameter*. It controls the appearance of spatial patterns from the uniform state and is analogous to the Rayleigh number. The field $u(x,t)$ is related to the z component of the fluid velocity at the center of a very long, narrow convection channel of dimension $L_x = L >> L_y > d$.

It is clear from Eq. (2.3) that $u(x,t) = u_b(x,t) = 0$ is a steady state for all r. Here, the

9

subscript b represents the "base" state, whose stability we are interested in. In a convection experiment, this is the state in which the fluid is at rest. Under what conditions is this state stable? To answer this question, we perturb the base state by adding to it a small perturbation $\delta u(x,t)$.

$$\delta u(x,t) = u(x,t) - u_b(x,t) \tag{2.4}$$

We now substitute this perturbation into the Swift-Hohenberg equation, giving

$$\partial_t(u_b + \delta u(x,t)) = r(u_b + \delta u(x,t)) - (\partial_x^2 + 1)^2(u_b + \delta u(x,t)) - (u_b + \delta u(x,t))^3 \tag{2.5}$$

We now make the assumption that δu is small enough to justify neglecting terms which are nonlinear in the perturbation. If we retain only the linear terms, we arrive at

$$\partial_t \delta u(x,t) = (r - 1 - 2\partial_x^2 - \partial_x^4 - 3u_b^2)\delta u(x,t) \tag{2.6}$$

Because u_b is zero everywhere, the final result is

$$\partial_t \delta u(x,t) = (r - 1 - 2\partial_x^2 - \partial_x^4)\delta u(x,t) \tag{2.7}$$

Since we are interested in spatially periodic patterns, we assume that the perturbation is of the form

$$\delta u(x,t) = Ae^{\sigma(q)t}e^{iqx} \tag{2.8}$$

To ensure that the perturbation is periodic over the domain $0 \leq x \leq L$, q must be of the form

$$q = m(2\pi/L), \quad m = 0, \pm 1, \pm 2, \cdots \tag{2.9}$$

10
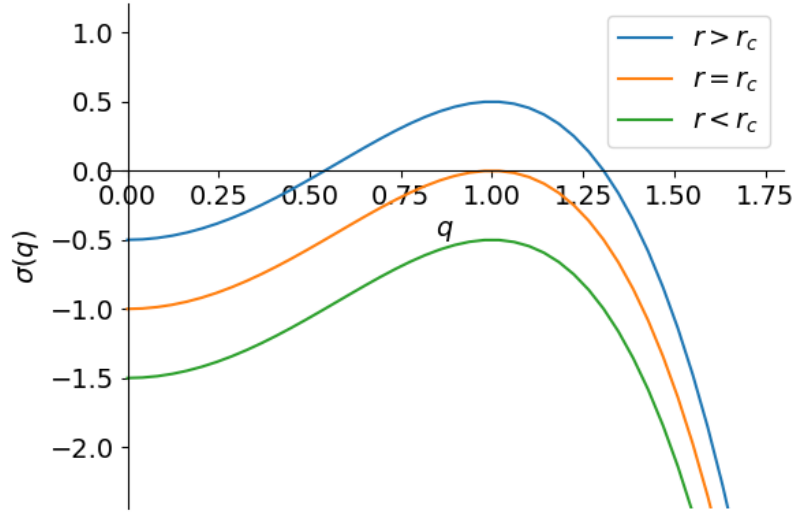
Figure 2.4: A plot of the dispersion relation for the Swift-Hohenberg model, Eq. (2.10) for three different values of the control parameter r - above threshold (blue line), at threshold (orange line) and below threshold (green line).

Substituting this form of the perturbation into Eq. 2.7 yields the growth rate σ as a function of the wavenumber.

$$\sigma(q) = r - (q^2 - 1)^2 \tag{2.10}$$

The time evolution of the perturbation is determined by the sign of $\sigma(q)$. If $\sigma(q) > 0$, the perturbation grows exponentially with time with rate σ. The uniform state u_b is thus destabilized. If, on the other hand, $\sigma(q) < 0$, then the perturbation decays exponentially and the uniform state is stable towards a periodic perturbation of wavenumber q.

Because the evolution of the perturbation is linear, the general solution of Eq. (2.7) can be written as

$$\delta u(x, t) = \sum_q c_q e^{\sigma(q)t} e^{iqx} \tag{2.11}$$

where the coefficients c_q are complex and represent the projection of δu on each wavenumber

in Fourier space. In general, the base state u_b is stable if the maximum real part of all the growth rates is negative.

$$max_q \ Re \ \sigma(q) < 0 \tag{2.12}$$

In Fig. 2.4, we plot Eq. (2.10) for various values of r below, at and above threshold. We see that $\sigma(q) < 0$ for negative r, independent of q (green line). Hence, the base state u_b is stable for all wavenumbers when $r < 0$.

For which values of r and q does σ first become non-negative? Let r_c and q_c be the critical values of the control parameter and wavenumber at which the growth rate crosses zero. These parameters satisfy the relations $\sigma(r_c, q_c) = 0$ and $\frac{\partial \sigma(r,q)}{\partial q}\big|_{q_c} = 0$. Solving simultaneously for r_c and q_c yields

$$r_c = 0, \quad q_c = 1 \tag{2.13}$$

When $r_c = 0$, the growth rate for $q = q_c$ is exactly zero (Fig. 2.4, orange line). When r exceeds r_c, $\sigma(q)$ becomes positive for a band of wavenumbers around q_c (Fig. 2.4, blue line). Perturbations with wavenumbers lying in this band grow exponentially in the linear regime and saturate to periodic steady states in the nonlinear regime. The base state is now *unstable* to periodic perturbations.

In general, the steps of a linear stability analysis can be summarized as follows. Given the form of the evolution equation for the system, we can obtain non-dimensional parameters which govern the bifurcation from the uniform state to the periodic states. For simplicity, let us assume that there is only one control parameter p. Let the critical value of the control parameter be p_c. We now introduce the *reduced control parameter*.

$$\epsilon = \frac{p - p_c}{p_c} \tag{2.14}$$

We rewrite the evolution equation in terms of the reduced control parameter and find the

spatially uniform steady state. We then add a small periodic perturbation to the base state and linearize the equation of motion. Finally, we obtain a dispersion relation giving the growth rate in terms of the wavenumber. The stability properties of the base state follow from an investigation of the dispersion relation.

The quantitative behavior of the growth rate near the critical value p_c and critical wavenumber q_c can be deduced by a simple Taylor expansion. For $p = p_c$ ($\epsilon = 0$) and $q = q_c$, the growth rate $\sigma(p_c, q_c) = 0$. If we keep the wavenumber fixed at q_c and consider small deviations of the reduced control parameter from zero, the Taylor expansion of the growth rate can be written as follows.

$$\sigma(p_c + \epsilon, q_c) = \frac{\epsilon}{\tau_0} + \mathcal{O}(\epsilon^2) \tag{2.15}$$

Here we have used the fact that $\sigma(p_c, q_c) = 0$ and τ_0 is defined as the characteristic time scale of the instability. The form of the first term can be deduced by noting that σ always has dimensions of inverse time, while ϵ is dimensionless. Hence, the first term much contain a coefficient with the dimension of inverse time and we write it as τ_0^{-1}. Finally, since we assume that ϵ is very small, we can neglect terms with quadratic and higher powers of ϵ.

Let us now keep p fixed at p_c and consider small deviations of the wavenumber from the critical wavenumber q_c. For small $|q - q_c|$, $\sigma(p, q)$ can be approximated by a quadratic function of q. We can then write a Taylor series for $\sigma(p_c, q)$ as

$$\sigma(p_c, q) = -\frac{\xi_0^2}{\tau_0}(q - q_c)^2 \tag{2.16}$$

where ξ_0 has the dimensions of length and is called the *coherence length*. It is a measure of the distance over which a local perturbation influences the surrounding pattern. Putting all this together, we can write the growth rate for small deviations of the control parameter

and wavenumber about their critical values as

$$\sigma(p, q) = \frac{1}{\tau_0} \left[\epsilon - \xi_0^2 (q - q_c)^2 \right] \tag{2.17}$$

2.3 Amplitude equation in one dimension

In the previous sections, we studied the emergence of spatially periodic steady states from a uniform state. The states that we considered were *highly idealized*, in the sense that they were perfectly periodic, characterized by a *single wavenumber*. Furthermore, we could only investigate the dynamics in the linear regime i.e. at very short times. Most real experimental systems do not admit perfectly periodic solutions and the most interesting features of patten-forming systems occur in the nonlinear regime. We must therefore generalize the treatment of the previous sections to include spatially distorted states and nonlinear terms. The amplitude equation formalism turns out to be an excellent first step in achieving this [32, 33, 34]. Here, we give a phenomenological derivation of the amplitude equation, using only information about the symmetries of the problem. Then we describe important applications of the amplitude equation.

2.3.1 Phenomenological derivation

Let us consider a system with extended dimensions $x_\perp$, in which the system can be treated as being practically infinite. The system is *finite* in the direction $x_\parallel$. In the experiment of Chapter 1, the x and y directions are the extended directions and the z direction is the confined direction. The $\parallel$ subscript indicates that the z direction is parallel to the tempera-ture gradient, while the $\perp$ symbol indicates that the extended directions are perpendicular to the temperature gradient. For now, we restrict our attention to a system with a single extended direction x. Let us define the spatially varying complex amplitude $A(x, t)$ in terms of a perturbation δu.

$$\delta u(x, \mathbf{x}_{||}, t) = A(x, t) u_c(\mathbf{x}_{||}) e^{iq_c x} + c.c. + \cdots \tag{2.18}$$

Here, $u_c(x_{||})$ accounts for the dependence of the critical mode on the confined direction and q_c is the critical wavenumber. Let us now write

$$A(x, t) = a e^{i\phi(x)} \tag{2.19}$$

where $a(x, t)$ is the real-valued magnitude and $\phi(x, t)$ is the spatially varying phase. Hence, a is the strength of the perturbation about the base state. On the other hand, we can expand $\phi(x)$ about some point x_0 as

$$\phi(x) = \phi(x_0) + k_x(x - x_0) + \cdots \tag{2.20}$$

Then Eq. (2.18) becomes

$$\delta u(x, \mathbf{x}_{||}, t) \approx a e^{i(\phi_0 + k_x(x - x_0))} u_c e^{iq_c x} + c.c. = a e^{i(\phi_0 - k_x x_0)} u_c e^{i(q_c + k_x)x} + c.c. \tag{2.21}$$

which shows that the periodicity of the perturbation is

$$q \approx q_c + k_x \tag{2.22}$$

It is therefore evident that the spatially varying phase $\phi(x)$ is equivalent to changing the wavenumber of the critical mode. In this way, the complex amplitude $A(x, t)$ represents a spatial distortion of the critical state. Using symmetry arguments, it can be shown that the amplitude $A(x, t)$ evolves according to

$$\tau_0 \partial_t A(x, t) = \epsilon A + \xi_0^2 \partial_x^2 A - g_0 |A|^2 A \tag{2.23}$$

15

The form of this equation is independent of the details of the physical system, with system-specific information being included in the coefficients ϵ, ξ, g_0 and τ_0. For one dimensional systems, the two relevant symmetries are translation invariance and parity symmetry. Translation invariance can be ensured by imposing the condition that the amplitude equation be unchanged by the transformation $A \to A e^{i\Delta}$ with Δ constant. This introduces a constant change in phase, which is simply equivalent to a translational shift of the whole pattern. Parity symmetry implies that the equation should be unchanged under the transformations $A \to A^\star$ and $x \to -x$. These conditions restrict the forms of the terms that are allowed in Eq. (2.23). Terms which are products of an odd number of factors of A and $A^\star$, i.e. A, $|A|^2 A$, etc. are allowed under both translation and parity symmetry. On the other hand, even powers are prohibited by translation invariance. The terms A and $|A|^2 A$ are the two lowest order terms which satisfy all the symmetry requirements.

The allowed derivatives follow in a similar manner. First order spatial derivatives such as $\partial_x A$ are allowed by symmetry, but can be absorbed by making the replacement $A \to \bar{A} e^{i\Delta x}$. The second spatial derivative is also allowed and appears in Eq. (2.23). Higher order spatial derivatives are assumed to be negligible since we are studying slow variations of the critical state. Putting all the allowed terms together yields Eq. (2.23).

Having deduced the general form of the amplitude equation, what can we say about the coefficients τ_0, ξ_0 and g_0? By introducing a perturbation of the form $\delta A(t) e^{ikx}$ and linearizing Eq. (2.23), it is straightforward to show that the perturbation has a growth rate given by $\tau_0^{-1}(\epsilon - \xi_0^2 k^2)$. This is simply the growth rate of a perturbation with wavenumber $q = q_c + k$ and so

$$\sigma(q) = \tau_0^{-1} \left[\epsilon - \xi_0^2 (q - q_c)^2 \right] + \cdots \tag{2.24}$$

Hence, the parameters τ_0 and ξ_0 can be identified as the time scale and length scale defined in Eq. (2.17). The system-specific dependence of the parameters ξ_0, τ_0 and g_0 can be conveniently scaled out of Eq. (2.23) by making the following substitutions.

$$\bar{A} = \left| \frac{g_0}{\epsilon} \right|^{1/2} A, X = \frac{|\epsilon|^{1/2}}{\xi_0} x, T = \frac{\epsilon}{\tau_0} t \tag{2.25}$$

Eq. (2.23) then becomes

$$\partial_T \bar{A} = \pm \bar{A} + \partial_X^2 \bar{A} - |\bar{A}|^2 \bar{A} \tag{2.26}$$

which does not involve τ_0, ξ_0 or g_0, again emphasizing the universal nature of the amplitude equation. Note that the first term on the right has a positive (negative) sign when $\epsilon > 0$ ($\epsilon < 0$).

2.3.2 Free energy for the amplitude equation

The amplitude equation is especially amenable to exact calculations, because it has a free energy or potential which governs the dynamics. This is significant because the steady states can then be identified as minima of the potential. The relative stability of the steady states can also be analyzed by comparing the value of the potential for each state.

We claim that the potential is given by

$$V[\bar{A}] = \int_a^b dX \left[-|\bar{A}|^2 + \frac{1}{2}|\bar{A}|^4 + |\partial_X \bar{A}|^2 \right] \tag{2.27}$$

Differentiating with respect to T gives

$$\frac{dV}{dT} = \int_a^b dX \{ \left(-\bar{A} + |\bar{A}|^2 \bar{A} \right) \partial_T \bar{A}^\star + \partial_X \bar{A} \partial_X (\partial_T \bar{A}^\star) + c.c. \} \tag{2.28}$$

Integrating by parts, using Eq. (2.23) and noting that the surface terms vanish for periodic boundary conditions, Eq. (2.28) reduces to

$$\frac{dV}{dT} = -2 \int_a^b dX |\partial_T \bar{A}|^2 \tag{2.29}$$

Since $|\partial_T \bar{A}|^2$ is always positive, it follows that the potential V always decreases with time if

17

$\bar{A}$ satisfies the amplitude equation.

2.3.3 Eckhaus instability

Next we turn to some applications. Perhaps the most important application of the amplitude formalism is to investigate the nonlinear behavior of the periodic states. So far, we have analyzed the stability of the uniform base state with respect to periodic perturbations. However, the resulting periodic steady states can themselves be unstable towards perturbations. These instabilities are called secondary instabilities. Here, we study the instability arising due to long wavelength perturbations, known as the Eckhaus instability. We consider the universal form of the amplitude equation given by Eq. (2.26). We are interested in the stability of the periodic base states as a function of the wavenumber. The base state is given by

$$\bar{A}_K(X) = a_K e^{iKX} \tag{2.30}$$

which represents a periodic state with wavenumber slightly different from the critical one:

$$q = q_c + \xi_0^{-1} \epsilon^{1/2} K \tag{2.31}$$

Substituting Eq. (2.30) in Eq. (2.26) yields the relation

$$a_K^2 = 1 - K^2 \tag{2.32}$$

The allowed wavenumbers are given by

$$-1 \le K \le 1 \text{ or } q_c - \xi_0^{-1} \epsilon^{1/2} \le q \le q_c + \xi_0^{-1} \epsilon^{1/2} \tag{2.33}$$

Again we add a perturbation $\delta\bar{A}$ to this base state

$$\bar{A}(X,T) = \bar{A}_K(X) + \delta\bar{A}(X,T) \tag{2.34}$$

and linearize the amplitude equation yielding

$$\partial_T \delta\bar{A} = \delta\bar{A} + \partial_X^2 \delta\bar{A} - 2|\bar{A}_K|^2 \delta\bar{A} - \bar{A}_K^2 \delta\bar{A}^\star \tag{2.35}$$

Using Bloch's theorem, we can show that the solution of Eq. (2.35) is of the form

$$\delta\bar{A} = e^{iKX}\left[\delta a_+(T)e^{iQX} + \delta a_-^\star(T)e^{-iQX}\right] \tag{2.36}$$

Substituting this in Eq. (2.35) and equating coefficients of $e^{i(K\pm Q)X}$ gives

$$d_T \delta a_+ = -(P^2 + U_+)\delta a_+ - P^2 \delta a_- \tag{2.37}$$

$$d_T \delta a_- = -P^2 \delta a_+ - (P^2 + U_-)\delta a_- \tag{2.38}$$

where

$$P^2 = 1 - K^2 \text{ and } U_\pm = [K \pm Q]^2 - K^2 \tag{2.39}$$

We have replaced the partial derivatives with respect to T with total derivatives (denoted for brevity by d_T) since $\delta a_\pm$ depend only on T. This is a system of linear equations and the growth rate $\sigma_K(Q)$ can be calculated by solving for the eigenvalues of the matrix

$$\begin{bmatrix} -(P^2 + U_+) & -P^2 \\ -P^2 & -(P^2 + U_-) \end{bmatrix} \tag{2.40}$$

The eigenvalues are

$$\sigma_K(Q) = -P^2 - \frac{1}{2}(U_+ + U_-) + \left[P^4 + \frac{1}{4}(U_+ - U_-)^2\right]^{1/2} \tag{2.41}$$

Since we are interested in long wavelength perturbations, the above expression can be simplified by expanding P and $U_\pm$ about $Q = 0$ and retaining the lowest order terms. This gives

$$\sigma_K(Q) = -\left(\frac{1 - 3K^2}{1 - K^2}\right)Q^2 - \left(\frac{2K^4}{(1 - K^2)^3}\right)Q^4 + \cdots \tag{2.42}$$

The coefficient of Q^4 is always negative for $|K| < 1$ and so the sign of the coefficient of Q^2 determines the sign of σ. This term becomes positive when

$$|K| > \frac{1}{\sqrt{3}} \tag{2.43}$$

Thus, for $K < -1/\sqrt{3}$ and $K > 1/\sqrt{3}$, the perturbation grows with time, rendering those base states unstable. The states satisfying $-1/\sqrt{3} \leq K \leq 1/\sqrt{3}$ are stable towards long wavelength perturbations. This band of states is called the Eckhaus stable band (or simply the Eckhaus band). Using the definition of K, the condition for Eckhaus stability can be rewritten in terms of physical quantities as

$$q_c - \frac{1}{\sqrt{3}}\xi_0^{-1}\epsilon^{1/2} \leq q \leq q_c + \frac{1}{\sqrt{3}}\xi_0^{-1}\epsilon^{1/2} \tag{2.44}$$

2.3.4   Phase diffusion

Another important application of the amplitude equation formalism is to derive an evolution equation for the phase of the complex amplitude. We start with Eq. (2.30) which represents a striped state with wavenumber $q = q_c + \xi_0^{-1}\epsilon^{1/2}K$

$$\bar{A} = a_K e^{iKX} \tag{2.45}$$

where $a_K = \sqrt{1 - K^2}$. We now introduce the perturbed amplitude

$$\bar{A}_p(X, T) = a e^{i\Phi} e^{iKX} \tag{2.46}$$

with $a = a_K + \delta a(X, T)$ and linearize in δa, as well as spatial derivatives of Φ. Since the amplitude is taken to be a slowly varying function of the spatial coordinates, we also neglect spatial derivatives of a. We then substitute Eq. (2.46) into the amplitude equation Eq. (2.26), use the relation

$$\partial_T \bar{A} = (\partial_T a + i a \partial_T \Phi) e^{i\Phi} e^{iKX} \tag{2.47}$$

along with a similar expression for $\partial_x^2 A$ to yield the following equations for $\partial_T a$ and $\partial_T \Phi$

$$\partial_T a = (1 - K^2)a - a^3 + \partial_X^2 a - 2Ka\partial_X\Phi - a(\partial_X\Phi)^2 \tag{2.48}$$

$$a\partial_T\Phi = 2(K + \partial_X\Phi)\partial_X a + a\partial_X^2\Phi \tag{2.49}$$

We further neglect the term $(\partial_X\Phi)^2$ and make use of the relation $a_K^2 = 1 - K^2$. This yields

$$\partial_T \delta a = -2a_K^2 \delta a - 2Ka_K\partial_X\Phi + \partial_X^2\delta a \tag{2.50}$$

The first term on the right is much larger than the others, since the other terms involve derivatives of slowly varying quantities. Thus,

$$a_K \delta a \approx -K\partial_X\Phi \tag{2.51}$$

We now substitute $a = a_K + \delta a$ into Eq. (2.49) and neglect $\partial_X \Phi$ since it is small compared to K. The result is

$$a_K \partial_T \Phi \approx 2K \partial_X \delta a + a_K \partial_X^2 \Phi \tag{2.52}$$

Using Eqs. (2.51) and (2.52) finally gives the following equation for the time evolution of the phase Φ

$$\partial_T \Phi = \frac{1 - 3K^2}{1 - K^2} \partial_X^2 \Phi \tag{2.53}$$

Reverting to the original co-ordinates x and t we get

$$\partial_t \Phi = D_{||} \partial_x^2 \Phi \tag{2.54}$$

with

$$D_{||} = (\xi_0^2 \tau_0^{-1}) \frac{\epsilon - 3\xi_0^2 k^2}{\epsilon - \xi_0^2 k^2} \tag{2.55}$$

This is of the same form as the diffusion equation with diffusion coefficient $D_{||}$. Eq. (2.53) implies that a state with wavenumber $q_c + k$ is unstable to long wavelength perturbations of the phase whenever $D_{||} < 0$ or $|\xi_0 k| > \epsilon^{1/2}/\sqrt{3}$. This is simply the Eckaus instability derived in the previous section.

The phase diffusion equation derived above is valid near threshold, since it was obtained from the amplitude equation. However, a generalization of Eq. (2.53) to systems far from threshold has been derived by Cross and Newell [35]. This generalized phase diffusion equation has been instrumental in understanding some quantitative aspects of patterns far from threshold. Here, we simply write the final form of the generalized equation in two dimensional stripe states.

$$\tau(q)\partial_t\phi = \nabla \cdot [\mathbf{q}B(q)] \tag{2.56}$$

where $\tau(q)$ and $B(q)$ are system-dependent quantities which are functions of the local wavenumber $\mathbf{q} = \nabla\phi$. The diffusion coefficients can be shown to be [35]

$$D_\perp(a) = \frac{B(q)}{\tau(q)} \text{ and } D_\parallel = \frac{1}{\tau(q)}\frac{d(qB)}{dq} \tag{2.57}$$

Eq. (2.56) implies that any perturbation of the stripes spreads diffusively. This has been verified experimentally for the roll state in Rayleigh-Bénard convection [36]. The roll state was perturbed by injecting fluid between the rolls. The evolution of this perturbation can be derived analytically from the generalized phase diffusion equation (see Ref. [36] for details). The analytical results matched experimental observations quantitatively.

The generalized phase equation can also be used to study the onset of secondary instabilities such as the Eckhaus instability and the zigzag instability [35]. The Eckhaus instability occurs when the longitudinal diffusion coefficient $D_\parallel(q) < 0$, while the zigzag instability occurs when $D_\perp < 0$. The exact location of the instabilities in the phase diagram depends on the system of interest through the functions $\tau(q)$ and $B(q)$.

Finally, the phase diffusion equation has been employed by Kramer et al. [4] to obtain the spatially varying wavenumber of the stationary solution in the presence of a control parameter "ramp". Control parameter ramps are widely used to precisely tune the periodicity of patterns and will be covered in Chapter 3.

2.4 Summary

In this chapter, we have gained a qualitative understanding of pattern formation in nature. We have also covered some quantitative methods such as linear ability analysis, amplitude equations and phase equations to explore the nonlinear regime. In the following chapter, we

will introduce the physical model which forms the main subject of this work.

Chapter 3

Introduction to the Stabilized Kuramoto-Sivashinsky Equation

In this chapter, we introduce a pattern-forming model known as the stabilized Kuramoto-Sivashinsky equation. The original Kuramoto-Sivashinsky equation reads

$$\partial_t u(x,t) = (-\partial_x^2 - \partial_x^4)u(x,t) + (\partial_x u(x,t))^2 \tag{3.1}$$

This equation first appeared in multiple scales analyses of diverse phenomena such as the Belousov-Zabotinskii reaction [37], motion of a combustion front [38], and flow of a liquid on an inclined plane [39]. More recently, it has been extensively studied to understand spatiotemporal chaos in out-of-equilibrium systems [40, 41, 42, 43, 44, 45]. The uniform state $u = 0$ is unstable to the growth of periodic states for $0 \leq q \leq 1$, with the growth rate being maximum for $q = 1/2$. However, numerical simulations show that these periodic states are rarely accessible for typical initial conditions. Most initial configurations lead to a time-dependent chaotic state [46]. In particular, for rigid boundary conditions, a series of states consisting of cellular states, time-periodic states and intermittent states are observed as the system size is increased. Beyond a particular size, only chaotic solutions are observed.

3.1 The stabilized Kuramoto-Sivashinsky equation

Our problem of interest is a generalization of the original KS equation discussed above. It includes an additional stabilizing term which allows us to access increasingly complex states as the control parameter is tuned. This modified equation is known as the *stabilized Kuramoto-Sivashinsky equation* or the SKS equation and has appeared in the context of step-flow growth [47] and directional solidification of binary alloys [48, 49]. Our investigation of noise-induced selection will focus on this system. There are two main reasons for this choice. Firstly, we chose the SKS equation because it exhibits rich nonlinear behavior and a band of spatially periodic stationary states, while being relatively simple and one dimensional, which makes simulating it easy. The second reason is that it is non-variational, i.e. the deterministic driving force cannot be expressed as the gradient of a potential. Thus, we expect that studying this system would shed light on wave-number selection in systems where minimization of a potential cannot explain selection of a particular state.

The SKS equation in one spatial dimension reads

$$\partial_t u(x,t) = (-\alpha - \partial_x^2 - \partial_x^4)u(x,t) + (\partial_x u(x,t))^2 \tag{3.2}$$

Here, $-\alpha u$ is the stabilizing term. The uniform state $u(x) = 0$ is a solution of this equation. Following the usual procedure, we first investigate the stability of the uniform state with the help of a linear stability analysis. Adding a perturbation of the form $\delta u \sim e^{iqx+\sigma(q)t}$ to the uniform state and linearizing the SKS equation gives the dispersion relation for the growth rate.

$$\sigma(q) = -\alpha + q^2 - q^4 \tag{3.3}$$

For fixed α, the uniform state is stable whenever $\sigma(q) < 0$ and unstable when $\sigma(q) > 0$. Solving the equations $\sigma(q) = 0$ and $\partial\sigma(q)/\partial q = 0$ shows that σ is positive when
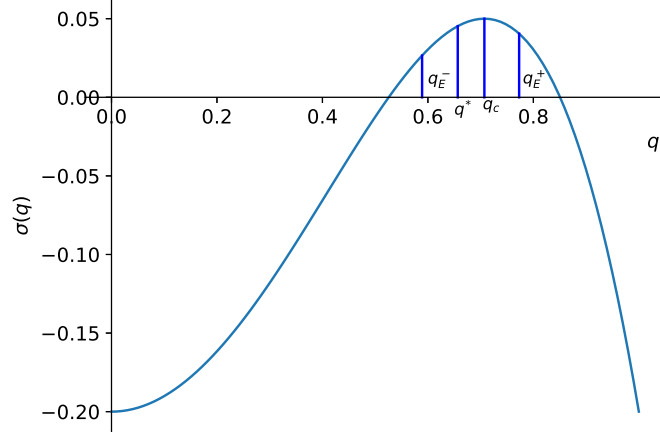
Figure 3.1: Dispersion relation Eq. (3.3) for the SKS equation with $\alpha = 0.20$. $q_E^{\pm}$ represent the boundaries of the Eckhaus band.

$$\alpha \leq \alpha_c = 1/4, \ q_c^2 - \sqrt{\alpha_c - \alpha} \leq q^2 \leq q_c^2 + \sqrt{\alpha_c - \alpha} \tag{3.4}$$

Here, $q_c = 1/\sqrt{2}$ is the critical wavenumber, i.e. the wavenumber for which the linear growth rate is maximum. For any $\alpha \leq 1/4$ and q lying in the above range, periodic perturbations grow exponentially in time during the linear regime. The exponential growth is balanced by the nonlinear terms at later times, resulting in saturated periodic steady states. An example of the dispersion relation is shown in Fig. 2.1.

3.2 Nonlinear steady states

Having explored the linear dynamics of the SKS equation, we turn to the nonlinear regime. A comprehensive characterization of the various nonlinear states has been given by Misbah and Valance [2], who showed that this apparently simple equation has a vast variety of possible time-independent and time-dependent solutions. Here we summarize their mathematical description and results. For the deterministic equation, it is possible to approximately calculate the periodic steady states analytically. We begin by writing a series expansion for a

solution of Eq. (3.2) with wavenumber q.

$$u(x,t) = \sum_{l=-\infty}^{\infty} \widetilde{u}_l(t)e^{ilqx} \tag{3.5}$$

Substituting this expansion into Eq. (3.2), and using the fact that the complex exponentials form an orthogonal set, we get

$$\dot{\widetilde{u}}_l = \sigma_l\widetilde{u}_l - \sum_{m=-\infty}^{\infty} m(l-m)q^2\widetilde{u}_m\widetilde{u}_{l-m} \tag{3.6}$$

We see that in Fourier space, the nonlinear term takes the form of a convolution. The coefficient of the linear term is

$$\sigma_l(q) = -\alpha + l^2q^2 - l^4q^4 \tag{3.7}$$

Now, let us assume that we are close enough to the bifurcation point to be able to neglect the dynamics of the third and higher harmonics. In this regime, the third and fourth harmonics are "slaved" to the first and second harmonics. In other words, one can write the evolution equations for $\widetilde{u}_3$ and $\widetilde{u}_4$ according to Eq. (3.6), set the left side to zero and obtain expressions for $\widetilde{u}_{3,4}$ in terms of $\widetilde{u}_{1,2}$. These expressions can then be substituted into the equations for $\dot{\widetilde{u}}_{1,2}$ and simplified to give

$$\dot{\widetilde{u}}_1 = \sigma_1(q)\widetilde{u}_1 + 4q^2\widetilde{u}_{-1}\widetilde{u}_2 + \frac{48q^2}{\sigma_3(q)}\widetilde{u}_1|\widetilde{u}_2|^2 \tag{3.8}$$

and

$$\dot{\widetilde{u}}_2 = \sigma_2(q)\widetilde{u}_2 - q^2\widetilde{u}_1^2 + \frac{24q^2}{\sigma_3(q)}\widetilde{u}_2|\widetilde{u}_1|^2 + \frac{64q^2}{\sigma_4(q)}\widetilde{u}_2|\widetilde{u}_2|^2 \tag{3.9}$$

Let us now write the complex coefficients $\widetilde{u}_{1,2}$ as

$$\widetilde{u}_1 = \rho_1 e^{i\phi_1}, \quad \widetilde{u}_2 = \rho_2 e^{i\phi_2} \tag{3.10}$$

28

Eqs. (3.8) and (3.9) then become

$$\dot{\rho}_1 = \sigma_1(q)\rho_1 + 4q^2\rho_1\rho_2 cos(\theta) + \frac{48q^2}{\sigma_3(q)}\rho_1\rho_2^2 \tag{3.11}$$

$$\rho_1\dot{\phi}_1 = 4q^2\rho_1\rho_2 sin(\theta) \tag{3.12}$$

$$\dot{\rho}_2 = \sigma_2(q)\rho_2 - q^2\rho_1^2 cos(\theta) + \frac{24q^2}{\sigma_3(q)}\rho_2\rho_1^2 + \frac{64q^2}{\sigma_4(q)}\rho_2^3 \tag{3.13}$$

$$\rho_2\dot{\phi}_2 = q^2\rho_1^2 sin(\theta) \tag{3.14}$$

with

$$\theta = \phi_2 - 2\phi_1 \tag{3.15}$$

Using Eqs. (3.12) and (3.14) and simplifying gives a differential equation for θ.

$$\dot{\theta} = q^2 \left[\rho_1^2/\rho_2 - 8\rho_2\right] sin(\theta) \tag{3.16}$$

In terms of these variables, we can transform back to position space and write

$$u(x,t) = \widetilde{u}_1 e^{iqx} + \widetilde{u}_2 e^{2iqx} + c.c.$$
$$= 2\rho_1 cos(qx + \phi_1) + 2\rho_2 cos(\theta)cos(2qx + 2\phi_1) - 2\rho_2 sin(\theta)sin(2qx + 2\phi_1) \tag{3.17}$$

We now discuss the various solutions obtainable from Eq. (3.17) by choosing different values of θ.

3.2.1 Period-halving bifurcation

We wish to find stationary solutions to Eqs (3.11), (3.12), (3.13) and (3.14). For the moment, we restrict our attention to the cases $\theta = 0$ and $\theta = \pi$. Note that for these choices of θ, Eq. (3.17) becomes symmetric with respect to spatial inversion $x \to -x$. The stationary solutions satisfy

$$\sigma_1(q)\rho_1 \mp 4q^2 \rho_1 \rho_2 + \frac{48q^2}{\sigma_3(q)}\rho_1 \rho_2^2 = 0 \tag{3.18}$$

$$\sigma_2(q)\rho_2 \pm q^2 \rho_1^2 + \frac{24q^2}{\sigma_3(q)}\rho_2 \rho_1^2 + \frac{64q^2}{\sigma_4(q)}\rho_2^3 = 0 \tag{3.19}$$

where the upper sign is for $\theta = \pi$ and the lower sign is for $\theta = \pi$. Next we note that $\rho_1 = 0$ is a solution of Eq. (3.18). We then obtain two kinds of solutions, called pure modes

$$\rho_1 = 0, \theta_+ = \pi \quad (P_+) \tag{3.20}$$

$$\rho_1 = 0, \theta_- = 0 \quad (P_-) \tag{3.21}$$

Setting ρ_1 to zero in Eq. (3.19), we can solve for ρ_2 as

$$\rho_2^2 = -\frac{\sigma_2(q)\sigma_4(q)}{64q^2} \tag{3.22}$$

Since $\sigma_4(q) < 0$, ρ_2^2 is positive only if $\sigma_2(q) > 0$. Thus, the pure modes appear when the second harmonic becomes active.

Let us now generalize to the case where both $\rho_1 \neq 0$ and $\rho_2 \neq 0$. Now, ρ_1 can be factored out of Eq. (3.18) yielding a quadratic equation for ρ_2. The solution is

$$\rho_2 = \frac{\sigma_3(q)}{48q^2}\left[\pm 2q^2 - \left[4q^4 - \frac{48q^2 \sigma_1(q)}{\sigma_3(q)}\right]^{1/2}\right] \tag{3.23}$$

30
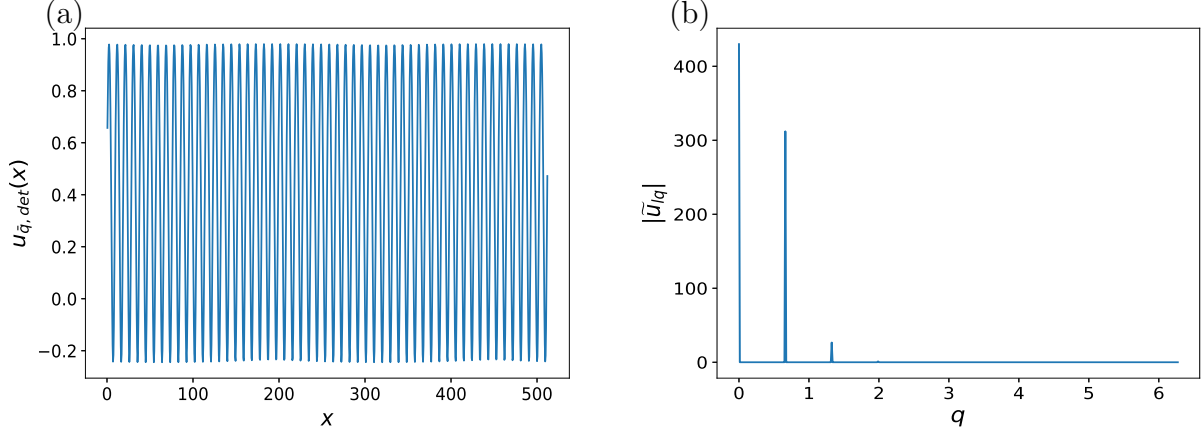
Figure 3.2: (a) Steady state configuration $u_{\bar{q},det}(x)$ for $q = \bar{q} = 0.6627$. (b) The discrete Fourier transform of $u_{\bar{q},det}(x)$, with peaks at $\bar{q}$, $2\bar{q}$ and $3\bar{q}$. Higher harmonics are present but too small to be seen.

Here, we have chosen the solution with a negative sign in front of the square root to ensure that ρ_2 is positive. Substituting this in Eq. (3.19) and solving for ρ_1 gives

$$\rho_1^2 = \frac{\rho_2 \left[\sigma_2(q) + 64q^2\rho_2^2/\sigma_4(q)\right]}{\mp q^2 - 24q^2\rho_2/\sigma_3(q)} \tag{3.24}$$

Since $\sigma_3(q) < 0$ and $\sigma_1(q) > 0$, the expression under the square root in Eq. (3.23) is always positive. Hence, the only condition necessary for the existence of these solutions is that $\rho_1^2 > 0$. If we choose the upper sign ($\theta = \pi$) in Eqs. (3.23) and (3.24), the positivity condition becomes

$$\left[\sigma_2(q) + 64q^2\rho_2^2/\sigma_4(q)\right]\left[q^2 + 24q^2\rho_2/\sigma_3(q)\right] < 0, \quad (M_+) \tag{3.25}$$

If on the other hand, we choose the lower sign ($\theta = 0$), the condition for positivity of ρ_1^2 becomes

$$\sigma_2(q) + 64q^2\rho_2^2/\sigma_4(q) > 0 \quad (M_-) \tag{3.26}$$

These two solutions are known as the "mixed modes" because they arise when both the first and second harmonics are active. We show an example of such a state in Fig. 3.2, in position

31
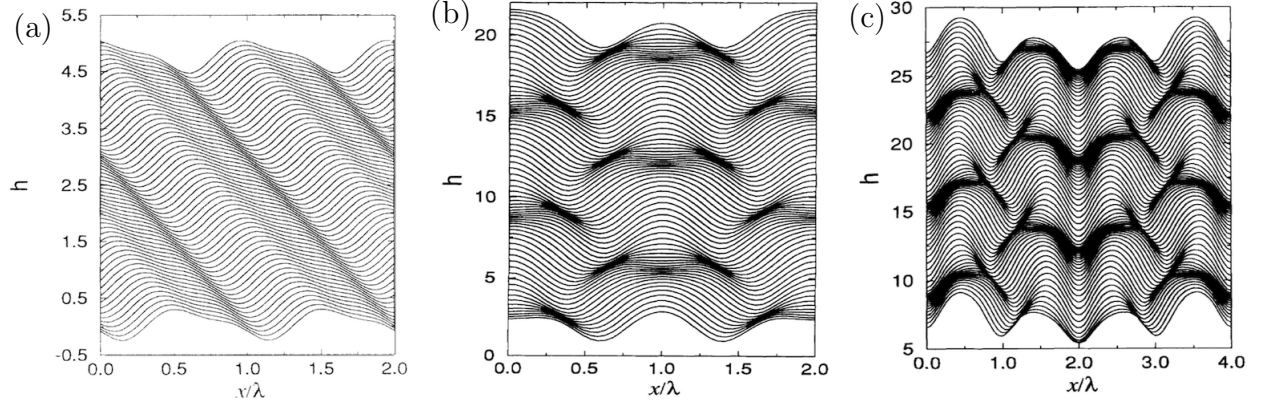
Figure 3.3: Spatiotemporal evolution of instabilities (a) Parity-breaking mode, $\alpha = 0.15, q = 0.46$. (b) Vacillating-breathing mode, $\alpha = 0.1, q = 0.46$. (c) Irrational vacillating-breathing mode. Reproduced from [2]. λ is the wavelength and h is equivalent to u in our notation.

space and Fourier space. We will focus on such states in our investigation of noise-induced selection.

3.2.2 Parity breaking

Now we look at non-trivial values of θ. Setting the left side of Eq. (3.16) to zero, we have

$$\rho_1^2 = 8\rho_2^2 \tag{3.27}$$

Meanwhile, Eqs. (3.11) and (3.13) still hold. Substituting Eq. (3.27) into Eqs. (3.11) and (3.13) with the left sides set to zero, we can solve for $cos(\theta)$ and ρ_2^2

$$cos(\theta) = -\frac{\sigma_3(q)\sigma_1(q) + 48q^2\rho_2^2}{4q^2\sigma_3(q)\rho_2} \tag{3.28}$$

$$\rho_2^2 = -\frac{[2\sigma(q) + \sigma_2(q)]\,\sigma_3(q)\sigma_4(q)}{32\,[9\sigma_4(q) + 2\sigma_3(q)]\,q^2} \tag{3.29}$$

provided that

$$2\sigma_1(q) + \sigma_2(q) > 0, \quad |\sigma_3(q)\sigma_1(q) + 48q^2\rho_2^2| < -4q^2\sigma(3q)\rho_2 \tag{3.30}$$

32
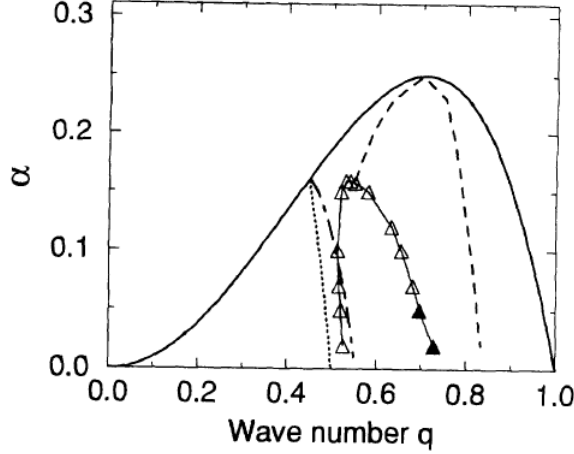
Figure 3.4: Full phase diagram of the SKS equation in the $\alpha - q$ plane. Reproduced from Ref. [2]. For fixed α, the solid line represents the boundaries of the range of wavenumbers in Eq. (3.4). The dashed line is the boundary of the Eckhaus instability, the dotted line is the boundary below which the period-halving bifurcation occurs, and the dash-dotted line is the boundary below which the broken parity states occur. Empty triangles are the boundaries of the vacillating-breathing mode and filled triangles are the boundaries of the irrational vacillating-breathing mode.

Since a non-trivial value of θ breaks the parity symmetry of Eq. (3.17), the solution described above is known as the "parity-breaking mode". It is interesting to note that because this mode is a stationary solution of Eqs. (3.11), (3.13) and (3.16), the right sides of Eqs. (3.12) and (3.14) become time-independent. Thus, the phases are linear functions of time. Hence we can write

$$u(x,t) = 2\rho_1 cos[q(x - vt)] + 2\rho_2 cos(\theta) \ cos[2q(x - vt)] - 2\rho_2 sin(\theta)sin[2q(x - vt)] \quad (3.31)$$

where

$$v = -4q\rho_2 sin(\theta) \quad (3.32)$$

Thus, the parity-breaking instability results in a moving or drifting pattern. The spatiotemporal evolution of this state is shown in Fig. 3.3 (a), where $h(x,t)$ is equivalent to $u(x,t)$ in our notation. The pattern can be seen to drift leftward.

In addition, secondary instabilities that are oscillatory in time can also be observed.

33

These are the vacillating-breathing and "irrational" vacillating-breathing modes. We do not repeat the description of these modes; details can be found in [2]. The spatiotemporal dynamics of these modes are shown in Fig. 3.3 (b) and (c). Finally, we show the full stability diagram of the SKS equation in the $\alpha - q$ plane in Fig. 3.4.

3.3 Summary

In this chapter, we have introduced first the KS equation and then a generalization of it known as the stabilized KS equation. The SKS equation with noise will be the main focus of the rest of this study. The relative simplicity of the equation itself, and the simultaneous existence of an array of complex spatiotemporal patterns even in one dimension make it an ideal system to study wavenumber selection. In the next chapter, we will give a definition for wavenumber selection and explore some prominent examples of the phenomenon.

Chapter 4

Introduction to Wavenumber Selection

From the preceding chapters, it is evident that many non-equilibrium systems, both natural and man-made, have multiple apparently equivalent steady states beyond a certain stability threshold. However, only a narrow subset of the available states is observed in experiments and computer simulations. This phenomenon is called "wavenumber selection". Although this issue has attracted much interest and attention over the last few decades [50, 51, 1, 52, 3, 53, 54, 55, 18, 19, 4, 56, 5, 6, 57, 22], a comprehensive theoretical understanding of it remains elusive. The main questions of interest are the following:

(1) Which physical processes can constrain the set of observed wavenumbers?

(2) Can we predict which wavenumbers are observed for particular experimental conditions?

(3) Is there a unique wavenumber which is preferred for a system, independent of experimental conditions?

In this chapter, we present a summary of the existing literature on the problem of wavenumber selection from the last few decades. A vast variety of mechanisms have been proposed which can be divided into two main types - deterministic mechanisms and stochastic mechanisms.

4.1 Deterministic Mechanisms

In this section, we review the existing results on wavenumber selection in the absence of noise. We will see that the deterministic mechanisms proposed in the literature do not select a unique wavenumber.

4.1.1 Control parameter ramps

One of the most widely studied selection mechanisms is the control parameter ramp, which involves a gradual spatial variation of the control parameter throughout the apparatus. Typically, the apparatus is designed so that the control parameter changes smoothly from values *below* the critical value in one part of the apparatus to values *above* the critical value in another part. Experimental investigations of such ramps have been performed for Taylor-Couette flow [50, 3]. The experiment consists of a fluid like air or water placed between two concentric co-rotating cylinders. The radii of the inner and outer cylinders are r_i and r_o respectively. The outer cylinder is held stationary, while the inner cylinder rotates with a constant angular velocity ω_i. The gap between the two cylinders i.e. $r_o - r_i$ is uniform over a length L and is decreased linearly beyond this length. The rate of decrease of the gap is proportional to the gap angle α, which can be controlled experimentally. The control parameter for Taylor-Couette flow is the Reynolds number R, defined as

$$R = \frac{vl}{\nu} \tag{4.1}$$

where v is a characteristic velocity, l is a characteristic length scale and ν is the kinematic viscosity of the fluid. For this specific experiment, the characteristic length scale is taken to be the distance between the two cylinders i.e. $r_o - r_i$ and the characteristic velocity is the tangential velocity of the inner cylinder i.e. $\omega_i r_i$. The Reynolds number for this problem therefore becomes

$$R = \frac{\omega_i r_i (r_o - r_i)}{\nu} \qquad (4.2)$$

Since $r_o - r_i$ decreases linearly at the bottom of the apparatus, so too does the Reynolds number, yielding the required control parameter ramp.

The pattern-forming dynamics occur in the following way: For $R < R_c \approx 100$, the flow between the cylinders is uniform and time-independent. As R is increased beyond R_c, the uniform state becomes unstable and a series of equally spaced vortices appear. The vortices are symmetric about the axis of the cylinders. As long as the Reynolds number is not too much larger than R_c, the pattern is time-independent and its wavenumber is determined by the spacing between successive vortices. [1] The question of interest is the following: Does spatial variation of the Reynolds number select a "preferred" value of vortex spacing?

Experimental results

Here, we present the findings of an experimental investigation of ramp-induced wavenumber selection in Taylor-Couette flow [3, 50]. To be consistent with the notation of Ref. [3] we will use the wavelength as the relevant quantity and not the wavenumber. The experimental apparatus consists of two coaxial cylinders, separated by a gap as described above. To investigate wavenumber selection, the wavelength of the flow pattern was measured in the straight section for different values of the (bulk) Reynolds number and ramp angle. For a fixed α and several values of the reduced control parameter $\epsilon = R/R_c - 1$, the wavelength was plotted as a function of the aspect ratio (length of the straight section/gap). The results have been reproduced here for convenience. We see that for $\alpha = 0.016$ radians and each ϵ value, the wavelength of the pattern is an oscillating function of the aspect ration. This means that for a given α and ϵ, one can observe a band of wavelengths. The width of the band decreases as ϵ is increased, implying that a single unique wavelength may be observed

---

[1] for $R \gg R_c$, the stationary pattern destabilizes and various time-periodic states such as the wavy vortex state and modulated wavy vortex state are observed. Finally, for still larger values of R, a turbulent state is achieved which lacks any spatial or temporal order. We are not interested in these regimes.
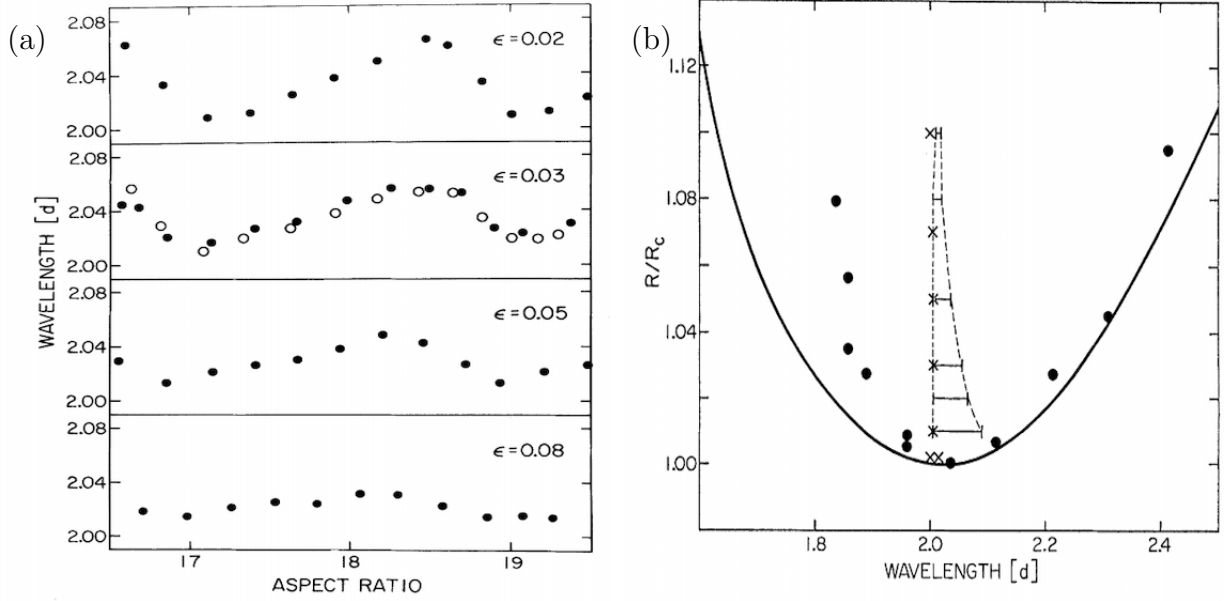
Figure 4.1: Wavelength selection in Taylor-Couette flow by ramps. (a) Mean wavelength as a function of the straight length L for various values of the reduced control parameter. The ramp angle is 0.016 radians. (b) Stable wavelengths as a function of R/R_c. The solid line is the range of wavelengths which grow in the linear regime. Solid circles are the wavelengths observed in the absence of the ramp. Horizontal bars represent the range of stable wavelengths for $\alpha = 0.016$ while crosses represent the wavelengths for $\alpha = 0.02$. Taken from Ref. [3].

only for large values of ϵ. These findings can also be re-expressed by a stability diagram showing the wavelength on the x axis and R/R_c on the y axis. The solid line is the band of allowed wavelengths given by a linear stability analysis. The black circles are results found in the absence of a ramp. The horizontal lines give the range of allowed wavelengths for $\alpha = 0.016$ and the crosses correspond to the same quantity for $\alpha = 0.02$.

Figs. 4.1 (a) and (b) show that even for a fixed value of the control parameter, the observed wavelength depends on α as well as the aspect ratio. This dependence is especially significant for small ϵ. It is thus clear that while a ramp yields a pattern with a well-defined wavelength, the exact value of the wavelength depends on various experimental parameters. In this sense, spatial ramps do not select a unique periodicity.

38

Theoretical illustration

The above observations have been explained theoretically by Kramer et al. [4] for a reaction-diffusion system in one dimension.

$$\partial_t u_1 = D_1 \partial_x^2 u_1 + a_1 u_1 (1 - u_1^2) - b_1 u_2 \tag{4.3}$$

$$\partial_t u_2 = D_2 \partial_x^2 u_2 - a_2 u_2 (1 - u_2^2) + b_2 u_1 \tag{4.4}$$

In this model, the bifurcation from homogeneous to periodic states occurs at a wavenumber given by $q^2 = (a_1 D_2 - a_2 D_1)/2 D_1 D_2$, when $b_1 b_2 < (a_1 D_2 + a_2 D_1)^2/4 D_1 D_2$ and $1 < a_2/a_1 < D_2/D_1$. Hence, the control parameter is $b_1 b_2$. Analytical calculations and simulations result in the stability diagram of Fig. 4.2. Curve 1 gives the limits of the Eckhaus band for $b_1 = b_2 = b$. Curve 2 gives the selected wavelength λ for a slow ramp with $b_1 = b_2 = b$. The bars give the range of wavelengths for a steep ramp and a step variation in b. Curve 3 gives the selected wavelengths when $b_1 = b = const$ and b_2 varying from b to a subcritical value. Curve 4 gives the same quantity with b_1 and b_2 interchanged. The fact that we obtain distinct curves in each case shows that the selected wavelength depends on *how the parameters b_1 and b_2 are varied individually.* This, again, demonstrates the lack of a unique selected wavelength.

4.1.2 Boundary conditions

The theoretical analysis of Chapter 1 assumed infinitely large or periodic systems which are not experimentally realizable. For such cases, we have seen that periodic states with wavenumbers in the Eckhaus band are stable. The analysis of *finite* systems, however, has shown that lateral boundaries can drastically restrict the set of observable wavenumbers. Here, we give a short summary of these studies.
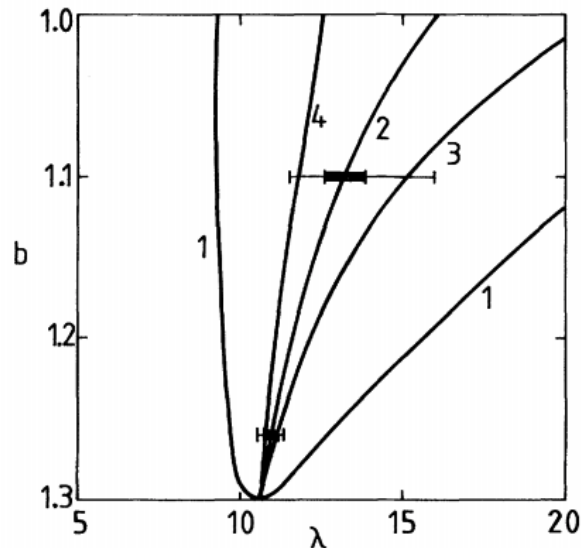
Figure 4.2: Results of Ref. [4].

Arter et al. [51] performed numerical simulations of Rayleigh-Bénard convection in two dimensions. The top and bottom boundaries were maintained at constant temperatures and the side walls were insulated. No-slip boundary conditions were imposed at all the walls. As time increased, an instability was seen to develop at the side walls. The rolls near the side walls were seen to compress and eventually get absorbed by neighboring rolls. This process continued till all the rolls attained roughly the same width. In this way, the band of unstable wavenumbers became narrower due to the presence of lateral walls. A qualitative explanation for this observation was obtained from the amplitude equation. The analysis revealed that the width of the band is of $\mathcal{O}(\epsilon)$ about the critical wavenumber, where ϵ is the reduced control parameter defined in Chapter 1. Recall that the width of the stable band for *periodic* boundary conditions is of $\mathcal{O}(\epsilon^{1/2})$. For $\epsilon << 1$ (i.e. close to threshold, which is the domain of validity of the amplitude equation) this implies that lateral walls shrink the Eckhaus band, as seen in the simulations.

Bodenschatz and Kramer [58] performed an analogous investigation with an *anisotropic* medium, namely a nematic liquid crystal. They studied two cases: a half-infinite system with one side wall and a finite system with two side walls. For the first case, the band of

40

stable wavenumbers was unchanged. Interestingly, the wavenumber of the fastest growing mode *increased.* For the second case, the width of the stable band was found to decrease, in a manner similar to that for an isotropic fluid (see above).

4.1.3   Quench from an initially disordered state

Another mechanism of wavenumber selection that has been studied in some detail is quenching from a disordered initial configuration. In this picture, the deterministic equations of motion are simulated starting from random initial conditions and the wavenumber of the final state is obtained from the maximum of the corresponding power spectrum. The evolution to the final state occurs through a competition between modes of different wavenumbers. At short times, all modes are active because of the disordered initial state. Eventually, all the modes except one decay, resulting in a periodic state with a well-defined wavenumber. The simulation is repeated for several independent realizations of the initial conditions and the late time power spectra are averaged over all realizations to yield the structure function $S(q,t)$. The wavenumber which maximizes $S(q,t)$ can then be designated as the selected wavenumber.

Schober et al. [57] performed such a study in the context of the one-dimensional Swift-Hohenberg equation [13]. The deterministic equation was integrated numerically, starting from random initial conditions with a power spectrum centered at a particular wave number $\bar{q}$. It was observed that the width of the structure function decreased with time until a sharp curve centered about a final wave number q^{∞} was obtained. Their simulations showed that the final wave number depended on the value of $\bar{q}$ and hence did not demonstrate the selection of a unique wavenumber.

4.1.4   Defect dynamics

An important factor that influences the observed patterns is the presence of topological defects. For stripe states, the wavenumber can be controlled by dislocations [10, 9]. A

dislocation is defined as a region where two stripes merge to form one stripe or where one stripe splits into two. Introducing a dislocation at a certain point causes the wavenumber to increase or decrease, through the climbing of the defect. The wavenumber for which the defect comes to rest is the dislocation-selected wavenumber q_d. Similarly, focus defects cause the wavenumber to relax by the creation or annihilation of stripes at the center. The selected wavenumber in this case is q_f. In addition, grain boundaries interact with one another and cause the growth of domains with a particular wavenumber q_g. In general, the three wavenumbers q_d, q_f and q_g are not equal to each other. The selected wavenumber may also be different if more than one type of defect is present.

4.2 Noise-induced Selection

The role of noise in inducing wave-number selection is the subject of some debate. The various mechanisms discussed above do not account for the presence of fluctuations. Neglecting fluctuations is usually justified by claiming that thermal noise is too small to have any significant effect on macroscopic dynamics [10, 9]. While this is certainly true, there can be other sources of noise in an experiment [17]. It is difficult to control experimental parameters precisely. Similarly, environmental disturbances may affect the results of an experiment in various ways. Since the nature of these effects is usually unknown, it is convenient to model them as noise. Motivated by these considerations, there have been some studies of wavenumber selection in the presence of noise. In this section we review the main results of these studies.

4.2.1 Directional Solidification

One of the first investigations of wavenumber selection in the presence of noise was conducted by Kerszberg [18, 19]. Specifically, the author explored the effects of noise on the dynamics of a moving solidification front [30, 14, 13, 12, 15]. The system can be realized experimentally
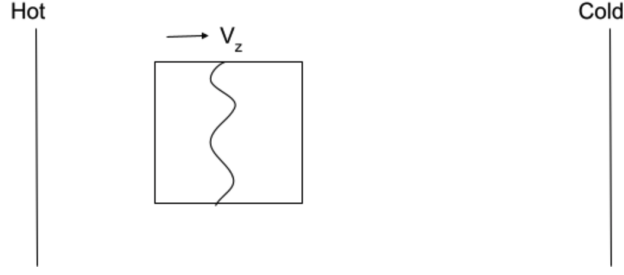
Figure 4.3: Sketch of directional solidification set-up.

by moving a material at a constant velocity V_z from a hot plate located at $-z_0$ to a cold plate at z_0 as shown in Fig. 4.3. As the sample moves from the hot plate to the cold plate, parts of it which are closer to the cold plate start solidifying. The result is a solidification front which moves in the $-z$ direction. For values of $V_z < V_{zc}$ (where V_{zc} is some critical velocity), the shape of the front is *planar*. As V_z is increased beyond this critical value, the planar front destabilizes and is replaced by a cellular structure.

The author first derived effective equations of motion for the solidification front in a binary mixture A-B, assuming a linearly varying temperature field $T(z) = T_0 + Gz$. The equation was of the form

$$\frac{\partial \mu}{\partial t} = D\nabla^2 \mu + V_z \frac{\partial \mu}{\partial z} \tag{4.5}$$

with μ being the chemical potential. Using this equation, the corresponding equation for the interface was derived and a linear stability analysis was performed yielding the range of unstable wavenumbers. To study the effect of noise, the interface equation was supplemented by Gaussian-distributed additive noise and integrated numerically. It was found that the system always evolved to a state with wavenumber κ_0 which depended only on V_z. The evolution occurred through the addition or destruction of cells, depending on the wavenumber of the initial state. All initial conditions were found to converge towards the same wavenumber. A stability diagram was obtained by repeating the simulations for various values of V_z.

4.2.2 The WKB approximation

A notable study on noise induced wave-number selection was performed by Kurtze [56]. The author used a WKB approximation [20] to estimate the stationary probability distribution for a general stochastic differential equation. The state corresponding to the maximum of the probability distribution was then the selected state. The formalism was tested on the Greenside-Cross equation [54] in one dimension and was found to give good agreement with direct numerical simulations. However, to our knowledge, Kurtze's method has not been used to find the selected wavenumber for other pattern-forming systems.

4.2.3 Selection in the noisy Swift-Hohenberg model

Viñals et al. [22] have performed a comprehensive numerical study of the dynamics of the stochastic Swift-Hohenberg (SH) equation in one dimension, with the aim of understanding the mechanism of pattern selection. The stochastic Swift-Hohenberg equation reads

$$\partial_t u(x,t) = ru - \left(\partial_x^2 + 1\right)^2 u^3 + \zeta(x,t) \tag{4.6}$$

where $\zeta(x,t)$ is uncorrelated Gaussian-distributed noise with zero mean, satisfying $\langle \zeta(x,t) \rangle = 0$ and $\langle \zeta(x,t)\zeta(x',t') \rangle = 2\epsilon\delta(x-x')\delta(t-t')$. Here ϵ is the variance of the distribution and is a measure of the strength of the noise. The Swift-Hohenberg equation possesses potential dynamics, with the potential being minimized by a state with wavenumber q_{min} [59].The equation was integrated from random initial conditions, with and without additive noise.

(i) $\epsilon = 0$

For this case, the pattern at long times was observed to approach a stationary configuration characterized by wavenumber q. The value of q was found to be dependent on the initial conditions and lay within a narrow interval centered about the critical mode of the model. Two regimes were observed in the evolution. In the linear regime, all the linearly unstable

modes were seen to grow in magnitude, with the critical mode being the largest. In the nonlinear regime, the pattern was observed to saturate and the width of the power spectrum decreased with time. Several independent simulations were performed and the results were averaged over the ensemble of independent runs. The average power spectra were seen to sharpen with time about $q = q_{max} \approx 1$. Note that the resolution of these simulations was not fine enough to distinguish q_{max} from the critical wavenumber and the wavenumber that minimizes the potential functional, q_{min}.

(ii) $\epsilon \neq 0$

With non-zero noise, the dependence on initial conditions was lost. In the linear regime, the various modes grew as in the deterministic case. In the nonlinear regime, however, the power spectrum in a single run had a peak at different wavenumbers as time passed. At long times, the power spectrum in a single run was broad, although peaked about a wavenumber close to one, as before. From this, the authors concluded that the pattern could not be characterized by a single wavenumber. Instead, the authors proposed that the number of zero-crossings or nodes in the pattern may be a better measure of the periodicity. The number of nodes was found to be almost constant in time, and was determined immediately after the linear regime. This quantity appeared to completely determine the wavenumber of the asymptotic pattern.

In related studies, Hernández-García et al. [60, 55] found that for the Swift-Hohenberg equation, the presence of noise smears the boundaries of the Eckhaus band, resulting in a smooth transition region between stable and unstable wave-numbers. It was also found that the time evolution of the dominant wave-number obeyed a scaling form.

4.3 Summary

In summary, the authors demonstrated that the noise erases the dependence on initial conditions and drives the system towards a state in which the average power spectrum is peaked about a particular wavenumber. This wavenumber was found to be almost equal to the critical wavenumber and the wavenumber of the minimum of the potential. These observations are unsurprising, because the stationary probability distribution for a stochastic system evolving in a potential is always peaked about the state which minimizes the potential.

Chapter 5

Wavenumber Selection in the Noisy

SKS Equation: Part I

In this chapter, we begin our study of the role of noise as a mechanism for wavenumber selection in the stabilized Kuramoto-Sivashinsky (SKS) equation. First, we will summarize some of the existing work on noise-induced selection in the SKS equation. We will then present new results of large-scale simulations of the noisy SKS equation. These results have been published in Ref. [7].

5.1   Previous Studies of Wavenumber Selection

For the case of the SKS equation, Obeid et al. [5] and Qiao et al. [6] have recently investigated noise induced wavenumber selection. We review their results, which are relevant to our work. Obeid et al. carried out direct numerical simulations of the noisy SKS equation,

$$\partial_t u(x,t) = -\alpha u - \partial_x^2 u(x,t) - \partial_x^4 u(x,t) + (\partial_x u(x,t))^2 + \zeta(x,t) \qquad (5.1)$$

where $\zeta(x,t)$ is an additive Gaussian noise satisfying,

$$\langle \zeta(x,t) \rangle = 0 \qquad (5.2)$$

and

$$\langle \zeta(x,t)\zeta(x',t') \rangle = 2\varepsilon\delta(x-x')\delta(t-t') \qquad (5.3)$$

The distribution of noise trajectories is given by

$$\rho\left[\zeta(x,t)\right] \propto exp\left[-\frac{1}{2\varepsilon}\int \zeta(x,t)^2 \, dt\right] \qquad (5.4)$$

Here ε is the variance of the distribution and is a measure of the width of the distribution. We will refer to it as the "noise strength". Eq. (5.1) was discretized using a simple finite difference scheme and the time integration was performed using the explicit forward Euler method. To determine the selected wavenumber, the authors simulated Eq. (5.1) starting with the system placed in any one of the deterministic periodic steady states. If the noise enabled the system to escape from the initial state, that state was designated to be unstable with respect to noise. For example, when $\alpha = 0.24$, it was found that the state with $q = 0.6995$ was most stable, in the sense that the system could not be knocked out of this state for 10^8 time steps, with noise strengths up to $\varepsilon = 5 \times 10^{-4}$. All other initial states were destabilized by the noise. Thus, the state with wavenumber $q = 0.6995$ was the selected wavenumber for $\alpha = 0.24$.

Similar simulations were carried out for $\alpha = 0.20$ and $\alpha = 0.17$. Smaller values of α were not considered because of the existence of the time-dependent states described in Chapter 2. As $\alpha_c - \alpha$ increased, no unique state could be identified as being most stable. For $\alpha = 0.2$, it was found that states with $0.650 \le q \le 0.712$ all remained stable up to 10^8 time steps and noise strengths up to $\varepsilon = 2 \times 10^{-3}$. Similarly, for $\alpha = 0.17$, states with $0.650 \le q \le 0.699$ were found to remain stable at 10^8 time steps and noise strengths up to $\varepsilon = 2 \times 10^{-3}$. It was therefore concluded that very long computational times would be required to destroy the
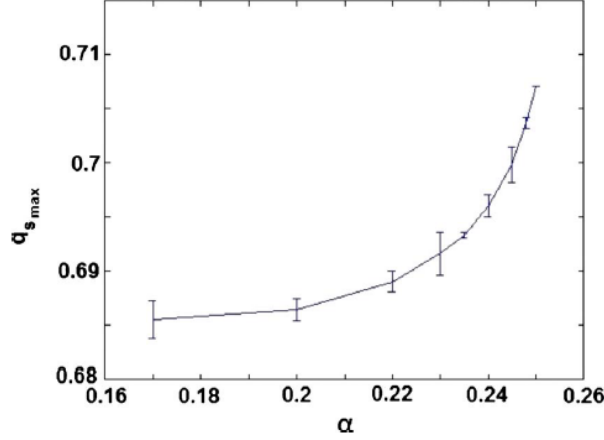
Figure 5.1: Selected wavenumber determined from the maximum of the phase diffusion coefficient $D_{||}$. Reproduced from Ref. [5].

stability of the states. Because of the computational limitations associated with the explicit Euler method, it was practically infeasible to run longer simulations. Thus, although the authors proved that the band of stable states became narrow in the presence of noise, they could not directly demonstrate the selection of a unique wavenumber for $\alpha < 0.24$.

The authors then attempted to find the selected wavenumber by determining the phase diffusion coefficient ($D_{||}$ described in Chapter 1) for various wavenumbers and fixed α. From the analysis of the phase diffusion equation, it is known that states with wavenumber q are stable to long wavelength perturbations if $D_{||}(q) > 0$. The selected state was then identified by the authors as the one that maximized the function $D_{||}(q)$. The selected wavenumber obtained in this way is shown as a function of control parameter in Fig. 4.1, reproduced from Ref. [5].

A more recent study of state selection in the SKS equation was conducted by Qiao et al. [6]. They used the least action principle of Freidlin-Wentzell theory [61] to calculate transition probabilities between pairs of periodic steady states for the SKS equation. The Freidlin-Wentzell theory for computing path probabilities for stochastic processes is summa-

rized below. For the following stochastic process defined on a spatial domain $[0, L]$,

$$\dot{\Phi}(x,t) = f[\Phi(x,t)] + \zeta(x,t) \tag{5.5}$$

the probability of a particular trajectory $\Phi(x,t) = \phi(x,t)$ defined over a time interval $[0,\ \mathrm{T}]$ is,

$$P_T[\phi(x,t)] = \mathcal{C} \ \exp[-S_T[\phi(x,t)]/\varepsilon] \tag{5.6}$$

where $\mathcal{C}$ is a normalization constant independent of $\phi(x,t)$, ε is the noise strength defined by,

$$\langle \zeta(x,t)\zeta(x',t') \rangle = 2\varepsilon\delta(x-x')\delta(t-t') \tag{5.7}$$

and $S_T[\phi(x,t)]$ is the action, given by,

$$S_T[\phi(x,t)] = \frac{1}{2} \int_0^T \mathrm{d}t \int_0^L \mathrm{d}x[\dot{\phi}(x,t) - f[\phi(x,t)]]^2 \tag{5.8}$$

Eq. (5.6) implies that the most probable trajectory connecting two states of the system is the one which minimizes the action. The most likely paths entering and leaving successive periodic states of the SKS equation were computed by finding the minimum action for transitions between those states (for example, $S^*_{q_j \to q_{j+1}}$ is the minimum action to go from a periodic state with wavenumber q_j to one with wavenumber q_{j+1}, and $S^*_{q_{j+1} \to q_j}$ is the minimum action for the reverse transition). These values were then used to determine the net direction of transitions between two adjacent states. By implementing this procedure for all pairs of successive steady states, the wavenumber corresponding to the selected state was found. Notably, their estimates of the selected wavenumber did not agree with those obtained by Obeid et. al using the phase diffusion coefficient.

5.2 Calculating the Empirical Probability Distribution of Final States

In this section, we lay the theoretical foundation needed to interpret our numerical results. Qiao et al. and Obeid et al. have devised indirect ways to calculate the selected wavenumber for the SKS problem. However, it would be useful to verify their results by performing a direct integration of the equation of motion. There are two practical difficulties associated with this. The first is that states in the Eckhaus band become more and more stable as $\alpha_c - \alpha$ increases [5]. To compare the relative stability of these states, one has to induce transitions between these states, so that the state in which the system spends most of its time is the most stable state. Observing such transitions between highly stable states requires extremely long integration times, as noted in [5]. The second problem is that numerical simulations are necessarily performed on finite systems. In a finite system, the set of accessible wavenumbers is discrete. The gap between these wavenumbers is inversely proportional to the number of lattice points. Thus, to get a precise estimate of the selected wavenumber, it is important to simulate very large systems. These two hurdles suggest that one look for a fast and efficient integration algorithm. Here, we use a semi-implicit, Fourier spectral integration method [62]. Using a Fourier spectral method is especially convenient for problems with periodic states, in addition to being much more accurate than finite difference methods [63]. On the other hand, using a semi-implicit time integration scheme allows one to use a significantly larger time step without compromising on accuracy, yielding a much higher speed of integration. The general idea behind the semi-implicit Fourier method is as follows. Consider the following partial differential equation,

$$\frac{\partial u(x,t)}{\partial t} = \hat{\mathbf{L}} u(x,t) + \hat{\mathbf{N}}[u(x,t), \partial_x u(x,t), \partial_x^2 u(x,t), \dots] \tag{5.9}$$

where $\hat{\mathbf{L}}$ is a linear differential operator and $\hat{\mathbf{N}}$ is a nonlinear functional of u and its spatial derivatives. We discretize space into N (not to be confused with $\hat{\mathbf{N}}$) grid points with lattice spacing h and denote the value of the field $u(x,t)$ at each grid point by $u(mh,t) = u_m(t)$. Then Eq. (5.9) reduces to a system of ordinary differential equations,

$$\frac{du_m}{dt} = (\hat{\mathbf{L}}u)_m + \hat{\mathbf{N}}[u(x,t),\dots]_m \qquad m = 0,1,\dots,N-1. \tag{5.10}$$

We define the discrete Fourier transform (DFT) of u_m as

$$\widetilde{u}_n(t) = \sum_{m=0}^{N-1} u_m(t)\,\exp\left[\frac{-2\pi imn}{N}\right]; \tag{5.11}$$

$$n = 0,1,\cdots,N/2-1,-N/2,\cdots,-1$$

Each n corresponds to a wave number q_n given by

$$q_n = \frac{2\pi n}{L} = n\Delta q \tag{5.12}$$

Taking the DFT of Eq. (5.10) gives

$$\frac{d\widetilde{u}_n}{dt} = \widetilde{(\hat{\mathbf{L}}u)}_n + \widetilde{\hat{\mathbf{N}}}_n \qquad n = 0,1,\dots,\frac{N}{2}-1,-N/2,\dots,-1 \tag{5.13}$$

For the (deterministic) SKS equation,

$$\hat{\mathbf{L}}u(x,t) = -\alpha u(x,t) - \partial_x^2 u(x,t) - \partial_x^4 u(x,t) \tag{5.14}$$

and

$$\hat{\mathbf{N}}[u(x,t),\partial_x u(x,t)] = (\partial_x u(x,t))^2 \tag{5.15}$$

The nth component of the DFT of Eq. (5.14) is [63] (see also Appendix A.1),

$$(\widetilde{\hat{\mathbf{L}}u})_n = -\alpha\widetilde{u}_n + (2\pi n/Nh)^2\widetilde{u}_n - (2\pi n/Nh)^4\widetilde{u}_n \tag{5.16}$$

The nth component of the DFT of the nonlinear term can be obtained from the discrete convolution theorem (Appendix A.1).

$$\widetilde{\hat{\mathbf{N}}}_n = \left(\frac{1}{N}\right)\left(\frac{2\pi}{L}\right)^2 \sum_{n_1=-N/2+1}^{N/2-1} \widetilde{v}_{n_1}\widetilde{v}_{n-n_1} \tag{5.17}$$

where $\widetilde{v}_n$ is the nth component of the DFT of $\partial_x u$, given by $(2\pi i n/Nh)\widetilde{u}_n$ for all n. In practice, evaluating the nonlinear term $\widetilde{\hat{\mathbf{N}}}_m[u(x,t),\dots]$ in Fourier space directly is computationally expensive, since the convolution involves $O(N^2)$ computations. Therefore, in our simulations, we compute the nonlinear term in position space and then transform it back to Fourier space. Putting all this together, we get,

$$\frac{d\widetilde{u}_n}{dt} = -\alpha\widetilde{u}_n + (2\pi n/Nh)^2\widetilde{u}_n - (2\pi n/Nh)^4\widetilde{u}_n + \widetilde{\hat{\mathbf{N}}}_n[u(x,t),\dots] \tag{5.18}$$

We now describe the semi-implicit time integration scheme. It involves treating the linear terms implicitly and the nonlinear term explicitly [62]. In other words, to solve for the value of $\widetilde{u}_n$ at time t_{j+1}, we evaluate the linear part of the right side of Eq. (5.18) at time t_{j+1} (implicit time integration) and the nonlinear part at time t_j (explicit time integration). Approximating the left side of Eq. (5.18) as $du_n^j/dt = \frac{u_n^{j+1}-u_n^j}{\Delta t}$ and solving for $\widetilde{u}_n^{j+1}$ yields,

$$u_n^{j+1} = \frac{u_n^j + \Delta t\widetilde{\hat{\mathbf{N}}}_n^j}{1 - \Delta t\left[-\alpha + \left(\frac{2\pi n}{Nh}\right)^2 - \left(\frac{2\pi n}{Nh}\right)^4\right]} \tag{5.19}$$

With this semi-implicit scheme, it is possible to increase the time step by a factor of about 50 compared to that in an explicit time integration scheme, without causing instabilities and without loss of accuracy. This was tested by integrating the deterministic SKS equation

using a simple explicit Euler algorithm with $\Delta t \sim \mathcal{O}(10^{-4})$ and comparing the results with those obtained from the semi-implicit method (see also [62]). This results in a significant speed up of the algorithm. Finally, in order to incorporate noise, we let ζ_n^j denote the value of the noise term at time t_j and Eq. (5.19) is modified to read,

$$u_n^{j+1} = \frac{u_n^j + \Delta t \widetilde{\mathbf{N}}_n^j + \sqrt{\frac{2\varepsilon N \Delta t}{h}} \zeta_n^j}{1 - \Delta t \left[-\alpha + \left(\frac{2\pi n}{Nh} \right)^2 - \left(\frac{2\pi n}{Nh} \right)^4 \right]} \tag{5.20}$$

where $\langle \zeta_n^j \rangle = 0$ and $\langle \zeta_n^j \zeta_{n'}^{j'} \rangle = \delta_{n,-n'} \delta_{jj'}$. The procedure for generating noise in Fourier space which satisfies equations Eqs. (5.2) and (5.3) is given in Appendix B of Ref. [17].

5.3   Results

Our aim is to compute the empirical probability distribution for the allowed periodic states by using the algorithm in Eq. (5.20). If the distribution has a peak at a particular wavenumber, it would support the hypothesis that noise is a possible mechanism of wavenumber selection.

Before computing the probabilities, however, we must address two technical issues. First, we must clarify how to determine the "state" of the system at time t. Because of the noise, the state of the system at any given time has a broad power spectrum, with non-zero components for several wavenumbers. In position space, the configuration retains its cellular shape but is irregular. Hence, it is inaccurate to say that the system is *in* a given periodic state. Hence, we adopt the following criterion: the system is considered to be in a state with wave number $q_n = 2\pi n/L$ at time t if

$$|\widetilde{u}_n(t)| \geq 2|\widetilde{u}_{n'}(t)| \text{ for all } n' \neq n \tag{5.21}$$

where both n and n' are non-zero. This criterion ensures that only those states were counted in which one mode is much larger than all others, and highly disordered configurations with several wave numbers having roughly the same Fourier amplitude are disregarded.

The second issue is determining an appropriate noise strength for the simulations. First, taking our computational resources into account, we fix the run time at T for all the simulations. To obtain accurate stationary probability distributions of wave numbers, it is important to be able to sample all accessible states in time T. If the noise strength is too small, the system is likely to get stuck near one periodic state for the entire simulation. Thus, we define a threshold noise strength $\varepsilon_{min}(\alpha, N, T)$ above which the entire set of states can be sampled and stationary histograms can be attained *in time T*. The arguments emphasize that ε_{min} depends not only on α but also on the run time and the system size. It is thus a practical choice which is dictated by computational restraints. For example, increasing the run time T while keeping α and N fixed leads to a smaller value of ε_{min}. On the other hand, increasing N while keeping T fixed increases ε_{min}. By fixing the system size N and simulation time T, ε_{min} can be determined for each α. All our simulations are performed with $\varepsilon \geq \varepsilon_{min}$.

The empirical probability density can now be obtained from the average of the *indicator function* for a state with wavenumber q,

$$M_T(q) = \frac{1}{T} \int_0^T \mathbf{1}_q(t) \, \mathrm{dt} \tag{5.22}$$

Let the system be in a state with wavenumber k (according to the criterion in Eq. (5.21)). The indicator function is defined by,

$$\mathbf{1}_q(t) = \begin{cases} 1 & k = q \text{ at time } t \\ 0 & \text{otherwise} \end{cases} \tag{5.23}$$

This quantity gives the fraction of time spent near the state with wavenumber q and approaches the stationary probability distribution of wavenumbers at very long times.

$$\lim_{T \to \infty} M_T(q) = P_{st}(q) \tag{5.24}$$

We are now in a position to present our results. Since wavenumber selection has already been demonstrated for a small system with control parameter $\alpha = 0.24$ in [5], we carry out the procedure described above for $\alpha = 0.22$. In accordance with Obeid et al. we restrict our simulations to the interval $0.16 < \alpha < 0.25$, for reasons described above. We set the lattice spacing to $h = 0.5$, the time step to $\Delta t = 0.3$ and set the total integration time to $T \approx 2 \times 10^8 \Delta t = 5 \times 10^7$. We perform simulations for several values of N.

For $\alpha = 0.22$, wavenumbers lying in the range $0.6136 \leq q \leq 0.7486$ are unstable to perturbations [2]. For all our simulations, the initial condition is of the form $u_{in} \sim \sin(2\pi n_{in} x / Nh)$ with n_{in} being an integer. For the range $0.6136 \leq q \leq 0.7486$, and $N = 1024$, $h = 0.5$, we have $50 \leq n \leq 61$.

We start with a small noise strength $\varepsilon = 10^{-4}$ to determine the set of most stable periodic states. We find that the states with $n = 54, 55, 56$ are all very stable to noise. The system is unable to escape from any one of these states during time T. We gradually increase ε and find that at $\varepsilon = 1.8 \times 10^{-3}$, transitions between the $n = 54, 55$ and 56 states become possible, with the $n = 55$ ($q = 0.6749$) state being the most visited one. The histogram of visited wavenumbers has a maximum at this wavenumber which persists until the end of the integration. The histogram also narrows with time, indicating that the system spends most of its time close to the $n = 55$ state.

We also perform simulations with higher values of ε. We see that the maximum of the histogram is still at the $n = 55$ state, although the histogram is broadened as expected. The observation that the most visited state remains the same in spite of increasing the noise strength is promising evidence of the selection of a unique state by noise. For concreteness, we also repeat these simulations with different initial states and find that the wavenumber corresponding to the maximum of the histogram remains the same. This also points to the existence of a unique selected wavenumber. The histograms are shown in Fig, 5.2 (a).

Finally, we check the dependence of the selected wavenumber on the system size N. We plot histograms for the same value of α and ε, but a larger system size $N = 4000$ in Fig. 5.2
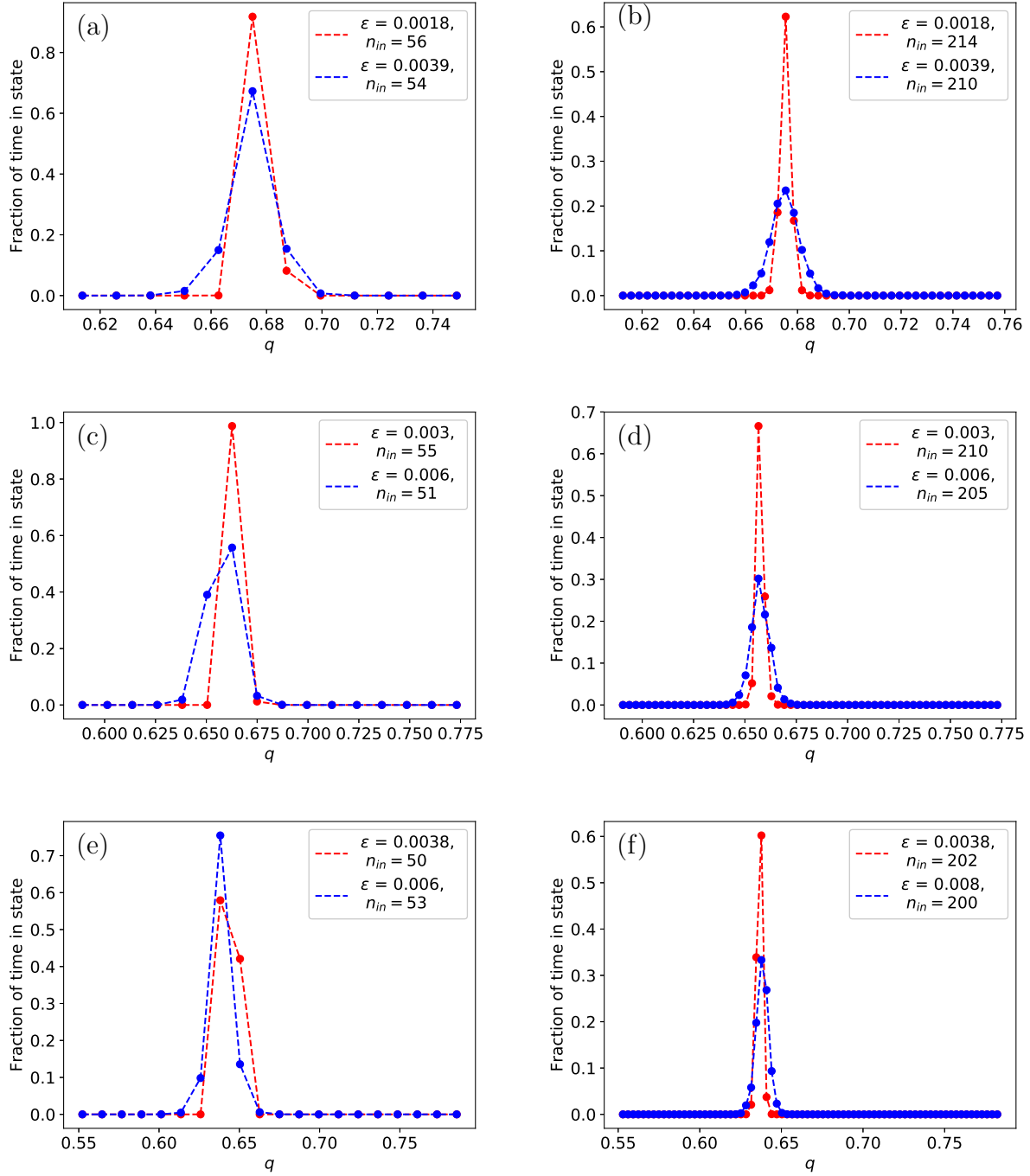
Figure 5.2: Empirical probability distributions for various control parameter values and small and large system sizes. (a) $\alpha = 0.22$, $N = 1024$. (b) $\alpha = 0.22$, $N = 4000$. (c) $\alpha = 0.20$, $N = 1024$. (d) $\alpha = 0.20$, $N = 4000$. (e) $\alpha = 0.17$, $N = 1024$. (f) $\alpha = 0.17$, $N = 4000$

(b). Immediately we notice that the histograms are narrower compared to those obtained for $N = 1024$. The peaks of the histograms are at a wavenumber which is very close to the selected wavenumber found for $N = 1024$ [1]. We also perform simulations for $N = 1600$, 2200 and 3000. In general, we observe that the histogram for a fixed noise strength becomes narrower as N increases. Hence, the most precise estimate of the selected wavenumber is obtained for the largest system size i.e. $N = 4000$. For this size, the difference between two successive wavenumbers is the smallest and is equal to $\Delta q = 2\pi/Nh = 0.003$. The most visited states for $\alpha = 0.22$ are presented in Table. 5.1. Thus, we see that our best estimate for the selected wavenumber for $\alpha = 0.22$ is $q_s = 0.6754 \pm \Delta q/2$ or $q_s = 0.6754 \pm 0.0015$, corresponding to the case $N = 4000$.

Next, we repeat the same process for other values of α. The Eckhaus band becomes wider as α is reduced from the critical value [5]. Furthermore, the states in the Eckhaus band become more stable to noise for smaller values of α, necessitating the use of larger noise strengths. For $\alpha = 0.20$ and $N = 1024$, the Eckhaus stable wavenumbers are $0.5890 \leq q \leq 0.7608$ or $48 \leq n \leq 62$. For a range of noise strengths between 3×10^{-3} and 6×10^{-3} and different initial conditions, we find $n = 54$ ($q = 0.6627$) to be the most visited state (Fig. 5.2(c)). For $N = 4000$ lattice points, we find $n = 209$ to be the most visited state, see Fig. 5.2(d). Results for various system sizes are shown in Table 5.2. Finally, results for $\alpha = 0.17$ are shown in Table 5.3 and Fig. 5.2(e) and (f).

For the sake of completeness, we have also reproduced Obeid's result for $\alpha = 0.24$ and extended it to larger sizes, as shown in Table 5.4.

The power spectra at the end of integration for $\alpha = 0.22$ and low and high noise strengths are shown in Fig. 5.3. These figures show that the final power spectra have prominent maxima at the most visited wavenumber, in spite of the large noise strengths we have used. Small but visible second harmonic peaks are also observed, indicating that the system is close to a periodic steady state of the deterministic system. The power spectra for $\alpha = 0.20$

---

[1]The selected wavenumbers for two different system sizes are not exactly equal because the discrete set of wavenumbers accessible in the simulation depends on the system size.
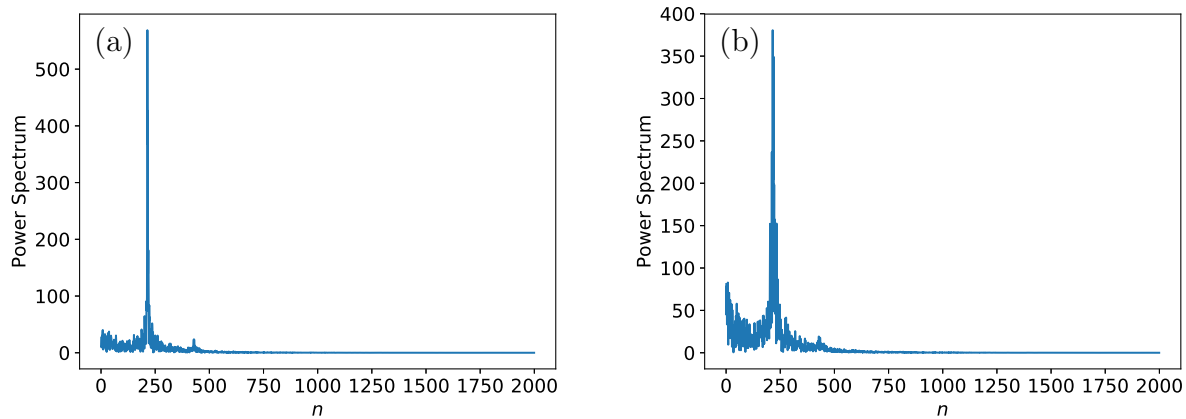
Figure 5.3: Long time power spectra for $\alpha = 0.22$ and 4000 lattice points. We have plotted the number of cells n in the solution on the x axis for visual clarity. (a) $\varepsilon = 0.0018$. (b) $\varepsilon = 0.0039$.

and 0.17 are similar. Note that we have plotted the number of cells n on the x axis, instead of the wavenumber.

We also show plots of the field $u(x,t)$ (for $\alpha = 0.22$ and 1024 lattice points) at very long times in Fig. 5.4. Fig 5.4(a) corresponds to $\varepsilon = 0.0018$, while Fig. 5.4(b) is for $\varepsilon = 0.0039$. Finally, a plot of the selected wavenumbers for 4000 lattice points against α is shown in Fig. 5.5, with error bars representing the discretization error. It also shows the results obtained in [6] for the same values of α. Both curves show that as the value of α is decreased below threshold, the selected wavenumber is shifted to the left of the critical wavenumber q_c (horizontal line in Fig. 5.5). However, our values for the selected wavenumber do not agree with theirs far from $\alpha = \alpha_c$. The reason for the disagreement is likely numerical. Since the disagreement is particularly large away from threshold, it is possible that the use of the amplitude equation in Ref. [6] may be inappropriate. It is possible, for example, that the saddle solution for the amplitude equation is not a sufficiently accurate initial guess for the true saddle state for α values far from α_c. Secondly, the time reversed deterministic path is the minimum action path only for potential systems [6]. While it is reasonable to assume that it would be a good initial guess for non-potential systems, it is also possible that the actual minimum action path is far more complicated away from threshold, where the non-potential
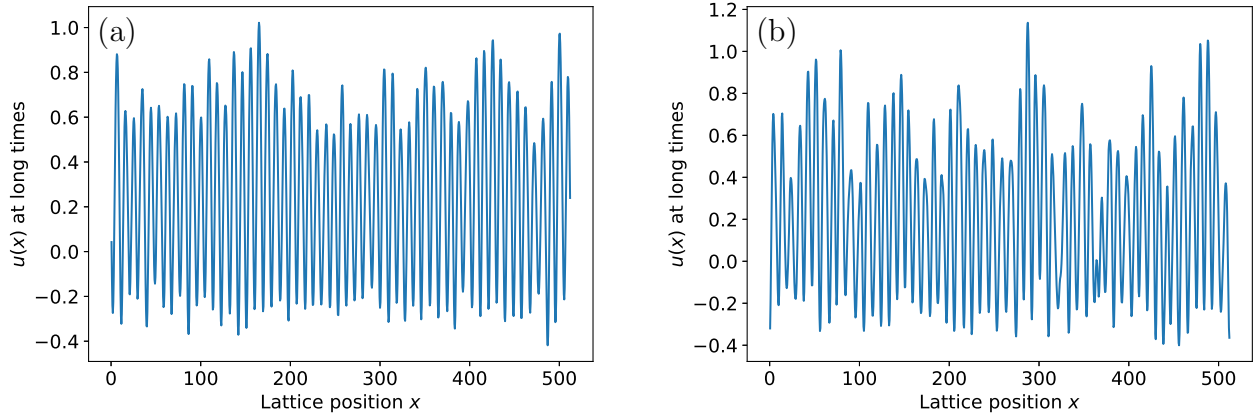
Figure 5.4: Typical final configurations at the end of integration for $\alpha = 0.22, 1024$ lattice points. (a) $\varepsilon = 0.0018$ (b) $\varepsilon = 0.0039$

term in Eq. (5.1) is not small. The discretized action is a function of the discretized field at all lattice points and all times, and hence could be an extremely complicated function, with possibly multiple minima. It is not clear what kind of numerical uncertainties arise in minimizing this action, and whether the minimum action paths found in [6] are local minima or global minima. A thorough analysis of the optimization techniques is needed to explore these issues.

Number of lattice points N	System Length $(L = Nh)$	Most visited state
1024	512	0.6749 $(n = 55)$
1600	800	0.6754 $(n = 86)$
2200	1100	0.6740 $(n = 118)$
3000	1500	0.6744 $(n = 161)$
4000	2000	0.6754 $(n = 215)$

Table 5.1: Most visited wavenumbers for various sizes, $\alpha = 0.22$.

Number of lattice points N	System Length $(L = Nh)$	Most visited state
1024	512	0.6627 $(n = 54)$
1600	800	0.6597 $(n = 84)$
2200	1100	0.6569 $(n = 115)$
3000	1500	0.6576 $(n = 157)$
4000	2000	0.6566 $(n = 209)$

Table 5.2: Most visited wavenumbers for various sizes, $\alpha = 0.20$.

Number of lattice points N	System Length ($L = Nh$)	Most visited state
1024	512	0.6381 ($n = 52$)
1600	800	0.6361 ($n = 81$)
2200	1100	0.6340 ($n = 111$)
3000	1500	0.6367 ($n = 152$)
4000	2000	0.6377 ($n = 203$)

Table 5.3: Most visited wavenumbers for various sizes, $\alpha = 0.17$.

Number of lattice points N	System Length ($L = Nh$)	Most visited state
1024	512	0.6995 ($n = 57$)
1600	800	0.6990 ($n = 89$)
2200	1100	0.6969 ($n = 122$)
3000	1500	0.6953 ($n = 166$)
4000	2000	0.6974 ($n = 222$)

Table 5.4: Most visited wavenumbers for various sizes, $\alpha = 0.24$.

5.3.1 Extension to thermodynamic limit

It is interesting to note that the probability distributions we have obtained sharpen about the selected wavenumber as the system size is increased. This appears to be surprising, because the number of accessible wavenumbers increases with system size and hence, one would expect the histograms of Fig. 5.2 to become wider when the system size is increased. The emergence of new modes is, in fact, seen in Fig. 5.2(b), (d) and (f). However, the crucial observation is that these newly excited wavenumbers lie in a narrower band than the excited wavenumbers for a smaller system.

Based on the above observations, it is reasonable to suppose that the discrete probability distributions obtained for finite system sizes can be used to estimate the selected wavenumber for an infinite system (for which there exists a continuous band of allowed wavenumbers). We use cubic spline interpolation to smoothly interpolate between the discrete points. The maximum of the interpolated continuous curve is the selected wavenumber q_s. The interpolated curves for $\alpha = 0.22, 0.20$ and 0.17 are shown in Figs. 5.6 through 5.8. Our continuum estimates for the selected wavenumbers are given in Table 5.5.
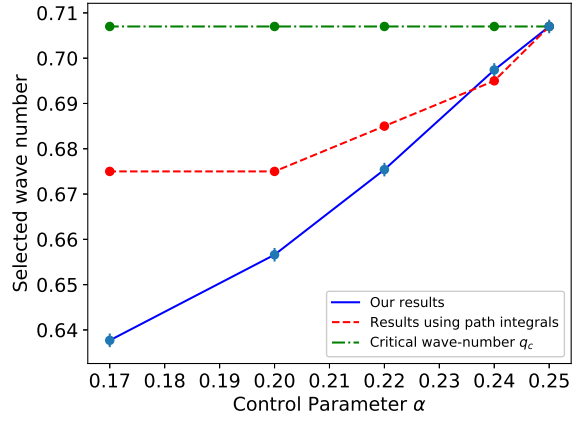
Figure 5.5: Comparison of our results with those of [6]. The horizontal line represents the critical wavenumber $q_c = \frac{1}{\sqrt{2}}$, which is the fastest growing wavenumber in the linear stability analysis.
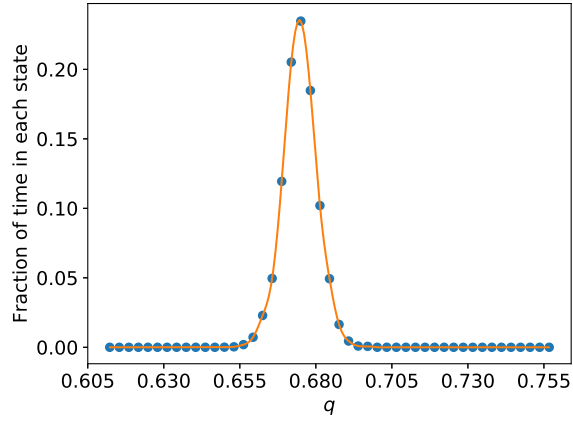
Figure 5.6: Interpolating curve for $\alpha = 0.22$, with a maximum at $q_s = 0.6748$.
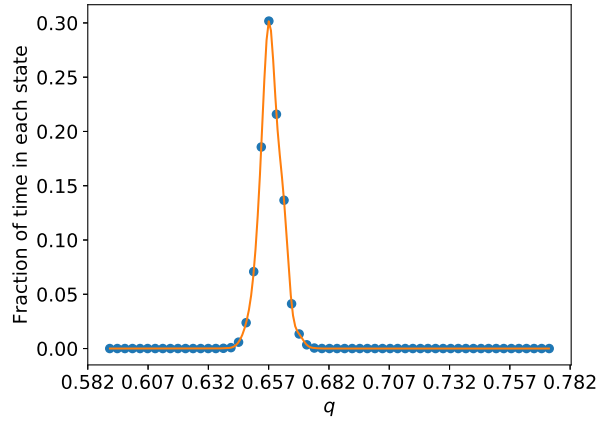
Figure 5.7: Interpolating curve for $\alpha = 0.20$, with a maximum at $q_s = 0.6567$

62
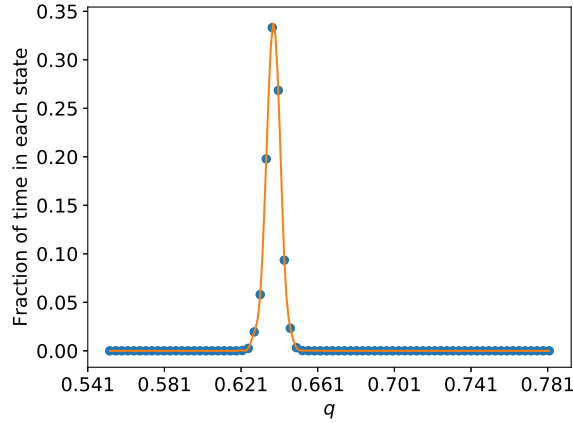
Figure 5.8: Interpolating curve for $\alpha = 0.17$, with a maximum at $q_s = 0.6384$.

Control Parameter α	q_s
0.22	0.6748
0.20	0.6567
0.17	0.6384

Table 5.5: Most visited or selected wavenumbers q_s in the thermodynamic limit.

5.4 Summary

In this chapter, we have presented new simulations of the noisy SKS equation. Using a fast, efficient code we have accessed very long time scales and large systems to obtain precise estimates of the selected wavenumbers over the entire relevant range of control parameter values. Our results disagree with those of Refs. [5, 6], but we have proposed plausible qualitative explanations for the discrepancy.

Chapter 6

Wavenumber Selection in the Noisy SKS Equation: Part II

In the last chapter, we presented the results of simulations of the SKS equation supplemented with additive noise. We performed long-time simulations of the equation and obtained the stationary probability distributions of wavenumbers. These distributions were found to be peaked at a unique wavenumber, provided that the applied noise was strong enough. The selected wavenumber found in this way was always less than the critical wavenumber q_c. While the stationary histograms provide a convincing demonstration of the importance of noise in selecting a unique wavenumber, they do not tell us how the stationary distribution is attained. Furthermore, they do not give any insight into why the selected wavenumber is less than the critical wavenumber.

In this chapter, we shift our focus from the stationary probability distributions to the time evolution of the various Fourier components of the field $u(x,t)$. By doing so we identify the key process responsible for noise-induced selection in the SKS model. Through a detailed numerical analysis, we show that the noise fundamentally alters the nonlinear dynamics of the SKS equation in two ways. First, it causes the growth of modes with wave numbers close to zero in the nonlinear regime. Second, it couples these small wave number modes with the

Table 6.1: Noise-selected wave numbers as found in Ref. [7].

Control Parameter α	$q^\star$ $(L = 2000) = 2\pi n^\star/Nh$
0.24	0.6974 ($n^\star = 222$)
0.22	0.6754 ($n^\star = 215$)
0.20	0.6566 ($n^\star = 209$)
0.17	0.6377 ($n^\star = 203$)

Eckhaus stable modes in a way that opposes the growth of modes close to the critical one. The results given below are published in Ref. [64].

6.1 Analysis of Dynamics

For convenience, we list the selected wavenumbers for $N = 4000$ lattice points from the previous chapter in 6.1. For the remainder of this chapter, these wavenumbers will be denoted as $q^\star = 2\pi n^\star/Nh$. Also note that for brevity, we will refer to the procedure of obtaining stationary histograms from a single long run as the "histogram method". We will repeatedly compare the histogram method with the simulations reported in this chapter.

To study the dynamics of individual Fourier modes, it is natural to focus on the time evolution of the structure function $S_n(t) = \langle|\widetilde{u}_n(t)|^2\rangle = \langle\widetilde{u}_n(t)\widetilde{u}_{-n}(t)\rangle$, where the angular brackets denote an average over independent trajectories. We begin by writing the discrete form of the noisy SKS equation.

$$\frac{d\widetilde{u}_n}{dt} = -\alpha\widetilde{u}_n + (2\pi n/Nh)^2\widetilde{u}_n - (2\pi n/Nh)^4\widetilde{u}_n + \widetilde{\mathbf{N}}_n[u(x,t),\dots] + \zeta_n(t) \qquad (6.1)$$

Using Eq. (6.1), we can derive an equation for the time derivative of S_n as follows.

$$\dot{S}_n(t) = \langle\dot{\widetilde{u}}_n(t)\widetilde{u}_{-n}(t)\rangle + \langle\widetilde{u}_n(t)\dot{\widetilde{u}}_{-n}(t)\rangle \qquad (6.2)$$

The dot denotes the time derivative. Using Eqs. (5.18) and (5.17), we obtain,

$$\dot{S}_n(t) = 2\sigma_n S_n(t) + \langle \widetilde{u}_n \widetilde{\zeta}_{-n} \rangle + \langle \widetilde{u}_{-n} \widetilde{\zeta}_n \rangle +$$

$$\frac{1}{N} \left[\sum_{n_1=-N/2+1}^{N/2-1} \langle \widetilde{v}_{n_1} \widetilde{v}_{-n-n_1} \widetilde{u}_n \rangle \right. \tag{6.3}$$

$$\left. + \sum_{n_1=-N/2+1}^{N/2-1} \langle \widetilde{v}_{n_1} \widetilde{v}_{n-n_1} \widetilde{u}_{-n} \rangle \right]$$

where $\sigma_n = -\alpha + q_n^2 - q_n^4$ is the linear operator appearing in Eq. (6.1) and $\widetilde{v}_n$ is the nth component of the DFT of $\partial_x u$ as defined in Chapter 5. We can split the sums over n_1 as follows,

$$\sum_{-N/2+1}^{N/2-1} = \sum_{-N/2+1}^{-1} + \sum_{1}^{N/2-1} \tag{6.4}$$

The term in square brackets in Eq. (6.3) then becomes,

$$\sum_{n_1=-N/2+1}^{-1} \langle \widetilde{v}_{n_1} \widetilde{v}_{-n-n_1} \widetilde{u}_n \rangle + \sum_{n_1=1}^{N/2-1} \langle \widetilde{v}_{n_1} \widetilde{v}_{-n-n_1} \widetilde{u}_n \rangle$$

$$+ \sum_{n_1=-N/2+1}^{-1} \langle \widetilde{v}_{n_1} \widetilde{v}_{n-n_1} \widetilde{u}_{-n} \rangle + \sum_{n_1=1}^{N/2-1} \langle \widetilde{v}_{n_1} \widetilde{v}_{n-n_1} \widetilde{u}_{-n} \rangle \tag{6.5}$$

The second and third terms of Eq. (6.5) are complex conjugates as are the first and last terms. Since $z + z^\star = 2 \, Re(z)$ for a given complex number z, the above reduces to

$$\sum_{n_1=1}^{N/2-1} 2 \, \mathrm{Re} \langle \widetilde{v}_{n_1} \widetilde{v}_{-n-n_1} \widetilde{u}_n \rangle + (n \rightarrow -n)$$

Substituting this expression into Eq. (6.3), we get the expression for the time derivative

of the structure function

$$\dot{S}_n(t) = 2\sigma_n S_n(t) + 2 \ Re \ \langle \widetilde{u}_n \widetilde{\zeta}_{-n} \rangle +$$

$$\sum_{n_1=1}^{N/2-1} [2 \ Re \langle \widetilde{v}_{n_1} \widetilde{v}_{-n-n_1} \widetilde{u}_n \rangle + (n \rightarrow -n)] \tag{6.6}$$

We can make this expression more compact by defining

$$\mathcal{S}_{n,n_1} = 2 \ Re \langle \widetilde{v}_{n_1} \widetilde{v}_{-n-n_1} \widetilde{u}_n \rangle \tag{6.7}$$

and

$$\mathcal{N}_n = \frac{1}{N} \sum_{n_1=1}^{N/2-1} (\mathcal{S}_{n,n_1} + \mathcal{S}_{-n,n_1}) \tag{6.8}$$

Equation (6.6) then reduces to

$$\dot{S}_n(t) = 2\sigma_n S_n(t) + 2 \ Re \langle \widetilde{u}_n \widetilde{\zeta}_{-n} \rangle + \mathcal{N}_n \tag{6.9}$$

Finally, we note that from Novikov's theorem [17], $\langle \widetilde{u}_n \widetilde{\zeta}_{-n} \rangle$ is simply a constant proportional to ε. Therefore, this term only contributes a constant to Eq. (6.9) and will henceforth be ignored.

From Eq. (6.9), it is clear that the linear dynamics of the structure function are identical to those of the deterministic SKS equation, with twice the linear growth rate. To understand the effects of the noise, we must therefore study the *nonlinear* dynamics of $S_n(t)$ for various values of n. We do this by integrating Eq. (6.1) for several independent noise realizations over a fixed time interval and averaging over all the realizations to yield the the time evolution of the structure function. For brevity, we will call this procedure the "structure function method". Note that it is also possible to integrate Eq. (6.9) directly, but one would require an appropriate truncation scheme to do so. We do not pursue this method here.

We study two cases of interest. First we obtain $S_n(t)$ with random initial conditions and

zero added noise, i.e. $\varepsilon = 0$. Then we repeat the same procedure, but with $\varepsilon \neq 0$. In each case, we identify a dominant wave number as the one which maximizes S_n at the end of the simulation, and compare it with the results of the histogram method [7]. The difference in the dynamics of S_n for the two cases will shed light on the nature of the selection process. The simulations of the structure function are carried out over time intervals which are shorter than those of the histogram simulations, for reasons explained below. *These time scales and other important symbols are given in Table 6.2.*

6.1.1   Noiseless dynamics with random initial conditions

We set $\alpha = 0.20$, $\varepsilon = 0$ and use random initial conditions drawn from a Gaussian distribution. The lattice consists of $N = 4000$ points, separated by distance $h = 0.5$. We use the same semi-implicit time integration scheme as the previous chapter with time step $\Delta t = 0.3$, and integrate Eq. (6.1) from time $t = 0$ to time $t = T_{S0} = 1.2 \times 10^5$ for 180 independent runs. The subscript $S0$ signifies that we are calculating the structure function with zero noise. This calculation is computationally demanding, forcing us to use a run time which is much shorter than that used in Ref. [7] (see Table 5.2) .

For our parameters, the Eckhaus band is given by $n_E^- \leq n \leq n_E^+$, with $n_E^- = 188$ and $n_E^+ = 246$. This corresponds to $0.589 \leq q \leq 0.767$. The critical wave number is $q_c = 2\pi n_c/L \approx 1/\sqrt{2}$ where $n_c = 225$ and the selected wave number determined from the histogram method is $q^\star = 2\pi \times n^\star/L = 0.6566$ where $n^\star = 209$ [7].

In Fig. 6.1 (a), we show the structure function for $\alpha = 0.20$ and various values of n, including $n = n^\star$ and $n = n_c$. S_{221} and S_{222} are found to have the largest long-time values, with S_{222} being slightly larger. $S_{n^\star}$ and S_{210} decay to very small values, as does S_{n_c}. In Fig. 6.1 (b) and (c), we take a closer look at the early and intermediate time dynamics. At very early times (Fig. 6.1 (b)), S_{n_c} grows faster than all the others, followed by S_{220}, S_{221} and S_{222}. The growth of $S_{n^\star}$ and S_{210} is much slower. This is consistent with the fact that the structure function has the same linear dynamics as the deterministic SKS equation. Around

Symbol	Meaning
T	Time over which the number of hits in each state was measured in Ref. [7]
$\varepsilon_{min}(\alpha, N, T)$	Minimum noise needed to explore all states and obtain stationary histograms in one trajectory of length T, for fixed α and N
$q^\star = 2\pi n^\star / L$	Selected wave number when $(\varepsilon \geq \varepsilon_{min})$ found in Ref. [7].
T_{S0}	Duration of each trajectory in the ensemble of trajectories over which S_n is calculated when $\varepsilon = 0$. Fixed at $1.2 \times 10^5 = 4 \times 10^5 \Delta t$
T_S	Duration of each trajectory in the ensemble of trajectories over which S_n is calculated for $\varepsilon \neq 0$. Fixed at $1.2 \times 10^6 = 4 \times 10^6 \Delta t$
$q_{S0} = 2\pi n_{S0}/L$	Most probable wavenumber identified as the maximum of the structure function S_n at time T_{S0} for the noiseless case.
$q_S(\alpha, \varepsilon, T_S) = 2\pi n_S(\alpha, \varepsilon, T_S)/L$	Most probable wavenumber identified as the maximum of the structure function S_n at time T_S for given noise strength ε.

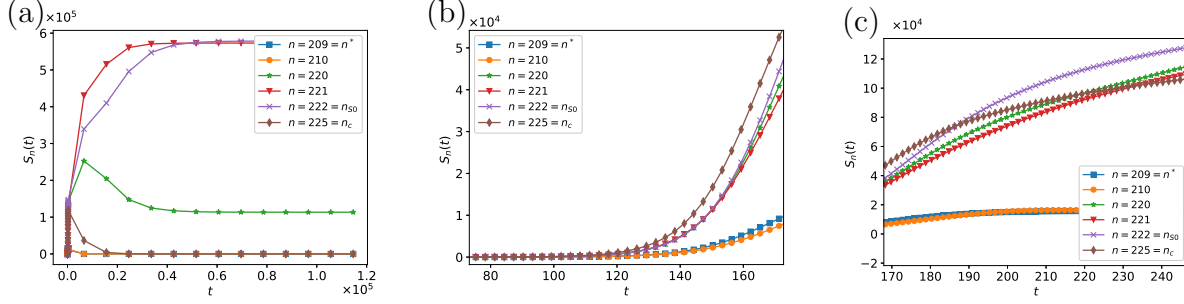Table 6.2: List of important symbols and their meanings.

Figure 6.1: (a) Time evolution of $S_n(t)$ with random initial conditions and $\varepsilon = 0$. (b) The early time regime. (c) Intermediate time regime.

$t \approx 180$, we can see the growth of S_{220}, S_{221}, S_{222} and S_{n_c} slowing down, marking the beginning of the nonlinear regime. A short time later, the growth of S_{n_c} becomes slower and slower (Fig. 6.1 (c)). S_{220}, S_{221} and S_{222} overtake S_{n_c}, while $S_{n^\star}$ and S_{210} start decreasing. Qualitatively, this occurs because the nonlinear terms (which oppose growth) in the equation of motion for $S_{n^\star}$ and S_{210} exceed the linear terms (which favor the growth), rendering the time derivatives $dS_{n^\star}/dt$ and dS_{210}/dt negative. Thus, $S_{n^\star}$ and S_{210} decay to zero.

We conclude that starting from random initial conditions, the system is most likely to end up in a periodic state with wave number $2\pi \times 221/L$ or $2\pi \times 222/L$. In other words, these are the states which are most likely to be realized for typical initial conditions, if the evolution is purely deterministic. *We use the symbol n_{S0} to refer to the $n = 222$ state, meaning that it is the wave number for which S_n is maximum when $\varepsilon = 0$.*

On the other hand, the state with $n = n^\star$, which was the noise-selected state from the last chapter, has a very small probability, as seen from the fact that $S_{n^\star}$ is negligible at the end of integration. The same is true for $n = 210$.

6.1.2 Stochastic dynamics

Next, we repeat the above procedure with $\varepsilon \neq 0$, using random initial conditions as in the previous subsection. For $\alpha = 0.20$, ε_{min} was found to be approximately equal to 0.003 [7]. Here, we set $\varepsilon_{min} = 0.004$, which is slightly greater than ε_{min}. To get a sense of how strong this noise is, we show a scatter plot of the wave number with the maximum power at each

70

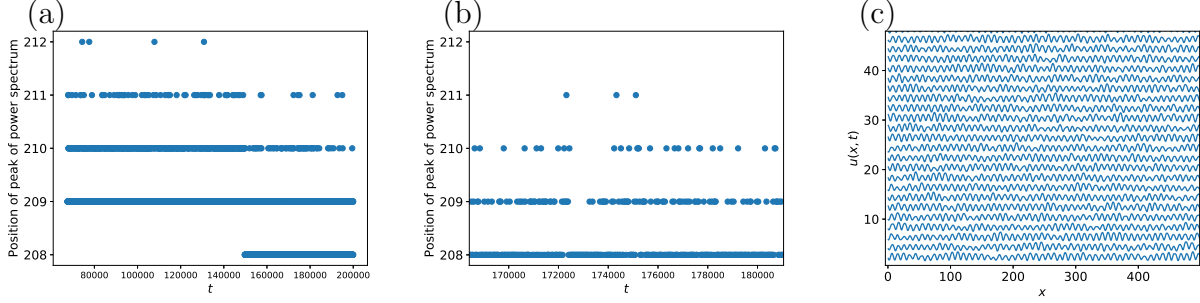Figure 6.2: (a) Maximum of power spectrum as a function of time, with $\alpha = 0.20$ and $\varepsilon = 0.004$. (b) Magnified view of the time interval $168000 \leq t \leq 181000$. (c) Temporal evolution of $u(x,t)$ for $0 \leq x \leq 500$ over the time interval $168000 \leq t \leq 181000$.
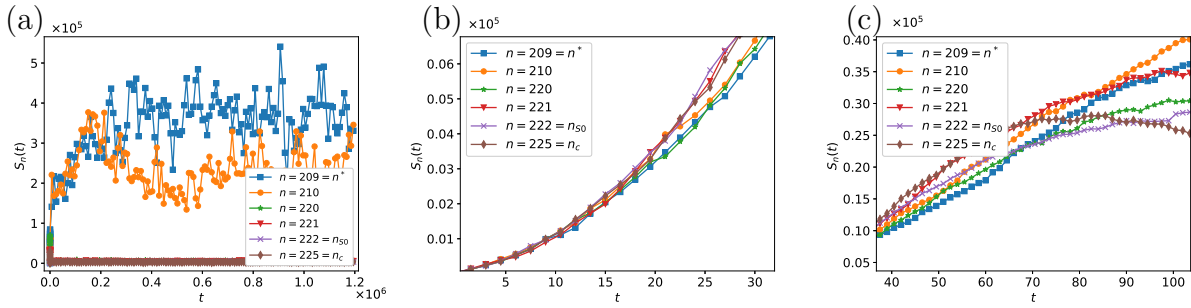

Figure 6.3: (a) S_n as a function of time t when $\varepsilon = 0.004$. (b) Early time dynamics. (c) Intermediate time dynamics.

time for *a single run*. The system initially undergoes transitions between several disordered states at different Eckhaus stable wave numbers. The states at the edges of the Eckhaus band are very unstable. After about 10^5 time steps, the system enters a dynamical regime in which only a few states are visited. This is illustrated in Fig. 6.2 (a) over the time interval $70000 \leq t \leq 205000$. There are rapid transitions among the $n = 209$, 210 and 211 states, along with rare transitions to $n = 212$. After $t \approx 150000$, the $n = 211$ state is visited less frequently, and frequent transitions to $n = 208$ occur. We show an enlarged view of the window between $t = 168000$ and $t = 182000$ in Fig. 6.2 (b). We also show a spatiotemporal portrait of $u(x)$ in Fig. 6.2 (c), although the transitions are hard to see in position space.

We now compute $S_n(t)$ by averaging over 180 integrations of Eq. (6.1). This time, the integration runs from $t = 0$ to $t = T_S = 1.2 \times 10^6$. This is an order of magnitude larger than T_{S0} because the time taken for one dominant mode to emerge from several competing ones is larger when the noise is non-zero, as we will see in Fig. 6.3. We want to determine the state with the maximum value of of the structure function at time T_S, denoted by n_S. The results are shown in Fig. 6.3 (a). We now see that $S_{n^\star}$ and S_{210} attain the largest long-time values while S_{220}, S_{221}, and $S_{n_{S0}}$ decay to small (but non-zero) values. S_{n_c} is always very small.

Fig. 6.3 (b) shows the evolution of $S_n(t)$ at early times. S_{220} and S_{210} are seen to grow fastest even in this early time regime, followed by S_{n_c}. Clearly, our chosen ε is so large that the linear regime is obscured in our simulation. After $t \approx 80$ (Fig. 6.3(c)), the growth of S_{220}, S_{221}, $S_{n_{S0}}$ and S_{n_c} slows down, while $S_{n^\star}$ and S_{210} keep growing. This suggests that the nonlinear terms in Eq. (6.9) for $n = 220$, 221, 222 (n_{S0}) ad $n = n_c$ surpass the linear terms in the presence of the noise. These modes decrease at intermediate times before attaining a small steady state value at $t = T_S$. For wave numbers near $n^\star$, the nonlinear term does not exceed the linear term and the structure function simply saturates at a large value at long times. The $n = 209$ state is the one which maximizes S_n, and hence $n_S = 209$. For this noise strength, n_S is identical to $n^\star$.

To summarize, for an ensemble of noiseless trajectories starting from random configurations, the most probable wave number n_{S0} is very close to n_c. The corresponding component of the structure function grows rapidly in the nonlinear regime, while the component corresponding to $n^\star$ decays in the nonlinear regime. However, when $\varepsilon \geq \varepsilon_{min}$, the situation is reversed and $S_{n^\star}$ grows nonlinearly, while $S_{n_{S0}}$ decays. This is consistent with the findings of Ref. [7], which were obtained from *long-time* averaging of the number of hits in each state. Before attempting to explain this reversal of dynamics, however, we investigate how the structure function dynamics are changed by the magnitude of ε.

6.1.3   Effect of varying the noise strength

In the last chapter, we saw that if $\varepsilon \geq \varepsilon_{min}$, the selected wavenumber from the histogram method, $q^\star$ was independent of the initial conditions as well as the actual value of ε. On the other hand, for $\varepsilon < \varepsilon_{min}$, the selected wavenumber could not be determined from the histogram method. How do the results from the structure function method look as ε is varied? We vary the noise strength over several orders of magnitude and determine n_S at time $T_S = 1.2 \times 10^6$, as shown in Fig. 6.4. We study the following two cases separately: (1) strong noise, i.e. $\varepsilon \geq \varepsilon_{min}$. (2) Weak noise, $\varepsilon < \varepsilon_{min}$. Recall that ε_{min} was determined in Ref. [7] for one run of duration T.

High noise strength

This case is represented by the last three points in Fig. 6.4. As long as $\varepsilon \geq \varepsilon_{min}$, the most probable wave number obtained from the structure function approach, i.e. *n_S is the same as selected wave number $n^\star$ obtained from the histogram method [7].* It is independent of noise strength and initial conditions. In a sense, for all $\varepsilon \geq \varepsilon_{min}$, there is an intrinsic wave number unique to the SKS equation, which can be obtained by time averaging (histogram method) [7] as well as trajectory averaging (structure function method).
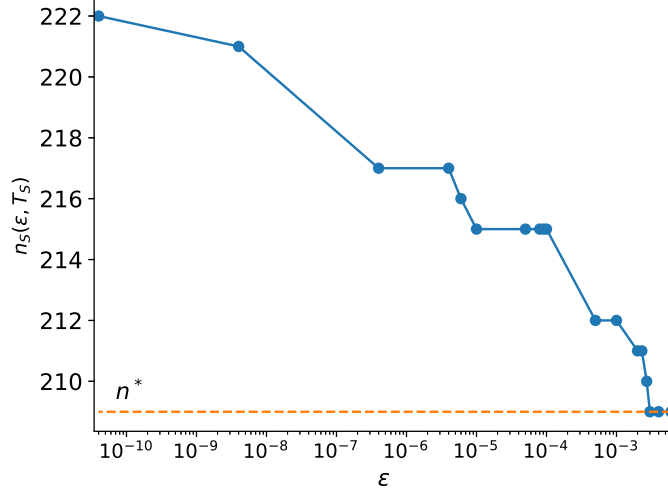
Figure 6.4: $n_S(\varepsilon, T_S)$ obtained from the time evolution of S_n, for different ε. For $\varepsilon \geq \varepsilon_{min}$, n_S is a constant, equal to $n^\star$. For $\varepsilon < \varepsilon_{min}$, a stationary state cannot be reached in time T_S. In this case, n_S depends on ε and T_S.

Low noise strength

Below ε_{min}, n_S increases slowly to values above $n^\star$, as ε is decreased. However, the evolution of $S_n(t)$ is slow in this case and does not reach a steady state in time T_S. To see this, we perform a simulation for ε slightly less than ε_{min} using the *histogram method of Ref. [7]*. We choose $\varepsilon = 0.0027$ for which the structure function approach gives a most probable wave number $n_S = 211$, cf. Fig. 6.4. The histograms at various times are shown in Fig. 6.5. After some initial transients, the system enters the $n = 213$ state, and then transitions to the $n = 212$ state at time $t = 4000$, where it remains stuck for a long time. At $t = 1.6 \times 10^7$ (stars in Fig. 6.5), the system makes frequent jumps to the $n = 210$ and 211 states, but the peak of the histogram stays at $n = 212$. By $t = 3.9 \times 10^7$, the system is in the $n = 210$ state for most of the time, and a prominent peak appears at this wave number (pluses in Fig. 6.5). Just before the end of the integration at $t = T$, the histogram has a peak at $n = n^\star = 209$, but it is still changing with time. It is then reasonable to conclude that the histogram is approaching a stationary form peaked about $n = n^\star$ for $\varepsilon = 0.0027$. Since the structure function approach gives a dominant wave number of $n_S = 211 > n^\star$ for the same ε at $t = T_S$,
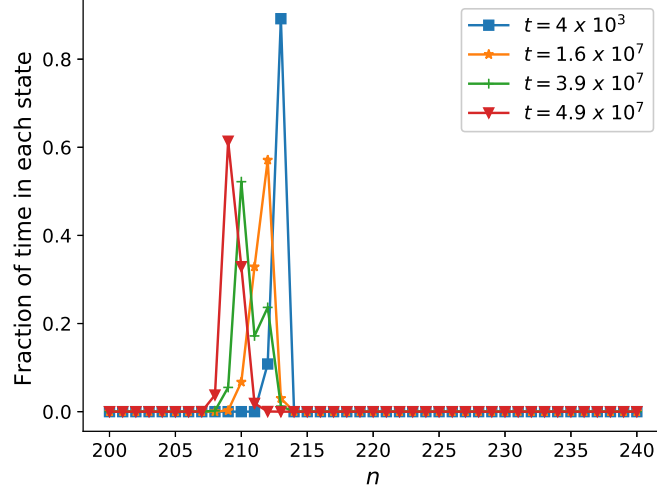
Figure 6.5: Histograms at various times during one long run from $t = 0$ to $t = T$, with $T = 5 \times 10^7$. Here $\varepsilon = 0.0027 < \varepsilon_{min}$.

we infer that it has not yet reached a stationary state at $t = T_S$. *Thus, we can no longer find a unique "selected wave number" which is identical for time averages and trajectory averages.* Instead, the structure function approach yields "most probable" or "dominant" wave number $q_S(\varepsilon, T_S)$ which need not be equal to $q^\star$. The arguments in parentheses emphasize that q_S is a function of ε and T_S when $\varepsilon < \varepsilon_{min}$, and does not represent a characteristic property of the SKS equation. As we decrease ε further, it becomes harder to reach a steady state with either the histogram method or the structure function method. In particular, the results of the histogram method become strongly dependent on initial conditions.

6.1.4 Turning off the noise at intermediate times

We have also investigated what happens if the noise is turned off at some late time. We obtain the time evolution of S_n for $\alpha = 0.20$ with $\varepsilon = 0.004$, but set ε to zero at $t = 10^6$. In Fig. 6.6 (a), we can see that after the noise is turned off, the system settles into one of the deterministic steady states with $n = 208, n^\star$ or 210. The $n = n^\star$ state continues to be more probable than $n = 208$ and 210.

On the other hand, if we use the histogram method, turning off the noise at some time
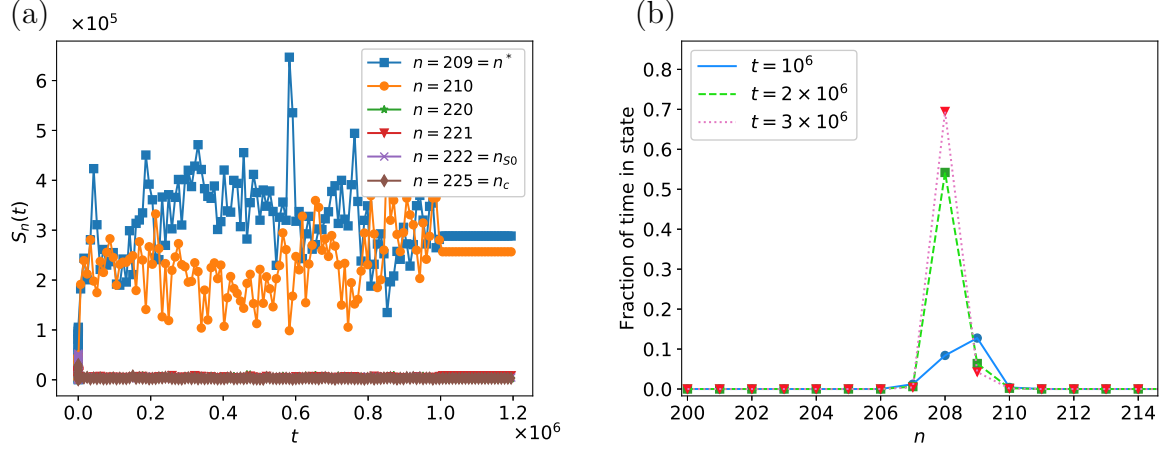
Figure 6.6: (a) $S_n(t)$ when the noise is turned off at $t = 10^6$. (b) Typical histograms at various times for a single run.

will make the system settle in the deterministic state that is closest to its configuration at the instant the noise was turned off. We show this for a typical trajectory (Fig. 6.6 (b)). At $t = 10^6$, when the noise is just turned off, the maximum of the histogram is at $n = n^\star$. However, the configuration at that particular instant is closest to the $n = 208$ state. Hence, as soon as the noise is turned off, the system collapses into the $n = 208$ state. Following this, the histogram develops a peak at $n = 208$ which gets progressively sharper with time. If we were to repeat this simulation again, the system could settle into a different state, depending on the configuration when the noise is turned off.

In summary, we have seen that the noise alters the nonlinear behavior of our model in a non-trivial manner. Its main effect is to make configurations with wave number less than q_c more probable. For $\varepsilon \geq \varepsilon_{min}$, there is a selected wave number which is an intrinsic property of the SKS equation. For $\varepsilon < \varepsilon_{min}$, neither a stationary histogram nor a stationary structure function can be obtained, and one can only find a most probable wave number for a given noise amplitude, time and averaging procedure.

Irrespective of whether ε is greater than or less than ε_{min}, the dominant wave number in Fig. 6.4 is always less than the critical wave number. In the following sections, we will focus on understanding why this is the case.
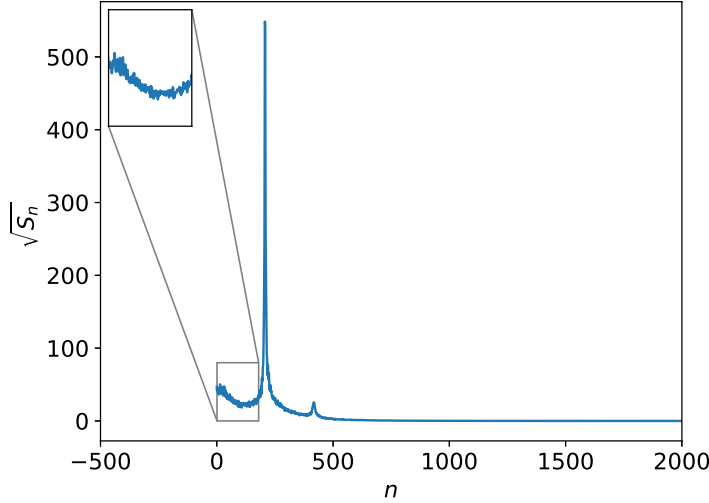
Figure 6.7: Long-time noise-averaged power spectrum for $\alpha = 0.20$ and $\varepsilon = 0.004$. Inset: Amplification of modes near $n = 0$.
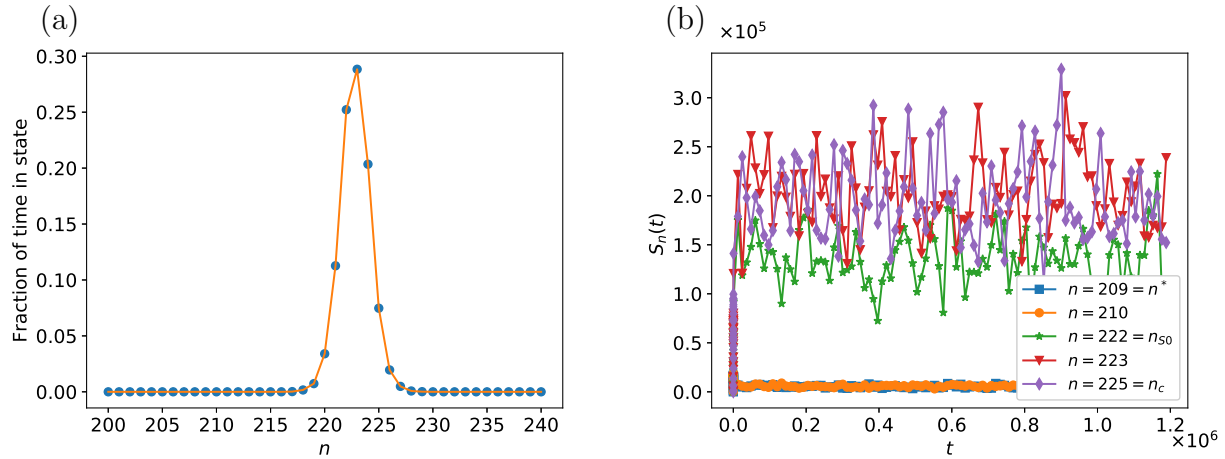
Figure 6.8: (a) Stationary probability distribution of wave numbers for $\alpha = 0.20$ and $\varepsilon = 0.004$ obtained from one long trajectory, but with modes between $n = 1$ and $n = 50$ ignored. The new selected wave number corresponds to $n = 223$ as opposed to $n = 209$ in the original dynamics. (b) Time evolution of S_n. The state with $n = 209$, which was selected in the unmodified dynamics is now highly improbable at long times. The most dominant modes are $n = 222, 223$ and 224. This is clearly evident in spite of the noisiness.

6.2 Mechanism of Wave-number Selection

To understand how the noise shifts the dominant wave number to values less than q_c, it is useful to plot $\sqrt{S_n}$ versus n at $t = T_S$, as shown in Fig. 6.7. We see that $\sqrt{S_n}$ is large for $n_E^- \leq n \leq n_E^+$ as well as for n values lying slightly outside this interval. However, the inset of Fig. 6.7 shows that $\sqrt{S_n}$ is large even for $n \leq 100$, which is far outside the Eckhaus stable band. Moreover, it *increases* as n decreases, becoming comparable to the second harmonic peak. The modes with $n < n_E^-$ quickly decay to zero in purely deterministic evolution (with the exception of $n = 0$, which we disregard) and cannot grow without noise. We hypothesize that this effect is responsible for the observations of the previous section.

To test this hypothesis, we remove the effect of the small wave numbers by repeating the stochastic simulations, but this time setting the modes with n lying between 1 and 50 to zero at each time step. This is equivalent to suppressing wave numbers between 0.003 and 0.157. We retain the $n = 0$ mode because it is a feature of the deterministic problem. We obtain the selected wave number from the histogram method of Ref. [7] and the time evolution of $S_n(t)$ as in Sec. 6.1.

We see immediately that the histogram for the "modified" dynamics is peaked about a *different* selected wave number $q^{\star\prime}$, which is very close to q_c (Fig. 6.8 (a)). On the other hand, the structure function dynamics in Fig. 6.8(b) indicate that the $n = n^\star$ mode decays to zero, while the $n = 222$, 223 and 224 modes grow to large values. The dynamics are extremely noisy in this case, even after averaging over 180 runs, so that it is impossible to determine a single selected wave number from the structure function. In spite of this, it is clear that the suppression of modes near the critical one seen in the original dynamics (Fig. 6.3) is a direct consequence of the large nonlinear excitations at small n. If these excitations are removed, the most probable wave number is much closer to the critical wave number.

In the following subsections, we perform a detailed numerical analysis of the nonlinear terms in Eq. (6.9) for $n \leq n_E^-$ as well as modes close to the critical mode, for $\alpha = 0.20$
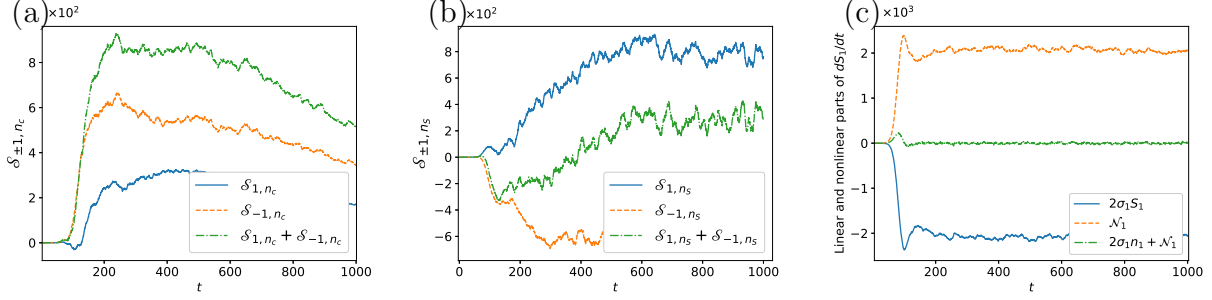
Figure 6.9: (a) Terms in $\mathcal{N}_1$ which contain $\widetilde{u}_{n_c}$ and their sum. (b) Terms in $\mathcal{N}_1$ which contain $\widetilde{u}_{n_S}$ and their sum. (c) Linear and nonlinear parts of Eq. (6.10). The dash-dotted curve is their sum, i.e. the time derivative of S_1.

and $\varepsilon = 0.0001$. We use a small noise strength so that we are able to distinguish between the linear and nonlinear regimes. For this noise strength, the most probable wave number is $n_S(0.0001, T_S) = 215$. We will show that the critical mode initially drives the nonlinear growth of the small n modes. When the small n modes become large, they cause the decay of the modes near n_c. We will then consider the effect of the small n modes on the $n = n_S$ mode and show that the small n modes drive the *growth* of this mode (or the $n^\star$ mode when $\varepsilon \geq \varepsilon_{min}$).

6.2.1 Nonlinear growth of long wavelength modes and consequences for Eckhaus modes

We write Eq. (6.9) for small n, disregarding terms like $\langle \widetilde{u}_n \widetilde{\zeta}_{-n} \rangle$ and $\langle \widetilde{u}_{-n} \widetilde{\zeta}_n \rangle$. For concreteness, we focus on the case $n = 1$. The analysis is similar for all modes with $n \leq n_E^-$.

$$\dot{S}_1(t) = 2\sigma_1 S_1(t) + \sum_{n_1=1}^{N/2-1} \left(\mathcal{S}_{1,n_1} + \mathcal{S}_{-1,n_1} \right) = 2\sigma_1 S_1(t) + \mathcal{N}_1 \tag{6.10}$$

We know from Sec. 6.1 that the effect of the noise is significant only in the nonlinear

regime. The nonlinear term in Eq. (6.10) is

$$\mathcal{N}_1 = \sum_{n_1=1}^{N/2-1} \left(\mathcal{S}_{1,n_1} + \mathcal{S}_{-1,n_1} \right)$$

$$= \mathcal{S}_{1,1} + \mathcal{S}_{-1,1} + \mathcal{S}_{1,2} + \mathcal{S}_{-1,2} + \cdots +$$

$$\underbrace{\mathcal{S}_{1,n_E^-} + \mathcal{S}_{-1,n_E^-} + \cdots + \mathcal{S}_{1,n_E^+} + \mathcal{S}_{-1,n_E^+}}_{\text{Eckhaus stable modes}} + \cdots \quad (6.11)$$

We expect that the largest terms in Eq. (6.11) are the ones with $n_E^- \leq n_1 \leq n_E^+$. These terms represent the interactions between the $n = 1$ mode and the Eckhaus stable modes. Out of these terms, the terms with n_1 close to n_c have the largest magnitude at the start of the nonlinear regime. From the definition of $\mathcal{S}_{\pm n, n_1}$, we see that the $n = 1$ mode is coupled to the $n = n_c$ mode when $n_1 = n_c - 1, n_c$ or $n_c + 1$. These terms evaluate to

$$\mathcal{S}_{1,n_c} + \mathcal{S}_{-1,n_c} + \mathcal{S}_{1,n_c-1} + \mathcal{S}_{-1,n_c+1} \quad (6.12)$$

We further note that $\mathcal{S}_{1,n_c} = \mathcal{S}_{-1,n_c+1}$ and $\mathcal{S}_{-1,n_c} = \mathcal{S}_{1,n_c-1}$. Hence, the nonlinear terms coupling $n = 1$ with $n = n_c$ are

$$2\left(\mathcal{S}_{1,n_c} + \mathcal{S}_{-1,n_c} \right) = 4 \left(2\pi/L \right)^2 \left[n_c(n_c + 1) Re\langle \widetilde{u}_{n_c} \widetilde{u}_{-n_c-1} \widetilde{u}_1 \rangle \right.$$

$$\left. + n_c(n_c - 1) Re\langle \widetilde{u}_{n_c} \widetilde{u}_{-n_c+1} \widetilde{u}_{-1} \rangle \right] \quad (6.13)$$

where we have used Eq. (5.17) for the nth component of the DFT of the spatial derivative $\partial_x u$. These terms represent the net effect of the critical mode on the time evolution of S_1.

At the same time, the $n = 1$ mode contributes to the equation of motion of S_{n_c}, which is the component of the structure function corresponding to the critical mode. The equation

of motion for S_{n_c} is

$$\dot{S}_{n_c}(t) = 2\sigma_{n_c} S_{n_c}(t) + \mathcal{N}_{n_c} \tag{6.14}$$

As before, we can write the nonlinear term $\mathcal{N}_{n_c}$ as

$$\mathcal{N}_{n_c} = \sum_{n_1=1}^{N/2-1} (S_{n_c,n_1} + S_{-n_c,n_1})$$

$$= \underbrace{S_{n_c,1} + S_{-n_c,1} + S_{n_c,2} + S_{-n_c,2}}_{\text{long wavelength modes}} + \cdots +$$

$$S_{n_c,n_E^-} + S_{-n_c,n_E^-} + \cdots + S_{n_c,n_E^+} + S_{-n_c,n_E^+} + \cdots \tag{6.15}$$

The terms in Eq. (6.15) depending on $\tilde{u}_1$ are

$$S_{n_c,1} + S_{-n_c,1} + S_{-n_c,n_c-1} + S_{-n_c,n_c+1} \tag{6.16}$$

Again, from the definition of $S_{\pm n,n_1}$, it follows that $S_{n_c,1} = S_{-n_c,n_c+1}$ and $S_{-n_c,1} = S_{-n_c,n_c-1}$. The nonlinear terms of Eq. (6.16) then add up to

$$2\left(S_{n_c,1} + S_{-n_c,1}\right) = 4\left(2\pi/L\right)^2$$

$$[(n_c + 1) \times Re\langle \tilde{u}_1 \tilde{u}_{-n_c-1} \tilde{u}_{n_c} \rangle \tag{6.17}$$

$$- (n_c - 1) \times Re\langle \tilde{u}_{n_c-1} \tilde{u}_1 \tilde{u}_{-n_c} \rangle]$$

Comparing Eq. (6.13) and Eq. (6.17), we see that S_{1,n_c} and $S_{n_c,1}$ are both proportional to $Re\langle \tilde{u}_1 \tilde{u}_{-n_c-1} \tilde{u}_{n_c} \rangle$, and have the same sign. Similarly, S_{-1,n_c} and $S_{-n_c,1}$ are both proportional to $Re\langle \tilde{u}_{n_c} \tilde{u}_{-n_c+1} \tilde{u}_{-1} \rangle$, *but have opposite signs*. We numerically evaluate each of these
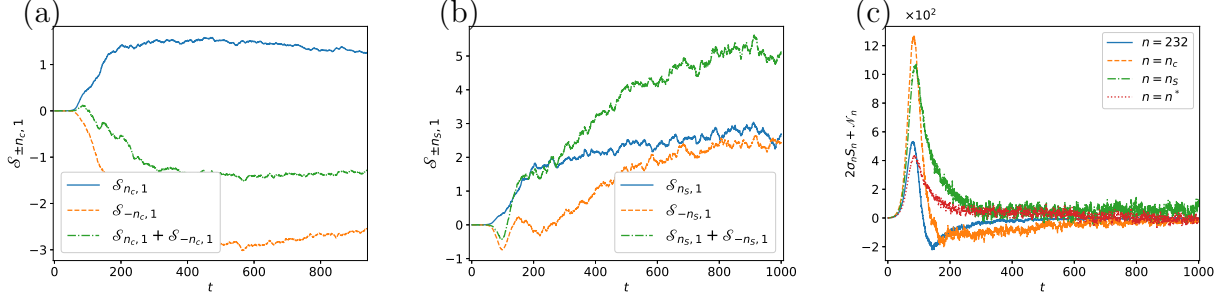
Figure 6.10: (a) $S_{n_c,1}$ and $S_{-n_c,1}$ as a function of time. Their sum represents the total contribution of $\widetilde{u}_1$ to $\dot{S}_{n_c}$ and is negative after $t \approx 180$. (b) $S_{n_S,1}$ and $S_{-n_S,1}$ as a function of time. Their sum represents the total contribution of $\widetilde{u}_1$ to $\dot{S}_{n_S}$ and is always positive . (c) $\dot{S}_n = 2\sigma_n S_n + \mathcal{N}_n$ as a function of time for various values of n. It is negative for $n = n_c$ and $n = 232$ after a particular time, but positive for n_S and $n^\star$.

quantities for $\alpha = 0.20$ and $\varepsilon = 0.0001 < \varepsilon_{min}$.

First, we plot S_{1,n_c} and S_{-1,n_c}, as well as their sum as a function of time in Fig. 6.9(a). After about $t = 80$, both S_{1,n_c} and S_{-1,n_c} (and hence their sum) are positive. Thus, the net contribution of the critical mode to the equation of motion of S_1 is positive.

A short time later, Eckhaus modes further from n_c become important and other terms in Eq. (6.11) become large. As an example, we show the effect of the $n = n_S$ mode on the time evolution of S_1 in Fig. 6.9 (b). We see that S_{1,n_S} is positive, but S_{-1,n_S} is negative. However, their sum is almost always positive, although it is smaller than the corresponding contribution from the critical mode.

Having studied some of the typical terms arising in Eq. (6.11), we plot the full nonlinear term $\mathcal{N}_1$ and the linear term i.e. $2\sigma_1 S_1$ in Fig. 6.9 (c). In the same plot, we show the total time derivative of S_1 which is simply the sum $2\sigma_1 S_1 + \mathcal{N}_1$. The linear term, $2\sigma_1 S_1$ is always negative because the growth rate σ_1 is negative and S_1 is positive by definition. The total nonlinear term $\mathcal{N}_1$ is always positive. Most importantly, starting at $t \approx 80$, the magnitude of the nonlinear term becomes slightly greater than the linear one, and the sum of the two is positive (green dash-dotted line). Note that this is around the same time that the nonlinear terms in dS_1/dt arising from the critical mode become non-zero. This shows that the interaction between the $n = 1$ mode and the critical mode is responsible for the

82

initial increase in S_1. Later, other Eckhaus modes become active and sustain the growth of S_1 until $t \approx 100$. Shortly after, the linear and nonlinear parts balance each other and S_1 reaches a steady non-zero value.

Let us now return to Eq. (6.17). We plot each of the terms $\mathcal{S}_{n_c,1}$ and $\mathcal{S}_{-n_c,1}$, along with their sum in Fig. 6.10 (a). We expect $\mathcal{S}_{n_c,1}$ to be positive and $\mathcal{S}_{-n_c,1}$ to be negative, as discussed above. This is indeed what we observe. The sum of the two is *negative*, and we conclude that the total contribution of the $n = 1$ mode to the time derivative of S_{n_c} is ngative. Figs. 6.9 (a) and Fig. 6.10 (a), and the discussion above have an important implication: *The nonlinear couplings between the $n = 1$ and $n = n_c$ modes assist the growth of S_1, but oppose the growth of S_{n_c}.*

The next piece of the puzzle is to understand why the $n = n_S$ mode persists, even though the critical mode and modes close to it decay. In analogy with Eq. (6.17), the net effect of the $n = 1$ mode on the evolution of the $n = n_S$ mode is

$$
\begin{aligned}
2\left(\mathcal{S}_{n_S,1} + \mathcal{S}_{-n_S,1}\right) = 4\left(\frac{2\pi}{L}\right)^2 &\left[(n_S + 1) \times Re\langle \widetilde{u}_1 \widetilde{u}_{-n_S-1} \widetilde{u}_{n_S}\rangle \right. \\
&\left. -(n_S - 1) \times Re\langle \widetilde{u}_1 \widetilde{u}_{n_S-1} \widetilde{u}_{-n_S}\rangle\right]
\end{aligned}
\tag{6.18}
$$

The time evolution of $\mathcal{S}_{n_S,1}$ and $\mathcal{S}_{-n_S,1}$ along with their sum is shown in Fig. 6.10 (b). This time, $\mathcal{S}_{-n_S,1}$ becomes positive after $t \approx 230$, and the sum $\mathcal{S}_{n_S,1} + \mathcal{S}_{-n_S,1}$ is positive. Thus, the nonlinear interactions between the $n = 1$ and $n = n_S$ contribute positive terms to the time derivative of S_{n_S} and hence assist the growth of the $n = n_S$ mode.

We now evaluate and plot the full right hand side of Eq. (6.3) for different values of n in the Eckhaus band. In general, we see that the time derivative of the structure function becomes more and more negative as n is increased beyond n_c. We illustrate this for $n = 232$ (solid blue line) in Fig. 6.10 (c). For $n = n_c$, the total time derivative $\frac{dS_{n_c}}{dt}$ dips slightly below zero around $t \approx 200$, and remains negative. Note that this occurs at about the same time that the contribution of the $n = 1$ mode to dS_{n_c}/dt becomes negative (see the green
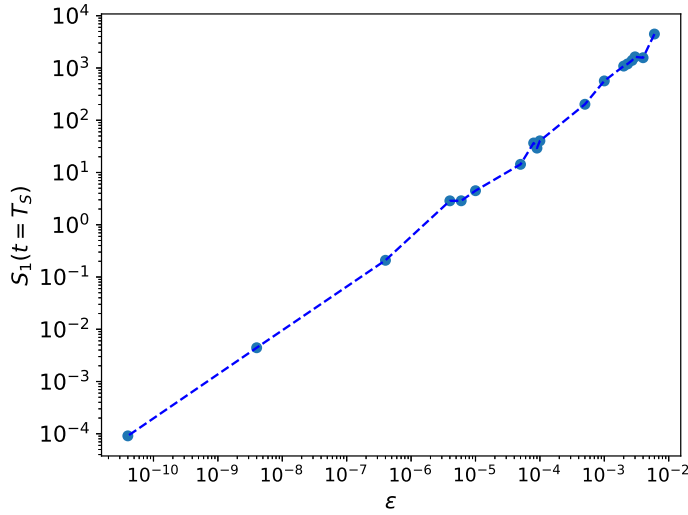
Figure 6.11: $S_1(t = T_S)$ for different noise strengths, and $\alpha = 0.20$.

curve in Fig. 6.10 (a)). This suggests that the growth of the small n modes in the nonlinear regime is directly responsible for the damping of the critical mode.

On the other hand, the time derivative of S_{n_S} stays non-negative throughout. We also show the time derivative of $S_{n^\star}$ (dash-dotted line). $dS_{n^\star}/dt$ is non-negative for almost all t, but its magnitude is less than that of dS_{n_S}/dt, which explains why $n_S = 215 \neq n^\star$ for $\varepsilon = 0.0001$.

6.2.2 Significance of noise strength and control parameter in exciting small wave number modes

The extent to which the modes with $n < n_E^-$ are excited by the noise depends on ε. To understand this dependence, we again focus on S_1. We compute $S_1(t = T_S)$ for a wide range of ε and plot it in Fig. 6.11. The value of $S_1(t = T_S)$ increases as ε is increased. The increasing strength of the $n < n_E^-$ modes as ε increases drives $n_S(\varepsilon, T_S)$ closer and closer to $n^\star$, with n_S becoming *equal to* $n^\star$ when $\varepsilon \geq \varepsilon_{min}$. It would be interesting to examine the dependence of all small n modes on the noise strength, as well as on the value of α. This is beyond the scope of the present paper and is saved for future work.
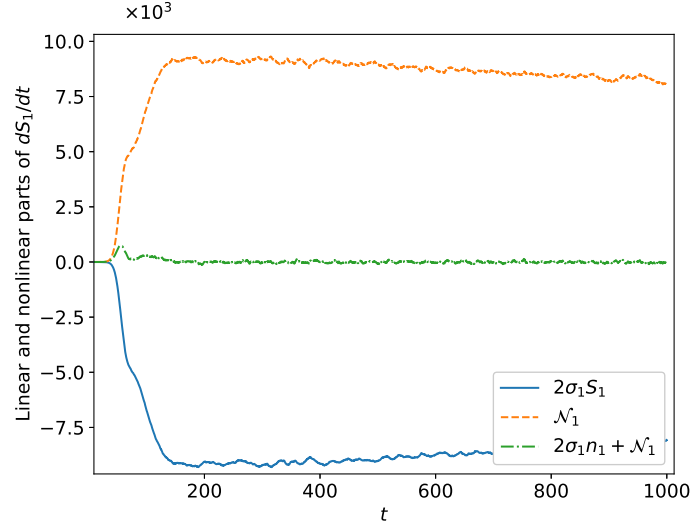
Figure 6.12: Linear and nonlinear terms in $\frac{d}{dt}S_1$ and their sum for $\alpha = 0.17$ and $\varepsilon = 0.0001$.

We can also provide a qualitative explanation for why the selected wave number decreases as we decrease α. We know that the width of the Eckhaus band increases as α decreases. Hence, the evolution equation for S_1 contains more terms which mix $\widetilde{u}_1$ with Eckhaus stable modes. Although we are unable to give a rigorous mathematical proof, our simulations show that the larger number of mixing terms causes a larger excitation of the $(n < n_E^-)$ modes.

We repeat the above simulations for $\alpha = 0.17$ and the same noise strength ($\varepsilon = 0.0001$). We show the linear and nonlinear terms in $\dot{S}_1$, as well as their sum in Fig. 6.12. The linear term is negative while the nonlinear term is positive, like in Fig. 6.9 (a). The sum of the linear and nonlinear terms is positive at short times. *Comparing the scale of the vertical axis in Fig. 6.9 (c) with that of Fig. 6.12 shows that $\dot{S}_1$ (and hence S_1) is larger for $\alpha = 0.17$ than for $\alpha = 0.20$, for the same noise strength.* This in turn, ensures that modes near the critical mode are damped to a larger extent as α is decreased below α_c. As a result, n_S decreases below n_c as α is decreased below α_c, for fixed noise strength.

6.3 Conclusions

In summary, we have analyzed the dynamics of the noisy SKS equation to shed light on the process of wavenumber selection and highlighted the important role of long wavelength fluctuations. Although the analysis is only valid for the specific case of the SKS model, it illustrates that noise can have non-trivial interactions with nonlinearities and significantly influence the macroscopic dynamics.

Chapter 7

Conclusions

In conclusion, we have performed a detailed numerical study of noise induced wavenumber selection in the one dimensional SKS equation. We have shown that even in the presence of large noise, long time power spectra of the field are most likely to be peaked at a unique wavenumber that does not depend on the initial state or the noise strength. We note again that due to the large noise strengths we had to use, there were non-zero Fourier components at other wavenumbers, which means that for finite system sizes and large noise strengths, there is no true selection, as expected. However, since the position of the peak of the power spectrum is independent of noise strength and since the probability distributions become sharper with increasing system size and decreasing noise strength, it is plausible to conclude that the same wavenumber would be selected for noise strengths much less than the ones used here, except that it would require prohibitively large integration times.

It is interesting to compare our findings with other selection mechanisms proposed in [3, 4, 16]. As discussed there, control parameter ramps are an efficient way to select a unique, well defined wavenumber. However, Refs. [4, 16] also show that varying different quantities that lead to the same final control parameter results in different selected wavenumbers. Ref. [57] has shown that starting from random initial conditions and simulating deterministically, the final wavenumber depends on the initial state. In contrast, our work shows that at long

times, the system is most likely to be found in a state with a dominant wavenumber, and this dominant wavenumber does not depend on initial conditions or noise strength, but is an intrinsic property of the SKS system. We have been able to show this for a wide range of control parameters and large system sizes, in contrast to previous work. Our work shows that noise induced wavenumber selection can occur in non-potential systems. Much remains to be done however; a future direction could be to devise efficient importance sampling techniques which would enable us to study transitions between states without using large noise strengths. It would also be interesting to see if it is possible to predict the selected wavenumber analytically, although to our knowledge no such analytical theory exists.

In the second part of this work, we have identified the mechanism of noise-induced wavenumber selection in a simple model of pattern formation. We have shown that the noise inhibits the nonlinear growth of modes near the critical mode, and enhances the growth of modes smaller than the critical wave number. The amplification of very long wavelength perturbations is responsible for the above effects. We have shown that if long wavelength excitations are suppressed, the selected wave numbers are close to the critical wave number. Together, these findings indicate that the coupling between modes with small wave numbers and the Eckhaus stable modes is the most important factor in determining the selected state.

It is important to address some shortcomings of our numerics. First, we are unable to draw definitive conclusions about selection in the weak noise regime for reasons explained in Sec. 6.1. This is purely due to finite computational resources. If we somehow increase T, it is possible that a stationary histogram peaked at $n^\star$ could be attained for very small values of ε. Alternatively, it is possible that the dominant wave number determined from the structure function i.e. n_S approaches $n^\star$ for small ε as $T_S \to \infty$. With our current resources and algorithms, it is not possible to confirm these hypotheses numerically and we have to restrict our attention exclusively to the strong noise regime.

Secondly, the evolution of the structure function is very noisy, in spite of averaging over 180 independent trajectories. On the other hand, the histograms of Ref. [7] are quite smooth.

This is because the histograms were obtained by determining the state of the system at each time step over one trajectory of length $\sim 10^8 \Delta t$, which is equivalent to taking 10^8 independent measurements of the state of the system. In contrast, for the structure function approach, one needs to find the *ensemble* average of the quantity $|\widetilde{u}_n(t)|^2$, which fluctuates rapidly from one time step to the next. In addition, computational restrictions prevent us from running more than 180 independent trajectories. Thus, the temporal averaging over a long run leads to very smooth statistics, while averaging over trajectories does not. However, in spite of the noisiness, one can obtain new insights into the mechanism of wave-number selection from the structure function dynamics that cannot be gained solely from the stationary histograms of our previous work.

Finally, it is worth mentioning that the large noise-induced nonlinear excitations at small wave numbers seen here may be related to the existence of chaotic solutions as $\alpha \to 0$. These chaotic solutions are a distinctive feature of the SKS equation and more studies of the stochastic SKS equation are needed in the $\alpha < 0.16$ regime. It would be interesting to investigate noise-driven selection in other non-potential models which do not possess chaotic solutions.

Another promising direction is to explore stochastic dynamics in higher dimensions and in the more realistic situations described in the Introduction. We also anticipate that the large noise strengths used here, which may be unphysical for some systems, will be relevant to biological processes, where the noise is known to be large [65].

Appendices

Appendix A

Supplementary Information for Chapters 6 and 7

A.1 Solving partial differential equations in Fourier space

We derive the appropriate discrete Fourier transforms of the various derivatives of the field $u(x, t)$ needed for the SKS problem. We closely follow the treatment given in Ref. [66]. The field $u(x, t)$ is defined for $0 \leq x \leq L$ with periodic boundary conditions $u(x + L, t) = u(x, t)$ so that

$$u(x, t) = \sum_{n=-\infty}^{\infty} \widetilde{u}_n(t) e^{\frac{2\pi i n x}{L}} \tag{A.1}$$

with the Fourier coefficients given by

$$\widetilde{u}_n(t) = \frac{1}{L} \int_0^L e^{-\frac{2\pi i n x}{L}} u(x, t) dx \tag{A.2}$$

Now, we approximate $u(x, t)$ by N discrete samples $u_m(t) = u(mL/N, t)$ for $m = 0, 1, \cdots, N-1$ and the $\widetilde{u}_n(t)$ are approximated using the discrete Fourier transform (DFT), defined as

$$\widetilde{u}_n(t) = \sum_{m=0}^{N-1} u_m(t) e^{-\frac{2\pi i n m}{N}} \tag{A.3}$$

The values of $u_m(t)$ can be obtained from the inverse discrete Fourier transform (IDFT),

$$u_m(t) = \frac{1}{N} \sum_{n=0}^{N-1} \widetilde{u}_n(t) e^{\frac{2\pi i n m}{N}} \tag{A.4}$$

(The placement of the pre-factor $1/N$ is a matter of convention and we have chosen the convention consistent with NumPy's implementation of the DFT). The $\widetilde{u}_n$'s can be obtained from the u_m's and vice versa in $\mathcal{O}(N\ln N)$ operations using the Fast Fourier transform (FFT). In what follows, we will not explicitly indicate the dependence on t for convenience. It should be understood that the u_m's and $\widetilde{u}_n$'s are functions of time.

To compute derivatives such as $u'(x)$, we need more than just the discrete samples u_m. We need to obtain a continuous interpolation *between* sample points and *differentiate this interpolation*. We use a technique called trigonometric interpolation. First, we note that replacing n in Eq. (A.14) by $n + lN$, where l is an integer, leaves the sample values u_m unchanged. However, it changes the values of the derivatives of u between the sample points, because it causes $u(x)$ to oscillate between sample points. This is called *aliasing*. To resolve this ambiguity, we assume a more general interpolation obtained by substituting $m = Nx/L$ into Eq. (A.14) and allowing an arbitrary aliasing integer l_n for each $\widetilde{u}_n$

$$u(x) = \frac{1}{N} \sum_{n=0}^{N-1} \widetilde{u}_n e^{\frac{2\pi i}{L}(n+l_n N)x} \tag{A.5}$$

where the l_n's are integers. We now impose the condition that the interpolating function undergoes "minimal oscillation" between sample points. This is equivalent to minimizing the spatial average of the squared slope $\frac{1}{L}\int_0^L |u'(x)|^2 dx$. Substituting Eq. (A.5) into this expression and simplifying gives

$$\frac{1}{L} \int_0^L |u'(x)|^2 dx = \left(\frac{2\pi}{LN}\right)^2 \sum_{n=0}^{N-1} |\widetilde{u}_n|^2 (n+l_n N)^2 \tag{A.6}$$

We see that the average squared slope is minimized by those l_n's that minimize $(n+l_n N)^2$

for each n. For $0 \leq n < N/2$, this quantity is minimum for all $l_n = 0$. For $N/2 < n < N$, the quantity is minimized by setting all the l_n's to -1. The situation is more complicated when N is even and $n = N/2$ because now the quantity $(n + l_n N)^2$ can be minimized by either $l_{N/2} = 0$ or $l_{N/2} = -1$. To overcome this issue, we split the $n = N/2$ term between the cases $l_n = 0$ and $l_n = -1$ in the form $\widetilde{u}_{N/2} \left[v e^{i\pi N x/L} + (1-v) e^{-i\pi N x/L} \right]$. The contribution of this term to the mean squared slope is

$$\frac{1}{N^2} \left(\frac{\pi N}{L} \right)^2 |\widetilde{u}_{N/2}|^2 \left[v^2 + (1-v)^2 \right] \tag{A.7}$$

which is minimized by $v = 1/2$. The minimum oscillation interpolation of $u(x)$ is then

$$N u(x) = \widetilde{u}_0 + \sum_{0 < n < N/2} \widetilde{u}_n e^{2\pi i n x/L} + \sum_{N/2+1 < n < N} \widetilde{u}_n e^{2\pi i (n-N) x/L} + \widetilde{u}_{N/2} \cos(\pi N x/L) \tag{A.8}$$

From this expression, the spatial derivatives can be calculated easily. For example, differentiating Eq. (A.8) gives,

$$N u'(x) = \sum_{0 < n < N/2} \frac{2\pi i n}{L} \widetilde{u}_n e^{+\frac{2\pi i n x}{L}} + \sum_{N/2+1 < n < N} \frac{2\pi i (n-N)}{L} \widetilde{u}_n e^{\frac{2\pi i (n-N) x}{L}} - \frac{\pi N}{L} \widetilde{u}_{N/2} \sin\left(\frac{\pi N x}{L} \right) \tag{A.9}$$

Evaluating at the sample points $x = mL/N$, we get,

$$N u'_m = \sum_{0 < n < N/2} \frac{2\pi i n}{L} \widetilde{u}_n e^{+\frac{2\pi i n m}{N}} + \sum_{N/2+1 < n < N} \frac{2\pi i (n-N)}{L} \widetilde{u}_n e^{\frac{2\pi i (n-N) m}{N}} \tag{A.10}$$

since the derivative of the $N/2$ term vanishes at the sample points. Noting that $e^{\frac{2\pi i (n-N) m}{N}} = e^{\frac{2\pi n m}{N}}$, we get

$$N u'_m = \sum_{0 < n < N/2} \frac{2\pi i n}{L} \widetilde{u}_n e^{+\frac{2\pi i n m}{N}} + \sum_{N/2+1 < n < N} \frac{2\pi i (n-N)}{L} \widetilde{u}_n e^{\frac{2\pi i n m}{N}} \tag{A.11}$$

We set $u'_m = v_m$ and let the DFT of u'_m be denoted by $\widetilde{v}_n$. Then, comparing with the

definition of the IDFT, Eq. (A.14), it is seen that

$$
\begin{aligned}
\widetilde{v}_n &= \frac{2\pi i n}{L}\widetilde{u}_n \text{ if } 0 < n < N/2 \\
&= \frac{2\pi i (n-N)}{L}\widetilde{u}_n \text{ if } N/2 + 1 < n < N \\
&= 0 \text{ if } n = 0 \text{ or } n = N/2
\end{aligned}
\tag{A.12}
$$

This can be written compactly as

$$
\widetilde{v}_n = \frac{2\pi i n}{L}\widetilde{u}_n; \quad n = 1, \cdots, N/2 - 1, -N/2 + 1, \cdots, -1
\tag{A.13}
$$

with $\widetilde{v}_0$ and $\widetilde{v}_{N/2}$ equal to zero as before. To maintain consistency, it is also customary to write Eq. (A.14) as

$$
u_m(t) = \frac{1}{N} \sum_{n=-N/2}^{N/2-1} \widetilde{u}_n(t) e^{\frac{2\pi i n m}{N}}
\tag{A.14}
$$

Similarly, the second and fourth spatial derivatives are

$$
u_m'' = - \sum_{n=-N/2}^{N/2-1} \left(\frac{2\pi n}{L}\right)^2 \widetilde{u}_n e^{\frac{2\pi i m n}{N}}
\tag{A.15}
$$

and

$$
u_m'''' = \sum_{n=-N/2}^{N/2-1} \left(\frac{2\pi n}{L}\right)^4 \widetilde{u}_n e^{\frac{2\pi i m n}{N}}
\tag{A.16}
$$

We can now derive the DFT of the nonlinear term in the SKS equation i.e. $(\partial_x u)^2 = v_m^2$. From the definition of the DFT we have

$$
\begin{aligned}
\widetilde{\mathbf{N}}_n &= \sum_{m=0}^{N-1} (\partial_x u)_m^2 e^{-2\pi i m n / N} \\
&= \sum_{m=0}^{N-1} v_m^2 e^{-2\pi i m n / N}
\end{aligned}
\tag{A.17}
$$

Using the fact that $v_m = \frac{1}{N}\sum_{n=-N/2}^{N/2-1} \widetilde{v}_n e^{\frac{2\pi i n m}{N}}$, we get

94

$$\widetilde{\hat{\mathbf{N}}}_n = \frac{1}{N^2} \sum_{m=0}^{N-1} exp\left[-2\pi inm/N\right]$$

$$\times \sum_{n_1=-N/2}^{N/2-1} \widetilde{v}_{n_1} exp\left[2\pi in_1m/N\right] \tag{A.18}$$

$$\times \sum_{n_2=-N/2}^{N/2-1} \widetilde{v}_{n_2} exp\left[2\pi in_2m/N\right]$$

Performing the sum over m yields $N\delta_{n_1+n_2-n}$. The end result is

$$\widetilde{\hat{\mathbf{N}}}_n = \frac{1}{N} \sum_{n_1=-N/2}^{N/2-1} \widetilde{v}_{n_1}\widetilde{v}_{n-n_1} \tag{A.19}$$

A.2 Determining the appropriate range of α

As mentioned in Chapter 3, a variety of complicated configurations become possible when the second harmonic becomes linearly unstable along with the fundamental harmonic [2]. To determine the value of α when this occurs, we set the growth rates for a perturbation with wave number q and a perturbation with wave number $2q$ to zero for $\alpha = \alpha_2$.

$$\sigma(q) = -\alpha_2 + q^2 - q^4 = 0 \tag{A.20}$$

and

$$\sigma(2q) = -\alpha_2 + 4q^2 - 16q^4 = 0 \tag{A.21}$$

Solving these equations simultaneously gives $\alpha_2 = 4/25 = 0.16$ and $q = 1/\sqrt{5}$. Accordingly, we restrict our study to $0.16 < \alpha < 0.25$.
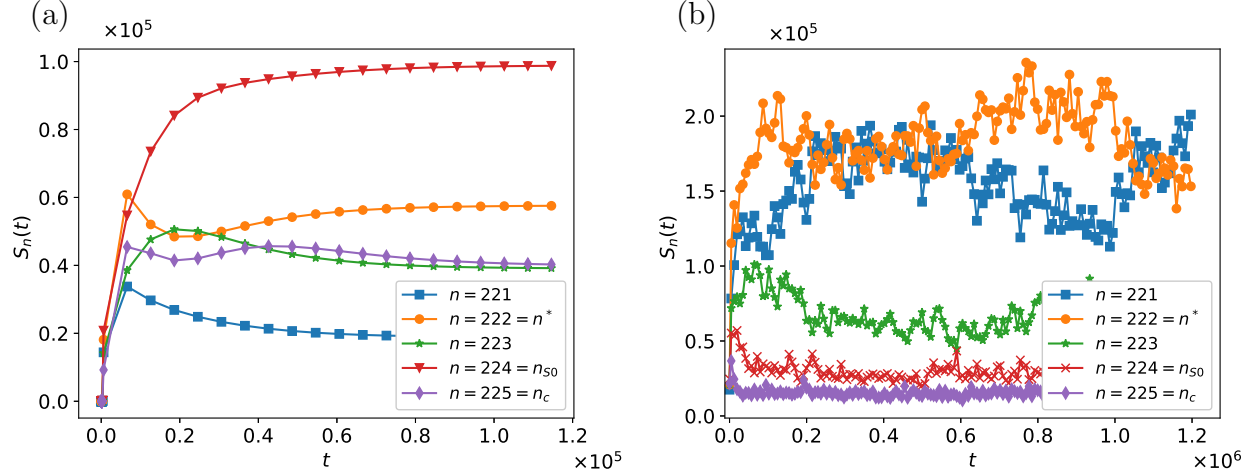
Figure A.1: S_n as a function of time for $\alpha = 0.24$. (a) $\varepsilon = 0.0$. (b) $\varepsilon = 0.0005$.

A.3   Results from Chapter 6 for other values of α

Here we show our results for other values of the control parameter α. ε is greater than ε_{min} in all cases and hence $n_S = n^\star$. In Figs. A.1, A.2, and A.3, we show the time evolution of $S_n(t)$ with and without noise for $\alpha = 0.24,\ 0.22$, and 0.17. For $\alpha = 0.24$ (Fig. A.1), $n_{S0} = 224$ and $n^\star = 222$. For $\alpha = 0.22$ (Fig. A.2), $n_{S0} = 222$ and $n^\star = 215$. Similar results are seen for $\alpha = 0.17$ (Fig. A.3).

In Fig. A.4, we show $n_S(\varepsilon, T_S)$ as a function of ε for $\alpha = 0.24,\ 0.22$ and 0.17.

Next we show the square root of the stationary structure function S_n versus n for the above values of α (Fig. A.5). As shown in Chapter 6, there is a large amplification of modes near $n \approx 0$. The amplification is larger for smaller values of α.

Finally, we show how the stationary histograms and time evolution plots are modified when the modes between $n = 1$ and $n = 50$ are suppressed; see Figs. A.6, A.7 and A.8.

A.4   More results from Section 6.2

The nonlinear growth of other small wave number modes can be explained using a similar argument. For example, we also computed the time derivatives of S_{25} and S_{50}. These are also positive initially, and approach zero at late times, leading to a non-zero value of S_{25} and
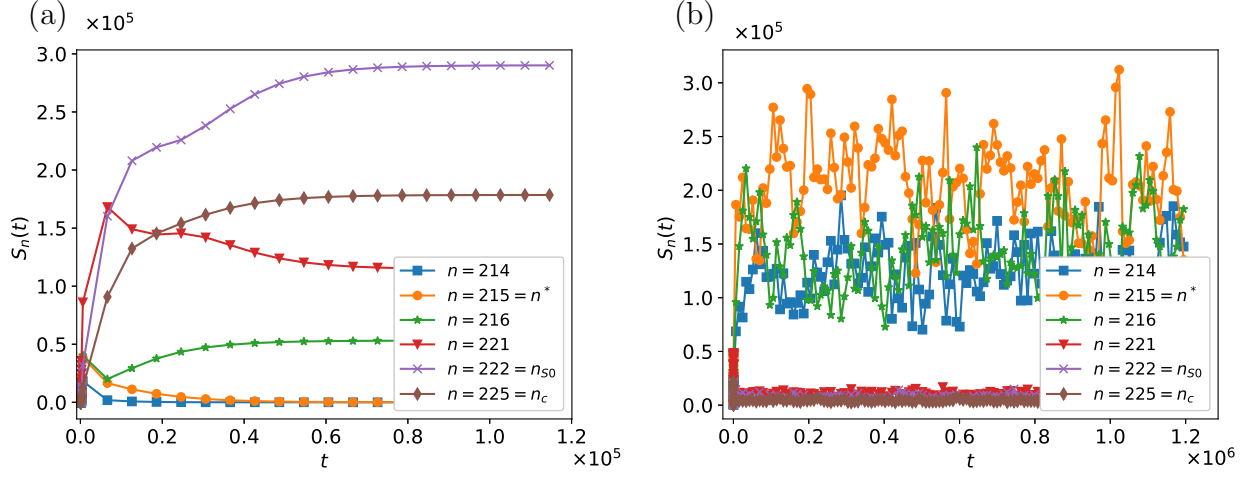
Figure A.2: S_n as a function of time for $\alpha = 0.22$. (a) $\varepsilon = 0.0$. (b) $\varepsilon = 0.0025$.
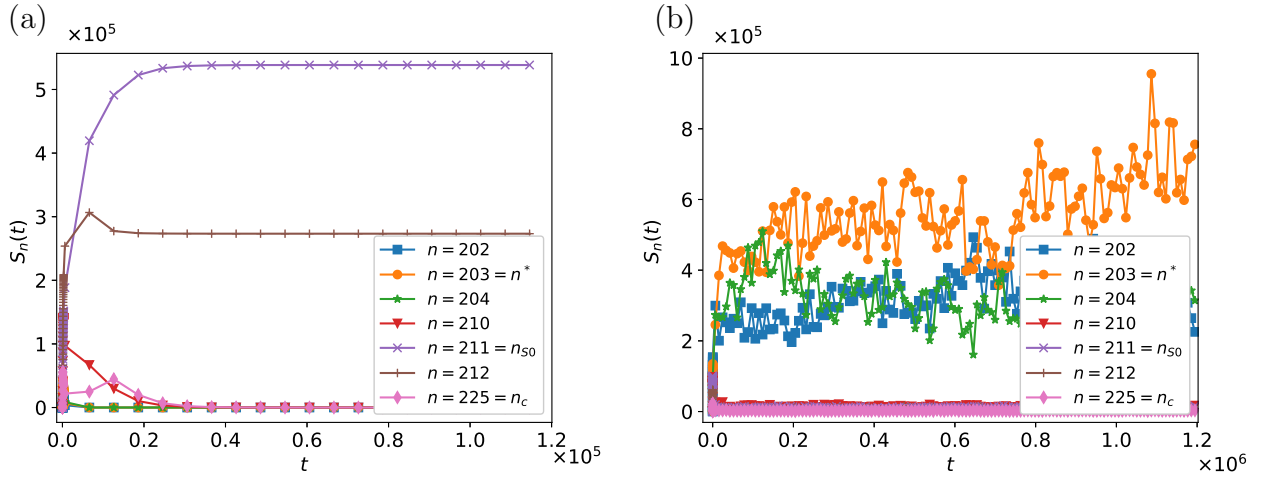

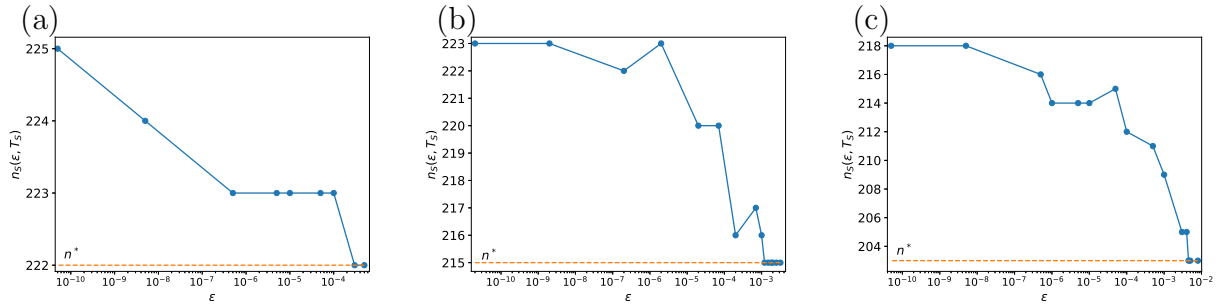Figure A.3: S_n as a function of time for $\alpha = 0.17$. (a) $\varepsilon = 0.0$. (b) $\varepsilon = 0.005$.

Figure A.4: $n_S(\varepsilon, T_S)$ for (a) $\alpha = 0.24$. (b) $\alpha = 0.22$. (c) $\alpha = 0.17$.
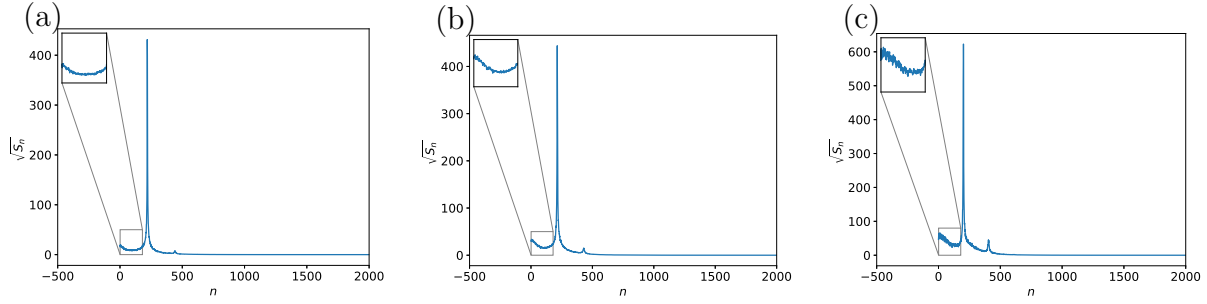
97

Figure A.5: $\sqrt{S_n}$ as a function of n for (a) $\alpha = 0.24$, $\varepsilon = 0.0005$. (b) $\alpha = 0.22$, $\varepsilon = 0.0025$. (c) $\alpha = 0.17$, $\varepsilon = 0.005$. Inset: Excitation of small wave number modes.
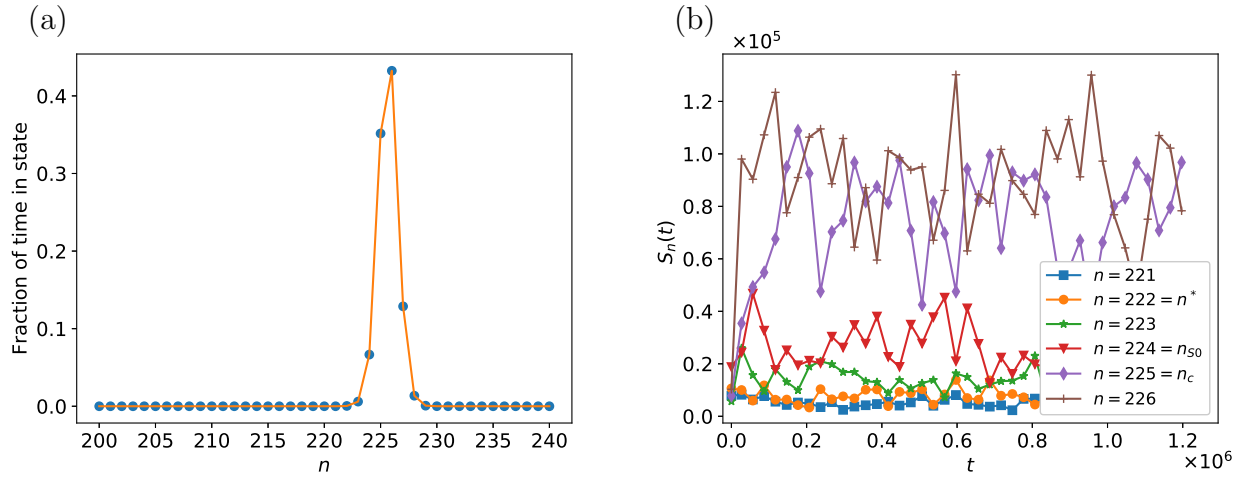

Figure A.6: (a) Long-time probability distribution of final states for $\alpha = 0.24$, $\varepsilon = 0.0005$ with the first 50 modes suppressed. (b) S_n as a function of time.

Figure A.7: (a) Long-time probability distribution of final states for $\alpha = 0.22$, $\varepsilon = 0.0025$ with the first 50 modes suppressed. (b) S_n as a function of time.
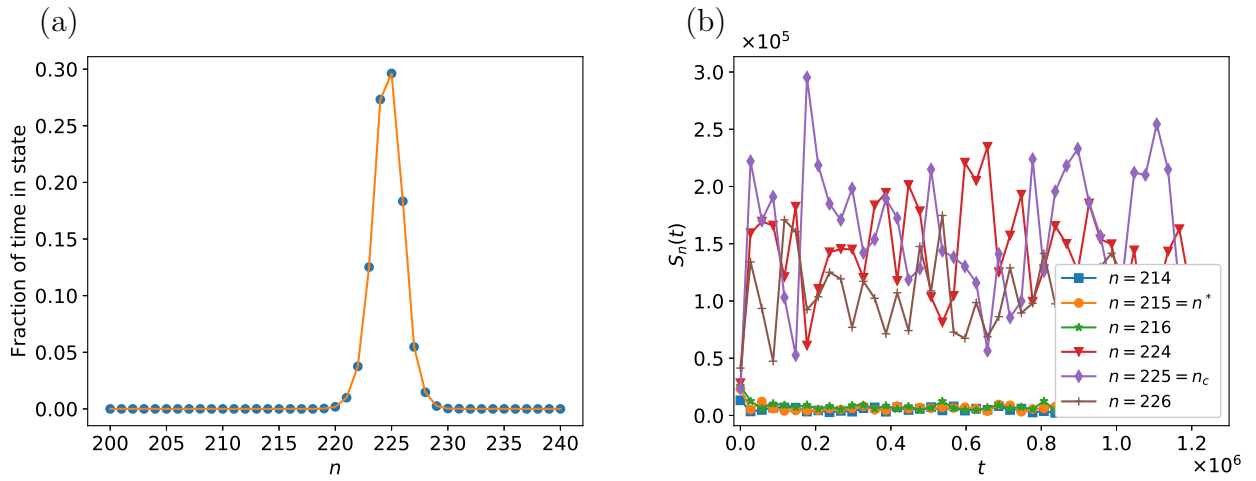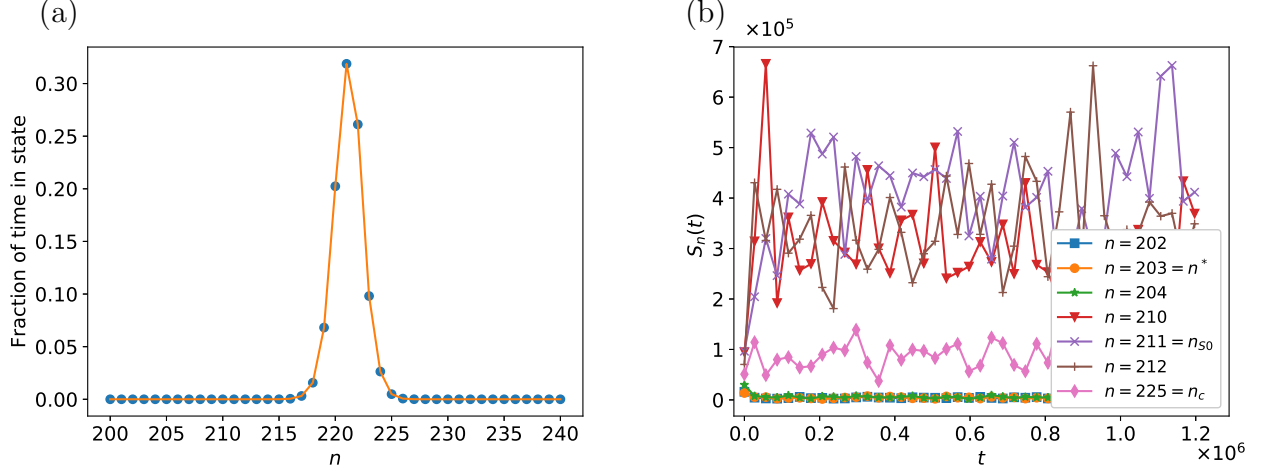
Figure A.8: (a) Long-time probability distribution of final states for $\alpha = 0.17$, $\varepsilon = 0.005$ with the first 50 modes suppressed. (b) S_n as a function of time.

S_{50}, as seen in Fig. A.9.

Finally, we give a heuristic explanation for why S_n decreases as n approaches n_E^- from the left. According to the discussion above, initially, the most important nonlinear terms in the equation for $\dot{S}_{25}$ are the ones involving $\widetilde{u}_{\pm n_c}$. These terms are proportional to $Re\langle \widetilde{u}_{25}\widetilde{u}_{n_c}\widetilde{u}_{-250}\rangle$ and $Re\langle \widetilde{u}_{-25}\widetilde{u}_{-200}\widetilde{u}_{n_c}\rangle$. In contrast, the corresponding terms in the equation for $\dot{S}_1$ are proportional to $Re\langle \widetilde{u}_1\widetilde{u}_{224}\widetilde{u}_{-n_c}\rangle$ and $Re\langle \widetilde{u}_{-1}\widetilde{u}_{226}\widetilde{u}_{n_c}\rangle$. On average, $|\widetilde{u}_{224}|$ and $|\widetilde{u}_{226}|$ are likely to be larger than $|\widetilde{u}_{200}|$ and $|\widetilde{u}_{250}|$ (at the end of the linear regime). This means that the nonlinear terms in $\dot{S}_1$ for a fixed n_1 are generally larger than the corresponding terms in $\dot{S}_{25}$ and $\dot{S}_{50}$. The overall result is that $\dot{S}_{25}$ and $\dot{S}_{50}$ are always smaller than $\dot{S}_1$. In general, we observe that $|\dot{S}_n|$ decreases as n approaches the Eckhaus band from the left. For this reason, S_n in Fig. 6.7 decreases with n for $n < n_E^-$.
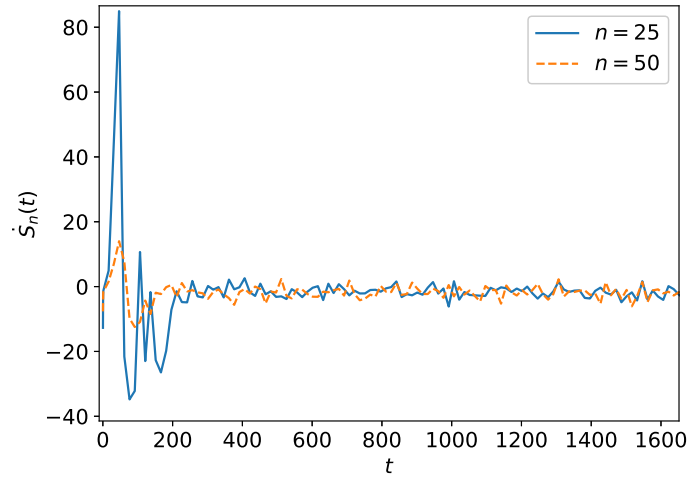
Figure A.9: dS_n/dt with $n = 25$ and $n = 50$ for $\alpha = 0.20$ and $\varepsilon = 0.0001$.

Bibliography

[1] K. M. S. Bajaj, N. Mukolobwiez, N. Currier, and G. Ahlers. Wavenumber selection and large-scale flow effects due to a radial ramp of the spacing in Rayleigh-Bénard convection. *Phys. Rev. Lett.*, 83:5282, 1999.

[2] C. Misbah and A. Valance. Secondary instabilities in the stabilized Kuramoto-Sivashinsky equation. *Phys. Rev. E*, 49:166, 1994.

[3] D. S. Cannell, M. A. Dominguez-Lerma, and G. Ahlers. Experiments on wave number selection in rotating Couette-Taylor flow. *Phys. Rev. Lett.*, 50:1365, 1983.

[4] L. Kramer, E. Ben-Jacob, H. Brand, and M. C. Cross. Wavelength selection in systems far from equilibrium. *Phys. Rev. Lett.*, 49:1891, 1982.

[5] D. Obeid, J. M. Kosterlitz, and B. Sandstede. State selection in the noisy stabilized Kuramoto-Sivashinsky equation. *Phys. Rev. E*, 81:066205, 2010.

[6] L. Qiao, Z. Zheng, and M. C. Cross. Minimum-action paths for wavenumber selection in non-equilibrium systems. *Phys. Rev. E*, 93:042204, 2016.

[7] S. Saxena and J. M. Kosterlitz. Wavenumber selection in pattern-forming systems. *Phys. Rev. E*, 100:022223, 2019.

[8] C. W. Gardiner. *Handbook of Stochastic Methods for Physics, Chemistry and the Natural Sciences*. Springer-Verlag, Berlin Heidelberg, 1985.

[9] M. C. Cross and P. C. Hohenberg. Pattern formation outside of equilibrium. *Rev. Mod. Phys.*, 65:851, 1993.

[10] M. C. Cross and H. Greenside. *Pattern Formation and Dynamics in Nonequilibrium Systems*. Cambridge University Press, New York, 2009.

[11] V. Eckhaus. *Studies in Nonlinear Stability Theory*. Springer-Verlag, Berlin, 1965.

[12] J. S. Langer. Instabilities and pattern formation in crystal growth. *Rev. Mod. Phys.*, 52:1, 1980.

[13] K. A. Jackson and J. D. Hunt. *Trans. Metall. Soc. AIME*, 236:1129, 1966.

[14] J. M. Flesselles, A. J. Simon, and A. J. Libchaber. Dynamics of one-dimensional interfaces: An experimentalist's view. *Adv. Phys.*, 40:1, 1991.

[15] A. J. Simon, J. Bechhoefer, and A. J. Libchaber. Solitary modes and the Eckhaus instability in directional solidification. *Phys. Rev. Lett.*, 61:2574, 1988.

[16] P. C. Hohenberg, L. Kramer, and H. Riecke. Effects of boundaries on one dimensional reaction-diffusion equations near threshold. *Physica*, 15D:402, 1985.

[17] Jordi Garcia-Ojalvo and Jose M. Sancho. *Noise in Spatially Extended Systems*. Springer-Verlag, New York, 1999.

[18] M. Kerszberg. Pattern emergence and selection in crystal growth. *Phys. Rev. B*, 27:3909, 1983.

[19] M. Kerszberg. Pattern selection in directional solidification. *Phys. Rev. B*, 28:247, 1983.

[20] H. Risken. *The Fokker-Planck Equation: Methods of Solution and Applications*. Springer-Verlag, Berlin Heidelberg, 1989.

[21] J. Swift and P. C. Hohenberg. Hydrodynamic fluctuations at the convective instability. *Phys. Rev. A*, 15:319, 1977.

[22] J. Viñals, E. Hernández-García, M. San Miguel, and R. Toral. Numerical study of the dynamical aspects of pattern selection in the stochastic Swift-Hohenberg equation in one dimension. *Phys. Rev. A*, 44:1123, 1991.

[23] Lord Rayleigh. On the dynamics of revolving fluids. *Proc. R. Soc. London Ser. A*, 93:148, 1916.

[24] H. Bénard. Les tourbillons cellulaires dans une nappe liquide transportent de la chaleur par convection en regime permanent. *Ann. Chim. Phys.*, 7:62, 1900.

[25] G. I. Taylor. Stability of a viscous liquid contained between two rotating cylinders. *Phil. Trans. R. Soc. A*, 223:289, 1923.

[26] C. D. Andereck, S. S. Liu, and H. L. Swinney. Flow regimes in a circular Couette system with independently rotating cylinders. *J. Fluid Mech.*, 164:155, 1986.

[27] E. Ben-Jacob, H. Shmueli, O. Shochet, and A. Tenenbaum. Self-organization during growth of bacterial colonies. *Physica A*, 187:378, 1992.

[28] B. N. Belintsev. Collective phenomena in the multicellular development of dictyostelium discoideum. In V. I. Krinsky, editor, *Self-organization, Autowaves and Structures Far from Equilibrium*. Springer-Verlag, Berlin, 1984.

[29] L. V. Belousov. Synergetics and biological morphogenesis. In V. I. Krinsky, editor, *Self-organization, Autowaves and Structures Far from Equilibrium*. Springer-Verlag, Berlin, 1984.

[30] Bruno Grossmann, K. R. Elder, Martin Grant, and J. M. Kosterlitz. Directional solidification in two and three dimensions. *Phys. Rev. Lett.*, 71:3323, 1993.

[31] A. Buka and L. Kramer. *Pattern Formation in Liquid Crystals*. Springer-Verlag, Berlin, 1996.

[32] M. C. Cross. Derivation of the amplitude equation at the Rayleigh-Bénard instability. *Phys. Fluids*, 23:172, 1980.

[33] A. C. Newell. Envelope equations. In *Lectures in Applied Mathematics*, volume 15, page 157. American Mathematical Society, Providence, RI, 1974.

[34] G. Ahlers, M. C. Cross, P. C. Hohenberg, and S. Safran. The amplitude equation near the convective threshold: Application to time-dependent heating experiments. *J. Fluid Mech.*, 110:297, 1981.

[35] M. C. Cross and A. C. Newell. Convection patterns in large aspect ratio systems. *Physica D*, 10:299, 1984.

[36] J. E. Wesfreid and V. Croquette. Forced phase diffusion in Rayleigh-Bénard convection. *Phys. Rev. Lett.*, 45:634, 1980.

[37] Y. Kuramoto and T. Tsuzuki. Persistent propagation of concentration waves in dissipative media far from thermal equilibrium. *Prog.Theor. Phys.*, 55:356, 1976.

[38] G. I. Sivashinsky. Nonlinear analysis of hydrodynamic instability in laminar flames. part i. derivation of basic equations. *Acta Astraunautica*, 4:1177, 1977.

[39] D. J. Benney. Long waves on liquid films. *J. Math. Phys.*, 45:150, 1966.

[40] H. Chaté and P. Manneville. Transition to turbulence via spatio-temporal intermittency. *Phys. Rev. Lett.*, 58:112, 1987.

[41] P. Manneville. Statistical properties of chaotic solutions of a one-dimensional model for phase turbulence. *Phys. Lett. A*, 84:129, 1981.

[42] P. Manneville. Liapounov exponents for the kuramoto-sivashinsky model. In O. Pironneau, editor, *Macroscopic Modeling of Turbulent Flows*. Springer-Verlag, Berlin, 1985.

[43] J. M. Hyman, B. Nicolaenko, and S. Zaleski. Order and complexity in the Kuramoto-Sivashinsky model of weakly turbulent surfaces. *Physica D*, 23:265, 1986.

[44] Y. Pomeau, A. Pumir, and P. Pelcé. Intrinsic stochasticity with many degrees of freedom. *J. Stat. Phys.*, 37:39, 1984.

[45] A. Pumir. Statistical properties of an equation describing fluid interfaces. *J. Phys. (Paris)*, 46:511, 1985.

[46] S. Tajima and H. Greenside. Microextensive chaos of a spatially extended system. *Phys. Rev. E*, 66:017205, 2002.

[47] I. Bena, C. Misbah, and A. Valance. Nonlinear evolution of a terrace edge during step flow growth. *Phys. Rev. B*, 47:7408, 1993.

[48] C. Misbah, H. M'uller-Krumbhaar, and D. E. Temkin. Interface structure at large supercooling. *J. Phys. I (France)*, 1:585, 1991.

[49] A. Novick-Cohen. Interfacial instabilities in directional solidification of dilute binary alloys: The Kuramoto-Sivashinsky equation. *Physica D*, 26:403, 1987.

[50] G. Ahlers, D. S. Cannell, M. A. Dominguez-Lerma, and R. Heinrichs. Wavenumber selection and Eckhaus instability in Couette-Taylor flow. *Physica D*, 23:20, 1986.

[51] W. Arter, A. Bernoff, and A. C. Newell. Wavenumber selection of convection rolls in a box. *Phys. Fluids*, 30:3840, 1987.

[52] J. C. Buell and I. Catton. Wavenumber selection in ramped Rayleigh-Bénard convection. *J. Fluid Mech.*, 171:477, 1986.

[53] R. N. C. Filho, J. M. Kosterlitz, and E. Granato. Pattern selection in a phase field model for directional solidification. *Physica A*, 354:333, 2005.

[54] H. S. Greenside and M. C. Cross. Stability analysis of two-dimensional models of three-dimensional convection. *Phys. Rev. A*, 31:2492, 1985.

[55] E. Hernández-García, M. san Miguel, R. Toral, and J. Viñals. Noise and pattern selection in the one dimensional Swift-Hohenberg equation. *Physica D*, 61:159, 1992.

[56] D. A. Kurtze. Noise and dynamical pattern selection. *Phys. Rev. Lett.*, 77:63, 1996.

[57] H. R. Schober, E. Allroth, K. Schroeder, and H. Müller-Krumbhaar. Dynamics of periodic pattern formation. *Phys. Rev. A*, 33:567, 1986.

[58] E. Bodenschatz and L. Kramer. Influence of lateral boundaries on the Eckhaus instability in anisotropic pattern-forming systems. *Physica D*, 27:249, 1987.

[59] Y. Pomeau and P. Manneville. Stability and fluctuations of a spatially periodic convective flow. *J. Phys. (Paris)*, 40:609, 1979.

[60] E. Hernández-García, J. Viñals, R. Toral, and M. san Miguel. Fluctuations and pattern selection near an Eckhaus instability. *Phys. Rev. Lett.*, 70:3576, 1993.

[61] M. I. Freidlin and A. D. Wentzell. *Random Perturbations of Dynamical Systems*. Springer, New York, 2012.

[62] L. Q. Chen and J. Shen. Applications of semi-implicit fourier spectral method to phase field equations. *Comput. Phys. Commun.*, 108:147, 1998.

[63] Lloyd N. Trefethen. *Spectral Methods in MATLAB*. SIAM, Philadelphia, 2000.

[64] S. Saxena and J. M. Kosterlitz. Dynamics of noise-induced wave-number selection in the stabilized Kuramoto-Sivashinsky equation. *Phys. Rev. E*, 103:012205, 2021.

[65] L. S. Tsimring. Noise in biology. *Rep. Prog. Phys.*, 77:026601, 2014.

[66] Jie Shen, Tao Tang, and Li-Lian Wang. *Spectral Methods: Algorithms, Analysis and Applications*. Springer-Verlag, Berlin Heidelberg, 2011.